Finite element modelling of hybrid (spot welded/bonded) joints under service conditions

Weidong Dang

Par **Weidong DANG**

Finite element modelling of hybrid (spot welded/bonded) joints under service conditions

Thèse présentée pour l'obtention du grade de Docteur de l'UTC

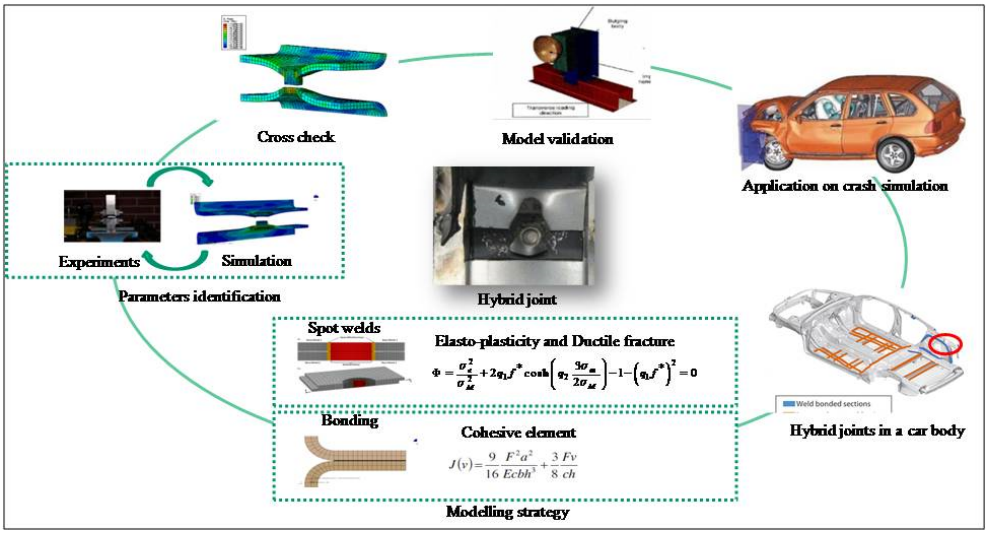

Soutenue le 20 février 2015
Spécialité : Mécanique Avancée

D2187

utc
Université de Technologie
Compiègne

Par Weidong DANG

Finite Element Modelling of hybrid (spot welded/bonded) joints under service conditions

Thèse présentée
Pour l'obtention du grade
De Docteur de l'UTC

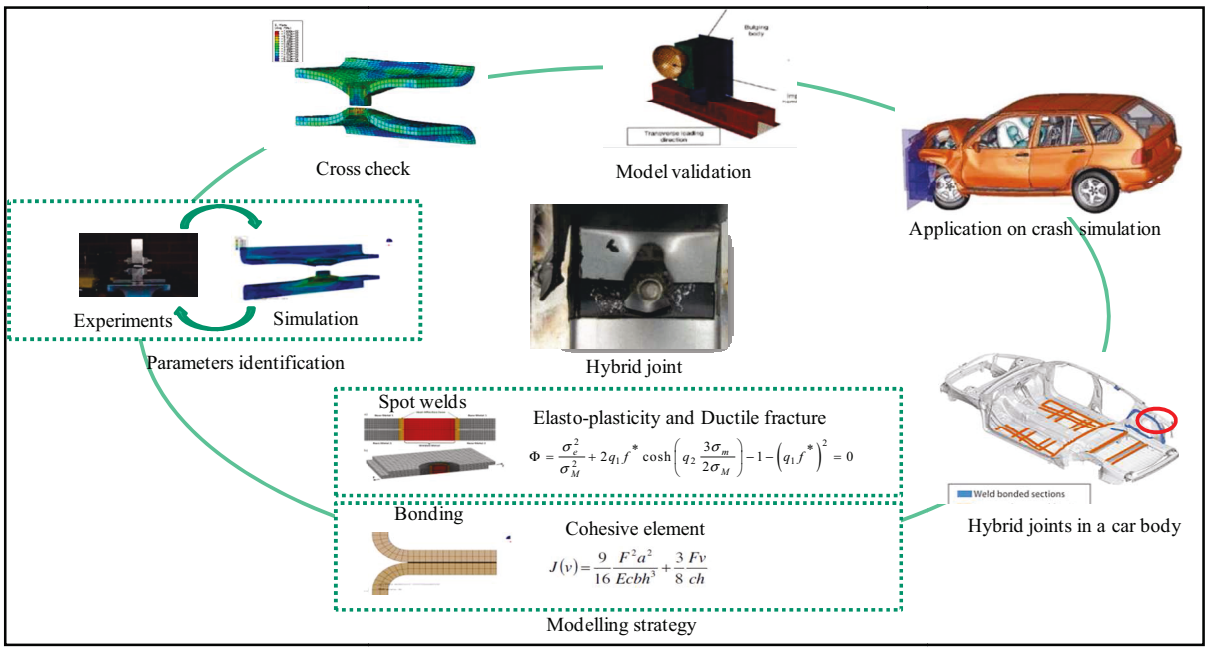

Soutenance prévue le 20 février 2015 à l'UTC

Jury:
Prof. Farid Abed-Meraim, ENSAM (Rapporteur)
Prof. Pierre-Olivier Bouchard, MINES ParisTech (Examinateur)
Prof. Daniel Marceau, Université du Québec à Chicoutimi (Rapporteur)
Prof. Said Hariri, Ecole des Mines de Douai (Examinateur)
Eng. Roland Jaeggi, Sika Technology AG (Examinateur)
Prof. Gerard Moulin, UTC (Examinateur)
Dr. Mohamed Rachik, UTC (Directeur de thèse)

Abstract:

Spot welding and adhesive bonding are widely used in joining of sheet metals, such as assembling of car body-in-white. Recently, spot weld and adhesive are combined to make weld bonded joint, which is employed to join Advanced High Strength Steel to improve the stiffness and crashworthiness of car body. In industry, the assessment of designing prior to prototype requires reliable constitutive models in terms of the prediction of the mechanical behaviors. The FE model of weld bonded joint is a new challenge as it should combine the models of spot welding and the models of adhesive.

This thesis focuses on the modeling of weld bonded joint by DP600 steel and structural adhesive SikaPower®-498. The model of weld bonded joint consists of solid model and simplified model. The former is devoted to predict the behavior of weld bonded joint on small-scale specimen: KS2 and lap-shear. The latter can be used to predict the performance of large components with acceptable computational cost.

As regards solid model, spot welded joint and adhesive bonded joint behaviors are separately identified by KS2 specimen under different loading path. The inhomogeneities in fusion zone and heat affected zone of spot weld are taken into account via the scaling of the flow stress of base metal. The scaling factors are calibrated by inverse identification. Gurson model is used to predict ductile fracture in heat affected zone and base metal while cohesive zone model is employed to simulate quasi-brittle fracture in the interface of fusion zone. The parameters of cohesive zone model are identified by the J-integral at the notch tip of spot weld crack. Cohesive zone elements with traction-separation-laws are also used to predict adhesive debonding. Model parameters are calibrated by Double Cantilevered Beam and End Notched Flexure specimens, corresponding to Mode-I and Mode-II fracture respectively. The model developed for spot weld is associated with adhesive model to predict weld bonded joint.

As regards simplified model, connector elements are employed to predict the damage of spot weld. The parameters of connector element are identified by KS2 tests under different loading paths. Finally, the simplified model of spot welding, adhesive bonding, and weld-bonding are validated by T-joint which can represent the B-pillar of car body.

Key words: Spot welding, Adhesive bonding, Hybrid joining, Finite element, Constitutive modelling, Inverse identification, Cohesive zone.

Résumé:

Le soudage par point et le collage sont largement utilisés dans la jonction des tôles, telles que l'assemblage de caisses de voiture. Récemment, le soudage par point et le collage ont été combinés pour faire le joint hybrid soudé-collé, qui est utilisé pour joindre les aciers à hautes résistances et améliorer la rigidité et la résistance aux chocs des corps de voiture. Dans l'industrie, l'évaluation de la conception avant prototype nécessite des modèles fiables de comportement en termes de prédiction des comportements mécaniques. Le modèle élément finis de joint soudé-collé est un nouveau défi car il doit combiner les modèles de soudage par points et les modèles de collage.

Cette thèse se concentre sur la modélisation du joint soudé-collé par de l'acier DP600 et avec l'adhésif structurel SikaPower®-498. La modélisation peur utiliser un modèle solide ou un modèle simplifié (élément coque plus élément de connexion). Le modèle solide permet de prédire le comportement de spécimen à petite échelle: KS2 et cisaillement. Le modèle simplifié peut être utilisé pour prédire la performance des composants de grande dimension avec un coût de calcul acceptable.

En ce qui concerne le modèle solide, le comportement du joint soudé et du joint collé sont identifiés séparément calibrés sur un spécimen KS2 sous trajets de chargement différents. Les inhomogénéités dans la zone de fusion et la zone affectée par la chaleur du soudage par point sont prises en compte par l'intermédiaire de facteurs d'échelle applique à la contrainte d'écoulement du métal de base. Les facteurs d'échelle sont determinés par identification inverse. Le modèle de Gurson est utilisé pour prédire la rupture ductile en zone affectée par le chaleur et dans le métal base tandis que le modèle de zone cohésive est utilisé pour simuler la rupture quasi-fragile dans l'interface de la zone de fusion. Les paramètres du modèle de zone cohésive sont identifiés par l'intégrale J à la pointe de fissure de la soudure. Des éléments de zone cohésive avec une loi traction-séparation sont également utilisés pour prédire le décollement adhésif. Les paramètres du modèle sont identifiés par des essais du type « Double Cantilevered Beam » et « End Notched Flexure », correspondant aux mode I et mode II respectivement. Le modèle élaboré pour le soudage par est associé avec le modèle de collage pour prédire le comportement et la rupture du joint soudé-collé.

En ce qui concerne le modèle simplifié, des éléments de connexion sont utilisés pour prédire les endommagement des soudure par point. Les paramètres de l'élément de connexion sont identifiés

par des tests de KS2 sous différents trajets de chargement. Enfin, les modèles simplifiés d'un soudage, d'un collage, et d'un soudé-collé sont validés sur une jonction en T qui peut représenter le pilier-B de carrosserie de la voiture.

Mots clés: Soudage par point, Collage, Assemblage hybride, Eléments finis, Lois de comportement, Identification inverse, Zones cohésives.

Acknowledgements

I would like to thank my advisor Mohamed Rachik, for his encouragement, instruction, and understanding. His broad level of knowledge, expertise, and interests are unmatched. He always steers me on the right way. During the report revision, he took his patience to fix the text problems raised by me.

I would like to give my appreciation to the Chinese Scholarship Committee for the finance supports. Thanks Dr. Pierre Jousset, previously in Sika AG, for sponsoring this research and the contributions for adhesive modelling. I would like to thank Dr. Hein at Laboratorium für Werkstoff und Fügetechnik of the University of Paderborn for the tests and valuable information.

I would like to thank my collegues in the laboratories, Velluet Isabelle for the preparation of metallographic, Wtyklo Jean-Patrick for SEM analysis. I also thank to my colleagues and friends Kang YANG, Raoelison Rija, Xiongjie LIU for the encouragement and discussion.

I would also like to thank the members of my reading committee: Prof. Farid ABED-MERAIM from ENSAM, Prof. Pierre-Olivier BOUCHARD, Prof. Daniel MARCEAU, Prof. Said HARIRI, Eng. Roland JAEGGI, Prof. Gerard MOULIN, for your reading, correction and discussion during the defense.

At the end, I want to give my love to my parents for their support and comprehension, both of which were essential. My daughters Camille were invaluable for her laugh which relaxed me when I was tired from the work. I am especially thankful for my wife. They are most important to me and make everyday a wonderful experience.

Symbols	Explanation
A	Gaussian distribution function
A_1	Eutectoid temperature
A_3	The lower-temperature boundary
Ac_1	The temperature at which austenite begins to form during heating
Ac_3	The temperature at which transformation of ferrite to austenite is completed during heating
A_{cm}	The counterpart boundary for high-carbon contents
a_1, a_2, a_3, a_4	Parameter of damage potential function
b_1, b_2, b_3, b_4	Parameter of potential function of displacement
$\boldsymbol{C}$	Fourth-order constitutive tensor
$c_i(x)$	Computed response for inverse identification
D_{ii}	Connector stiffness
d	Evolution of the damage variable
E	Young's module
F	Force
F_c	Evaluated force
F_{eff}	Effective force without damage
F_n	Critical force along normal direction
F_s	Derived force along shear direction
F^0	Yielding force
F_i	i^{th} component of force or moment
f	Void volume fraction in Gurson model
$\mathbf{f}$	Collection of forces and moments
f_N	Volume fraction of nucleating void
f_F	Yielding function
f_0	Initial void volume fraction
f_1	Force along first direction
f_2	Force along second direction

f_3	Force along third direction
f_c	Critical value of voids coalescence
f_f	Void volume fraction at fracture
f_n	Derived force along normal direction
f_s	Derived force along shear direction
f^*	Modified void volume fraction by Tvergaard
$f(x)$	Least square function
$\boldsymbol{I}$	First order identity tensor
I_{min}	Minimum welding current
I_{max}	Maximum welding current
G	Shear modulus
G_n	Energy along normal direction of model I
G_s	Energy along the first direction of model II
G_t	Energy along the second direction of model III
G^C	Mixed model fracture energy
G_{Ic}	Critical fracture energy of model I
G_{IIc}	Critical fracture energy of model II
K	Strength coefficient of Swift's equation
K_n	Stiffness of model I
K_s	Stiffness along first direction of model II
K_t	Stiffness along second directions of model III
L_c	Characteristic length of element
M_b	Critical bending moment at failure
M_t	Critical torsion moment at failure
m_1	Moment along first axis
m_2	Moment along second axis
m_3	Moment along third axis
$m_i(x)$	Measured response for inverse identification
n	Hardening exponent
P	Hydrostatic stress
$P(f)$	Magnitude of connector traction

q_1,q_2,q_3	Materials constant of Gurson model
r_{inf}	Influence radius of fastener
S_N	Standard deviation for the normal distribution
t	Steel thickness
$\boldsymbol{t}$	Nominal traction stress vector
T_0	Original adhesive thickness
t_n	Normal stress of model I
t_s	Shear stress along first direction of model II
t_t	Shear stress along second direction of model III
U	Relative motion
U_b	Relative motion in bending
U_n	Relative motion in normal
U_s	Relative motion in shear
U_t	Relative motion in torsion
$\bar{U}$	Coupled motion
$\bar{u}^{pl}$	Equivalent plastic relative motion
$\bar{u}_0^{pl}$	Equivalent plastic motion at plasticity initiation
$\bar{u}_f^{pl}$	Equivalent plastic motion at ultimate failure
$\dot{u}^{pl}$	Rate of plastic relative motion
$\dot{\bar{u}}^{pl}$	Rate of equivalent plastic relative motion.
u_i	Connector displacement or rotation in the i^{th} direction
α	Damage evolution exponent
α_1	Scaling factor of heat affected zone
α_2	Scaling factor of welded metal zone
ε_0	Prior plastic strain
ε_N	Mean voids nucleation burst strain
ε_n	Normal separation of model I
ε_s	Shear separation along first direction of model II
ε_t	Shear separation along second direction of model III
ε^e	Elastic strain

ε^p	Plastic strain
$\bar{\varepsilon}^p$	Equivalent plastic strain
$\bar{\dot{\varepsilon}}_m^p$, $\dot{\varepsilon}_m^p$	Matrix equivalent plastic strain and plastic strain rate
Φ	Yielding function
ξ	Benzeggagh-Kenane mix model parameter
ρ	Materials density
σ	Cauchy stress tensor
σ_0	Normal stress at damage initiation of model I
σ_e	Equivalent von Mises stress
σ_y	Yielding stress
$\boldsymbol{\sigma}'$	Deviatoric stress tensor
σ_{HAZ}	Stresses of heat affected zone
σ_{WM}	Stresses of welded metal
δ_n	Normal separations displacements of model I
δ_s	Shear separations displacements of model II
δ_t	Shear separations displacements of model III
τ_0	Shear stress at damage initiation of model II
:	Double-dot product
<>	Macauley bracket

Abbreviation

Abbreviation	*Explanation*
AB	Adhesive bonding/adhesive bonded
AFM	Atomic force microscopy
AHSS	Advanced high strength steel
B-K	Benzeggagh-Kenane
BM	Base metal
CP	Complex phase
CZM	Cohesive zone model
DCB	Double cantilever beam
DIC	Digital image correlation
DP	Dual phase
ENF	End notched flexure
FE	Finite element
HAZ	Heat affected zone
IF	Interfacial fracture
ISO	International standard organization
KS2	Combined tension-shear specimen
Ms	Martensite start
MS	Martensite steel
M-S	Mahnken-Schilimmer
OM	Optical microscopy
PO	Pull-out
SEM	Scanning electron microscopy
SW	Spot welding/Spot welded
TRIP	Transformation induced plasticity
TSLs	Traction-separation laws
TWIP	Twist induced plasticity
WB	Weld bonding/weld bonded
WM	Welded metal

Table of content

Chapter 1. Introduction

In the world, there were about *1 billion* cars and light trucks on the road in *2013* and the growing is still by roughly *40 million* yearly. Based on current predictions, the number of cars in emerging and developing economies could increase by *1.9 billion* from *2005* to *2050*, bringing the world's total to nearly *3 billion* automobiles [1]. The exhaustion of non-renewable fossil energy and the environment pollution force us to continuously improve the vehicle in terms of fuel consumption efficiency and gas emission and also to develop electrical vehicles or hybrid cars. To meet these purposes, the main way is to reduce car weight. Most of modern cars opt for uni-body construction and advanced materials to gain light-weight, passenger safety and performance. This design needs a large number of steel sheet to form different substructures, which are finally assembled together to produce whole car body [2]. In addition, some lightweight structure materials are chosen to reduce car weight, such as aluminum, magnesium and composite materials. For these developments, the materials, their processing and joining processes play prominent role in the quality of car body.

Over the last decade, Advanced High Strength Steel (AHSS) were widely introduced in automotive industry due to the improvement in formability and crash worthiness compared to conventional steel grades. AHSS include dual phase (DP) steel, transformation induced plasticity (TRIP) steel, twinning induced plasticity (TWIP) steel, complex phase (CP) steel and martensitic steels (MART) steel [3]. Figure 1-1 shows the elongation versus tensile strength at fracture of several steels used in automobile industry. The strength of AHSS is increased in large amount meanwhile the formability remains acceptable. AHSS help reducing car weight by using high strength thinner sheet metal gauge gaining the same stiffness and strength that are obtained with thick conventional steels.

For the manufacturing of a typical family car, the possible joining technology could include welding (electrical resistance welding, arc welding, laser welding and soldering) and mechanical fastener (riveting, screw, bolts, clinching, hemming). However, welding is always difficult when dealing with dissimilar metals. Dissimilar metals joined by fastener are likely to cause galvanic corrosion. In addition, welding is not possible for non-metallic materials, e.g. plastic and composite. Hence, adhesive bonding is the optimal joining method for dissimilar materials in car body assembly.

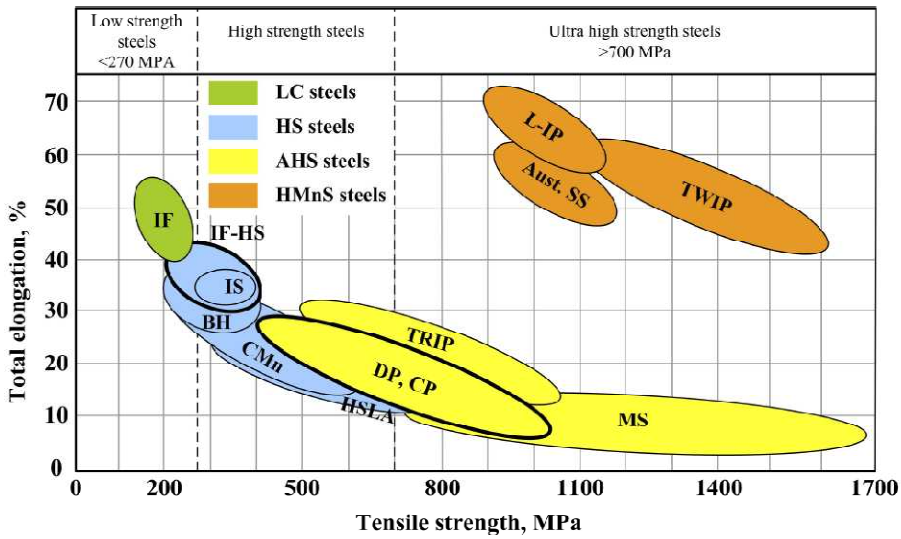

Figure 1-1. *Elongation versus tensile strength at fracture of different types of steels* [4].

Adhesive bonding has notable advantages like uniform stress distribution, fatigue life improvement and low cost [5]. When using adhesive for joining large structure in assembly line, it could be difficult to accurately position and maintain the parts in position. To overcome such difficulties, hybrid joints are developed by combining mechanical fasteners with adhesive bonding, such as spot welded bonded, bolted welded and laser welded bonded joints. Figure 1-2 (a) shows a complex car body structure, in which several types of aluminum alloys are combined with high strength steels to reduce the car weight. To join these dissimilar materials, different joining technologies are used as illustrated in Figure 1-2 (b).

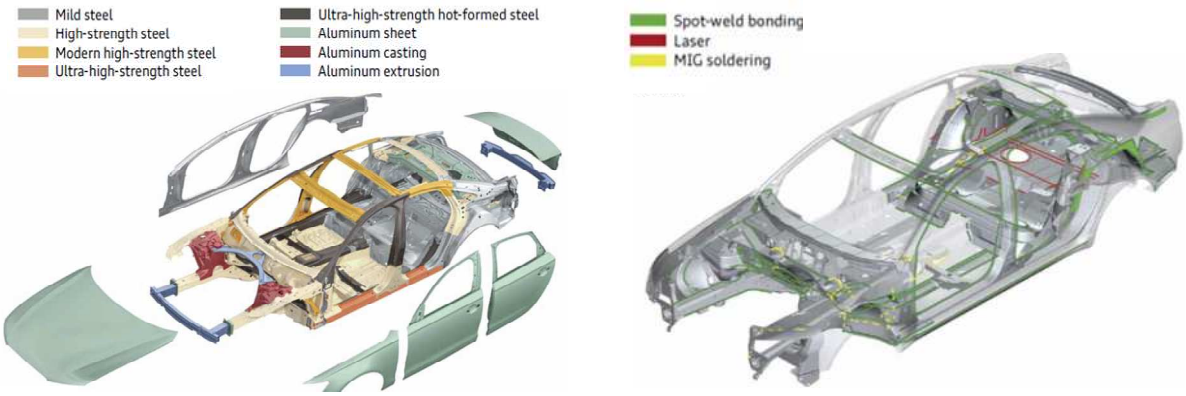

(a) **(b)**

Figure 1-2. *A typical car contains (a) multi-materials and (b) diversified joining techniques. (Source Audi)*

To design the above complex car frame, computer simulation is widely used by automakers in computer-aided engineering (CAE) analysis for crashworthiness in order to reduce the manufacturing cost and the development cycle by reducing the number of real crash tests. The crash test simulation, as illustrated in Figure 1-3, is used for design optimization on virtual prototype before a real prototype is manufactured. This simulation can predict the acceleration, the intrusions into the cabin and the risk of injury to the vehicle occupant.

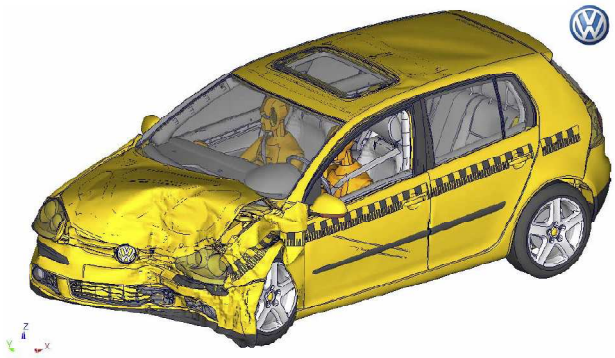

Figure 1-3. *Crash simulation of whole car (Sourse: Volkswagen)*

The car crash simulation is always facing problems of constitutive modeling when new materials and specific joining processes are used. As a consequence, material suppliers are requested to supply material input data and support for constitutive modeling of their materials. In this context, several research projects were initiated by Sika for the development of adequate models to predict failure behavior of new adhesive and hybrid joint. Recently, adhesive constitutive models were investigated by Jousset in [6]. The aim of our work is to extend the previous investigations to welded bonded joints. The microstructure of spot weld was firstly analyzed in order to investigate the spot weld structure and the interaction between the spot weld and the adhesive in hybrid joints. Material properties of welded metal and heat affected zone are calibrated based on the scaling of the base metal.

The modeling of spot weld behavior is carried out on two different scales with a solid finite element model and a simplified shell connector model. In the solid model, Gurson model is used to predict ductile fracture (pull-out fracture) of spot weld, while cohesive zone model is adopted for the simulation of interfacial fracture in the interface as Gurson model cannot predict voids coalescence under nearly zero stress triaxility. The parameters of cohesive zone model are calibrated using J-integral at notch tip of spot weld nugget. In the simplified model, connector

element associated with mesh independent fastener permit to simulate large component by saving computational time. Cohesive zone elements are also used to predict the adhesive failure. The material parameters are calibrated by DCB and ENF specimens, corresponding to Mode-I and Mode-II fracture. These two models are combined together to simulate hybrid joint.

Finally, the model was validated against T-joint benchmark that is representative of B-pillar of car frame. The predictions from the models are in good accordance with the test results. The model developed is intended to be used together with large industrial applications such as full car bodies crash-test simulations.

This document is organized in 6 chapters. In Chapter 1, the backgrounds and the motivations of this work are presented. Chapter 2 is the chapter for bibliographies, in which dual phase steel, spot welds, adhesive and weld bonding are introduced. Chapter 3 is devoted to introduce the specimens of KS2, peel and lap-shear. The force-displacement measurements and the results are discussed for each test. Chapter 4 introduces the numerical modeling, the material parameter calibration and the finite element analysis of simple tests. The obtained results are discussed. In Chapter 5, the simplified model is validated by different T-joint under longitudinal and transverse loading cases. Chapter 6 summarizes the main conclusions of this thesis and also present future work to be continued following this work.

Chapter 2. Bibliography

1. Dual phase steel

Advanced high strength steels (AHSS) are widely used in automobile industry for safety and light weight body design [7]. Dual phase (DP) steels are referred to as advanced high strength steel (AHSS). The microstructure of DP steels is composed of soft ferrite matrix and hard martensite with small amounts of bainite, pearlite, or retained austenite. This type of microstructure allows DP steels achieving high strength, continuous yield behavior, high work-hardening rate and superior ductility. Moreover, DP steel shows strong bake hardening effect which is highly advantageous for car body bake process [8-11]. DP steel properties are significantly influenced not only by grain size but also by martensite phase volume fraction, distribution, morphology and carbon content [8] [12-13].

Table 1-1. *Chemical composition of DP600 steel*

Elements	***C***	***Si***	***Mn***	***Cr***	***Al***	***S***	***P***
Content in *Weight %*	*0.08*	*0.5*	*1.4*	*0.42*	*0.42*	*0.008*	*0.085*

Table 1-1 shows typical chemical composition of DP600 steel. Adequate carbon weight fraction *(<0.1%*) can provide adequate martensite fraction (about *20%*) without diminishing the weldability [8].

Silicon is added to provide solid solution hardening and promote ferrite transformation [14].

Manganese in amount of *1%* to *1.5%* can stabilize super-cooled austenite (*γ-phase*), which can ensure sufficient hardenability.

Small amounts of microalloying additions (not show in Table 1-1), such as vanadium, niobiums, and titanium, are added to provide precipitation hardening.

Figure 2-1 shows *Fe-Fe_3C* equilibrium phase diagram, in which all the transformations occur in isothermal condition. DP600 steel is referred to as proeutectoid steel. It exhibits 3 types of phases depending on the temperature as shown by the *Fe-Fe_3C* phase diagram (Figure 2-1). From the transformation line A_3 to melt temperature, the DP600 structure is a single phase *γ-ferrite*. From the transformation line A_1 to the transformation line A_3, it is mixture of *γ-phase* and *α-phase*. Below the transformation line A_1, DP600 is in stable *α-ferrite* and Fe_3C.

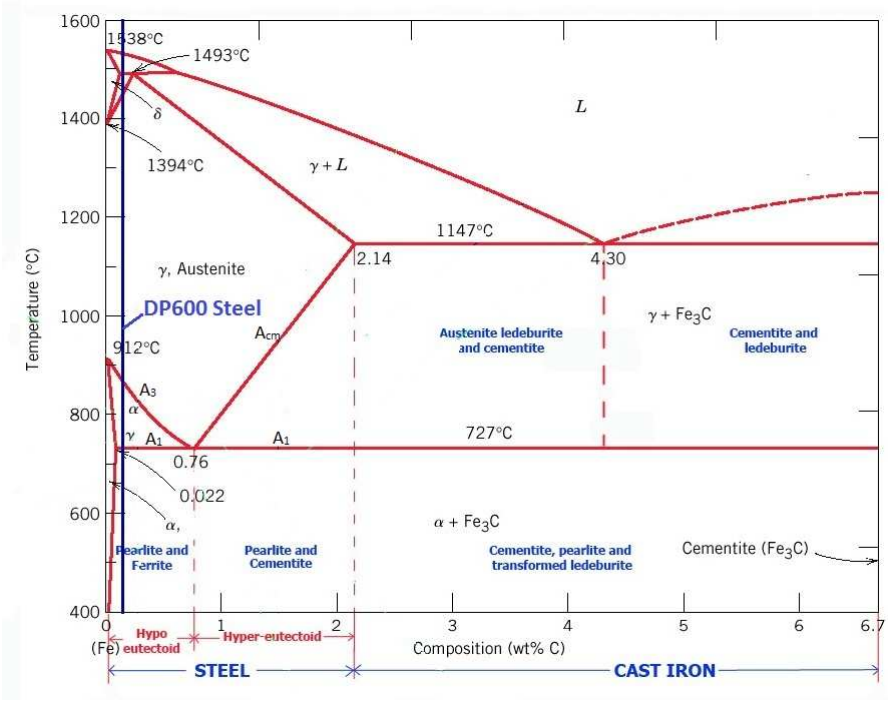

Figure 2-1. *Fe-Fe_3C equilibrium phase diagram*

Under non-equilibrium conditions, the phase transformation does not follow the equilibrium phase diagram in Figure 2-1. The microstructure can be estimated by continuous cooling transformation diagram, as shown in Figure 2-2. At high cooling rate, all the austenite can transform to martensite phase while an intermediate cooling rate could create a complex microstructure composed of ferrite, bainite and martensite. Finally, a low enough cooling rate produces the equilibrium structure consisting of ferrite and pearlite.

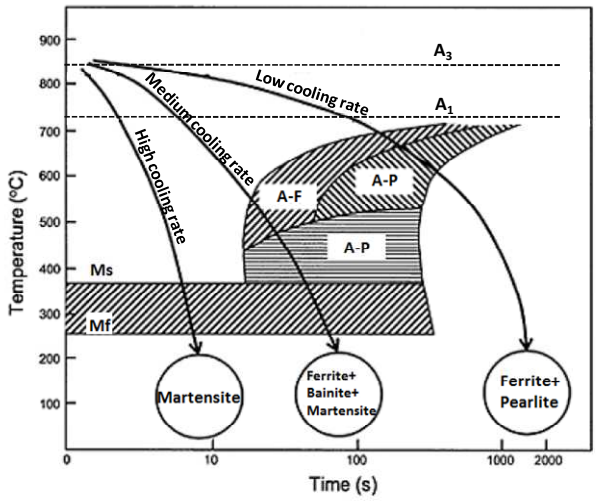

Figure 2-2. *CCT diagram of typical low carbon steel [15]*

DP600 steel can be produced by hot rolling or cold rolling process. In hot rolling process, the final deformation is carried out at a temperature above A_{r3}, as shown in Figure 2-3. After deformation, slow cooling is performed to obtain desirable ferrite by austenite decomposition, followed by the carbon enrichment in remaining austenite, which enhance the hardenability. The remaining austenite transforms to hard martensite by quick cooling before the final strip rolling.

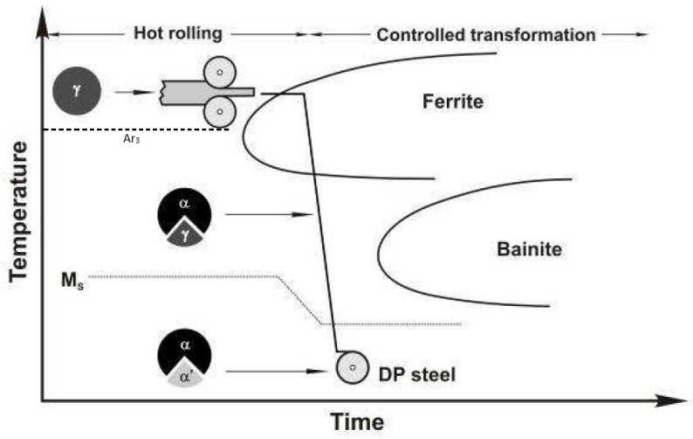

Figure 2-3. *Hot rolling schedule in the production of the DP strips [14]*

Dual phase microstructure can also be obtained by continuous annealing after cold rolling process. Figure 2-4 shows the schematic diagram of temperature changes in continuous annealing process. Steel is heated to intercritical temperature range between A_{c1} and A_{c3} and maintained for some time so that a small amount of ferrite and pearlite transforms to austenite. Then, the steel is quenched to a temperature lower than martensite start temperatures (Ms) so that the austenite phase transforms to martensite phase giving a ferrite-martensite dual phase structure [16].

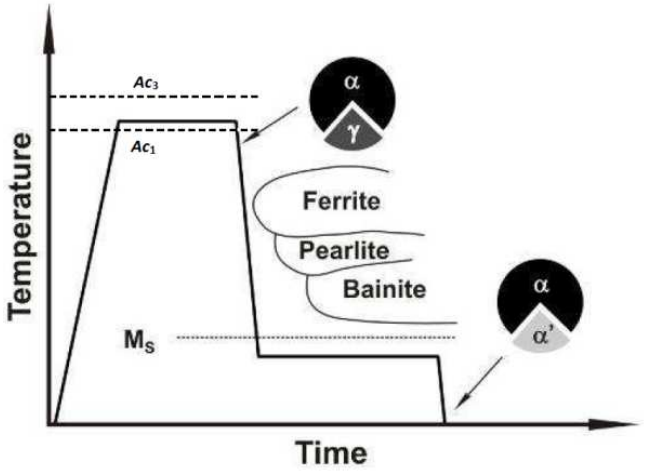

Figure 2-4. *Temperature changes during continuous annealing of DP steel sheets [17]*

2. Spot welds

Resistance spot welding is a conventional joining technology to joint sheet metal due to its advantages in superior toughness, welding efficiency and suitability for automation [18]. Consequently, it is widely used in many industrial products, such as aircrafts, automobiles bodies, truck cabins, and home applications [19]. For example, a typical car or truck may contain more than 2000 spot welds [20].

2.1. Spot welding process

Spot welding is the most common one of the various resistances welding [21]. Figure 2-5 shows spot welding pieces and machine, they consist of two or more sheet metal parts and two electrodes with adjustable forces and water cooling. The welding current is applied to the electrodes by alternative current power [22].

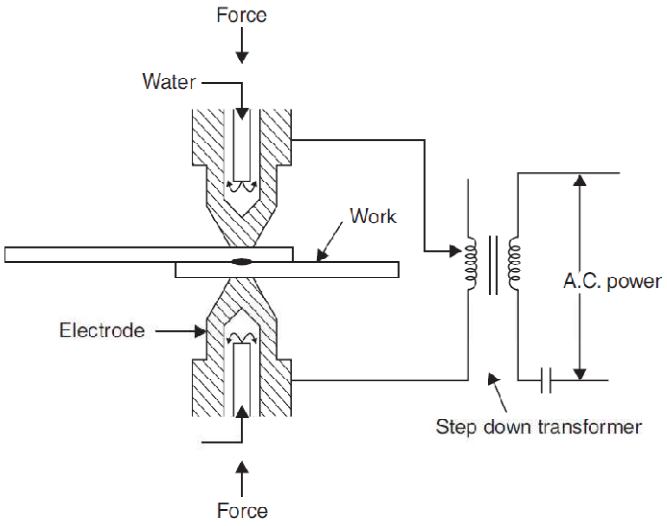

Figure 2-5. *Illustration of spot welding machine [21]*

The nuggets size is the most influential factor on the spot weld strength. A small nugget diameter usually results in low toughness and interfacial fracture [23-24]. The common criterion is that the average nugget diameter should be equal to or larger than $4\sqrt{t}$ (t is the sheet material thickness) [25]. In spot welding procedure, some adjustable resistance welding parameters can affect the nugget size and welding quality, such as welding current, weld time, electrode pressing force and electrode geometry [26].

Figure 2-6 shows welding stages to perform a spot weld. At first stage, proper pressure is applied on the electrodes for a short while (some seconds, squeeze time) to guarantee an effective

contact between electrodes and the work piece. Then instantaneous welding current is applied. The resistance heating makes the pieces temperature rise to their melting temperatures in the contact surfaces. Finally, welding force is decreased during the holding time. This post-welding time must be long enough to solidify the melted metal with the help of water cooling and base metal heat conductivity [27]. Due to high conductivity of metals, the cooling rate can be up to 10^5°C/s [28].

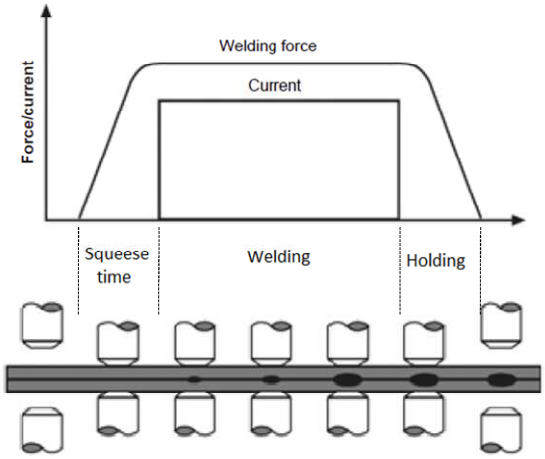

Figure 2-6. *Illustration of spot welding stages*

2.2. Spot welds microstructure

In spot welding process, the temperature distribution is not uniform in the nugget section. Figure 2-7 shows a simulated temperature field. The steel is heated up to liquid phase in the center of nugget (in red); the yellow color covers a mushy zone and a heat affected zone, corresponding to the temperature range from A_1 to molting line, as shown in Figure 2-7.

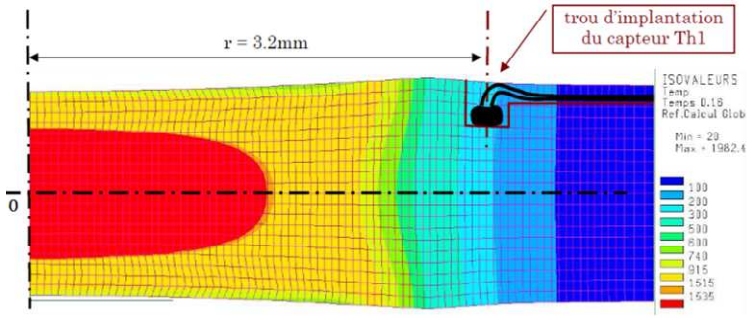

Figure 2-7. *Temperature contour in spot weld section [29]*

Furthermore, as illustrated in Figure 2-8, HAZ can be divided into austenized zone (above A_3 up to melting temperature-HAZ_2) and intercritical temperature zones (between A_1 and A_3-HAZ_2). As a result, different phases are obtained in each zone after rapid cooling. Molten zone produces solidification microstructure, including columnar grains and equiaxial crystal [15]. HAZ zone acquires refined microstructure due to recrystallization, which will be discussed in detail in Chapter 3 on DP600 steel.

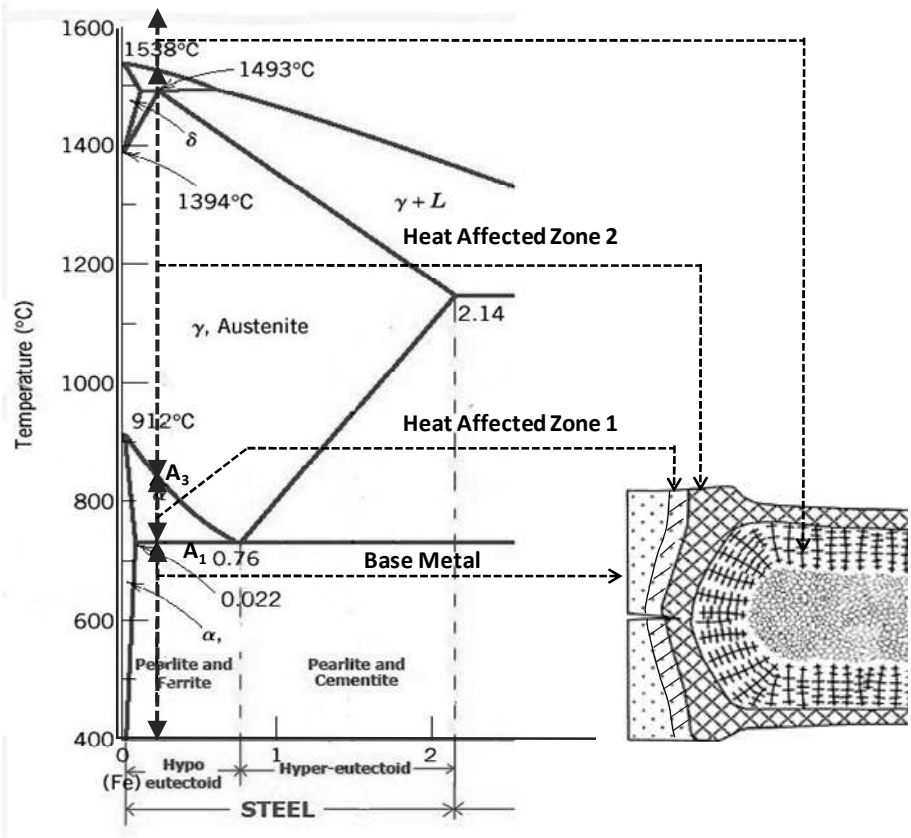

Figure 2-8. *Spot weld microstructures in different zones*

2.3. Spot welds failure modes

Several researches were conducted in order to investigate the failure mechanism of spot welds by means of experiments and numerical simulation [30-37]. All these researches evidenced three different failure modes in spot weld joint, e.g. interfacial fracture, pull-out (plug) failure and partial pull-out failure, as show in Figure 2-9. For a reliable spot weld joint, the pull-out failure is preferred because it ensures the higher peak loading and the largest energy absorption [38].

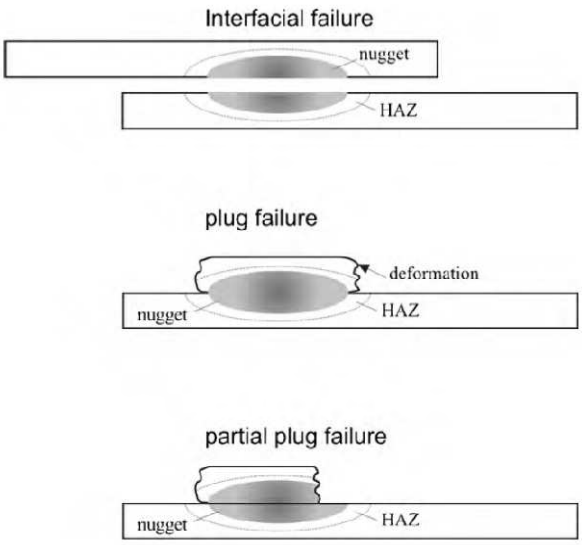

Figure 2-9. *Spot welds fail in different modes [18]*

Interfacial fracture and plug failure are two competitive processes. The cracks are caused by shear stress on faying surfaces in interfacial failure which generally leads to catastrophic damage. Plug failure is inducted by excessive plastic deformation in the heat affected zone or base metal [39]. Cracks propagate towards base metal and then terminate at outer surface of one nugget in plug failure.

3. Adhesive bonding

Adhesive bonding technology has been widely used in the long history of human being, in order to join woods, bamboos, papers, metals, etc. This joining technique aims to connect different components by means of placing liquid or soft adhesive between them. The adhesive subsequently solidifies to produce an adhesive bonding. Adhesive bonding offers various advantages over conventional mechanical fasteners as it is easy to perform, it makes it possible to join dissimilar materials, it allows for continuous connection achievement that leads to uniform stress distribution, fatigue life improvement and corrosion prevention. [40-42].

3.1. Structural adhesive

Structural bonding is gaining a competitive advantage compared to mechanical fasteners. Nowadays structural adhesive is well developed and it can cover almost all industrial application from aircraft industry, aerospace, automobile, construction to microelectronic and packaging… [43]. Different structural adhesives are developed to meet various requirements. For example, in

a typical family car, adhesive bonding allows flexible and durable connection between windshield and car body. In some shell parts assembly, like engine hoods, it permits to reduce system vibrations by soft connector between steel sheets. In order to reduce the cost and car weight, structural adhesive is more and more used to join structure components in car body-in-white, especially for joining dissimilar metals. For example, the adhesive seams measure a total length of *83 m* in the light-weight car body-Audi Q5 [44].

The properties of bonded structures are mainly affected by bonding procedure such as adhesive thickness, adherends surface preparation, curing process, etc [6]. In order to match the optimal mechanical properties, adhesive thickness is restricted to range from *0.2* to *0.5 mm*. The faying surfaces of adherends must be properly prepared to prevent adhesive failure. It should be pointed out that only cohesive failure is investigated in this work.

3.2. SikaPower-498

SikaPower®-498 is a mono-component structural epoxy adhesive. It can resist dynamic loading by adding high tough inclusions to hard matrix, providing to adhesive a viscoplastic behavior [6]. SikaPower®-498 can be applied without surface pre-treatment. In order to gain an easy and efficient application, the adhesive must be pre-heated to *60 ℃*.

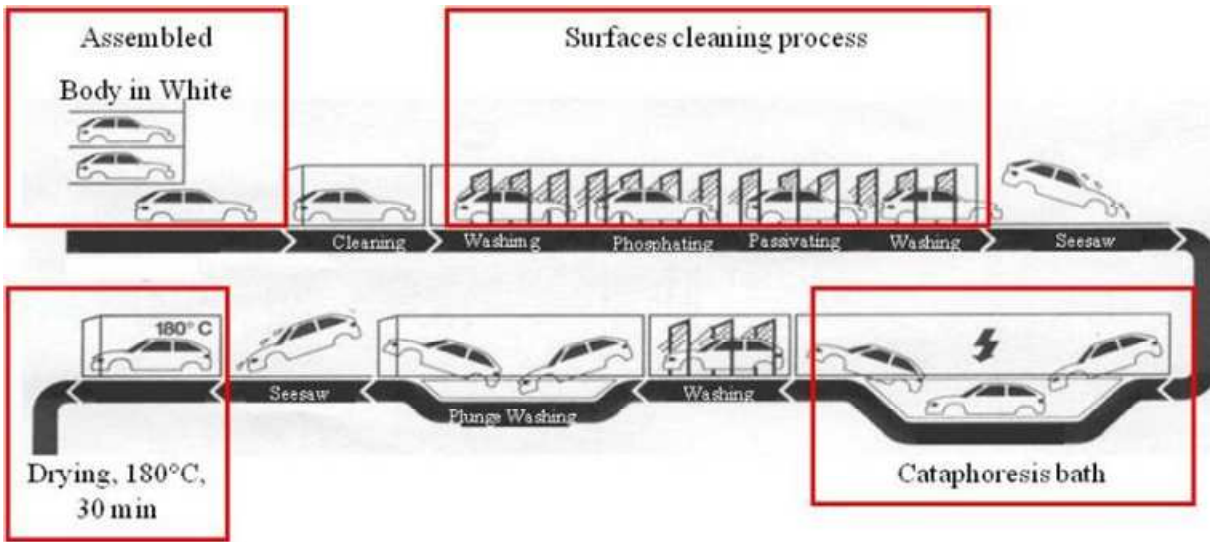

Figure 2-10. *Adhesive application in assembly chain of car body [6]*

It is designed for automated automotive assembly chains as it can resist wash-out and the cataphoresis. It allows hardening the adhesive during drying process (curing at *180 ℃* for *30 min*), as shown in Figure 2-10. SikaPower®-498 has been selected by some automotive

companies to fabricate new generation cars. In this thesis, SikaPower®-498 is combined with spot welds to produce hybrid joint. The properties data of SikaPower®-498 can be found in Appendix.

4. Weld-bonding

4.1. Motivations for weld-bonding

As shown in Figure 2-10, the adhesive may experience severe solicitations during the manufacture process of car body and sometimes before the final curing. Consequently, mechanical fasteners, such as spot welds, rivets, and bolts, are combined with adhesive bonding [44] [45-47]. Weld bonded joint is one typical hybrid joint which is mostly used in automobile industry since both spot welds and adhesive are largely used in car bodies manufactures [48-49].

On the one hand, the spot welds help to apply adhesive easily; on the other hand, the adhesive permits to reduce the number of spot welds. Some researchers show that weld bonded joints have higher strength than either spot welds or adhesive bonding, furthermore, the adhesive layer can increase stiffness of the assembled structure, reduce the vibration and corrosion of structure [40-42], increases energy absorption and improves crashworthiness. Consequently, the use of weld bonded joints in white-car-body manufacturing is quickly increasing in recent years [50]. Figure 2-11 shows Audi Q7 car body containing a large part of weld bonded joints.

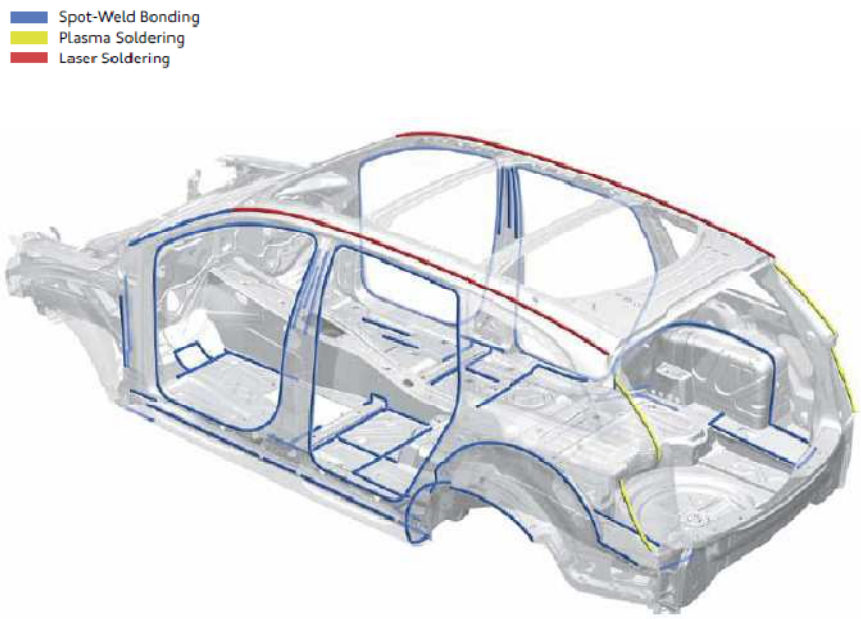

Figure 2-11. *Joining techniques in car body design (source Audi)*

There are two methods to perform weld bonding. Figure 2-12 (a) shows "flow-in" method, in which the sheets are first welded. Then low-viscosity adhesive is injected into overlap surface and subsequently cured [40].

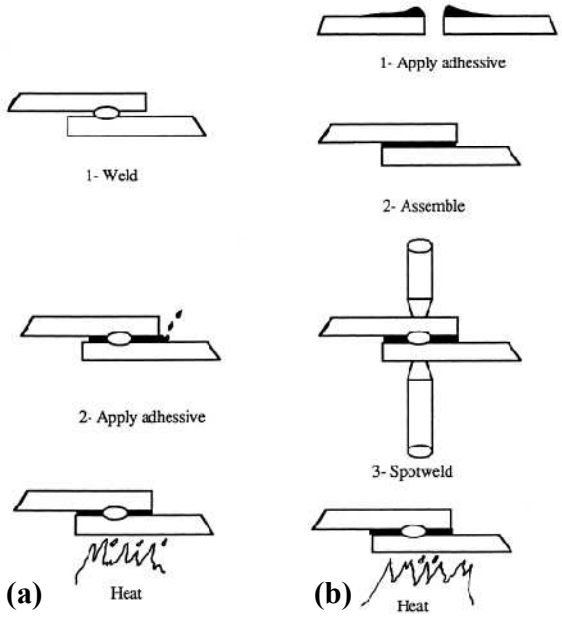

Figure 2-12. *Illustrations of Weld bonding process [40]*

Alternatively, as illustrated in Figure 2-12 (b), the adhesive is first applied on faying surface. Then the sheets are spot welded together in the center of faying surface before the curing process. The "flow-in" method requires low viscosity adhesive, which restrict the selection of adhesive. As a consequence, the second method, which is chosen in this project, is more widely used. In this work, SikaPower®-498 was selected to bond DP600 sheet and it is combined with spot welds.

Chapter 3. Joining procedures and joints characterization

In order to give an in-depth investigation into different joining methods, spot welded joint, adhesive bonded joint and hybrid joints are all investigated in this thesis. For each joint, tension, shear and complex loading are applied to calibrate the constitutive model. The so-called *KS2* specimens are used to gain different loading conditions [51]. As lap-shear specimens are widely used to evaluate spot welding failure in automobile industry [52-53], it is also investigated in this work. These specimens have benefits of simple geometry, limited experiment cost and limited experiment time. Moreover, the experiments results are reliable and reproducible. All the tests are carried out at Laboratorium für Werkstoff und Fügetechnik (LWF) in Paderborn using *1.6 mm* thickness DP600 coated steel.

In this chapter, the specimen's geometries, preparation process, experiment configurations and results are discussed in detail. Spot welds microstructure and failure mechanisms are also investigated to get precise nugget diameter. Cross-comparisons are made between the different joints.

1. Description of joining procedures

1.1. Spot welding

As discussed in section 2.1 of Chapter 2, the nuggets diameter is the most important factor that affects the strength and the energy absorption of spot welded joint. In general, small diameter can result in interfacial fracture, which is not desirable in spot welded structures as interfacial fracture has lower strength than pull-out fracture [53]. Hence, the optimal diameter of spot weld is firstly investigated. Sommer [53] gives a critical diameter of approximately *5.4 mm* for the transition from interfacial fracture to pull-out fracture under tension force on DP600 steel joint, but the sheet thickness is *1.5 mm*. The experiment is achieved in accordance with the standard *ISO 4063: 212*. Single spot weld is performed on samples of *45×45 mm* with *40 mm* overlap using CuCrZr A16 electrodes, as shown in Figure 3-1. The smallest welding current I_{min} is the one producing a minimum nugget diameter exceeding $4\sqrt{t}$ on 5 specimens [54]. The maximum current I_{max} is the current setting, decreasing from the setting where first splashing occur, that produces 3 non-splash welds, *7.6* scaled unit in Figure 3-1.

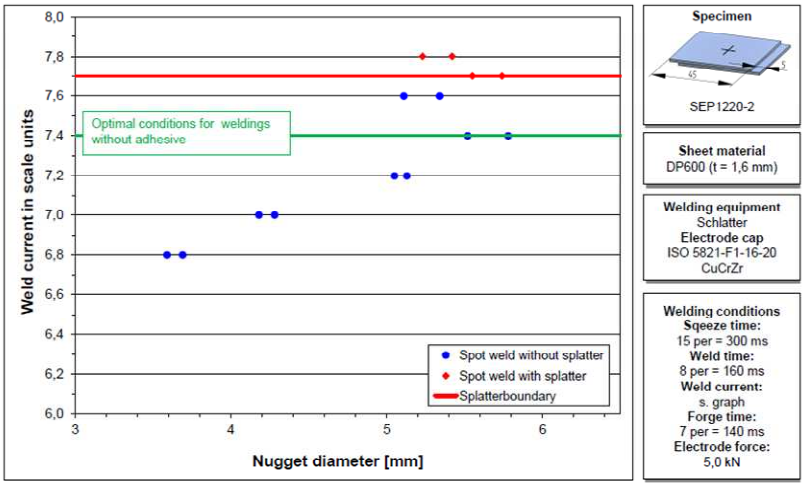

Figure 3-1 *Weldability of spot welded joint for DP600 steel with 1.5 mm thickness*

For *1.6 mm* thickness DP600 steel, the optimized welding current, welding force, squeeze time, welding time and holding time are listed in Table 3-1. Under these welding conditions, the nugget diameter is within a range from *5.4 to 5.8 mm*.

Table 3-1. *Spot welding parameters*

Welding Current In Scale Unit	**Welding Force** (*kN*)	**Squeeze Time** (*ms*)	**Welding Time** (*ms*)	**Holding Time** (*ms*)
7.4	*5*	*300*	*140*	*160*

Figure 3-2 shows a nugget metallographic cross section. The nugget diameter (ND) is *7.76 mm*, the nugget height (NH) is *2.61 mm* and the heat influenced zone diameter (HAZD) is *7.22 mm*.

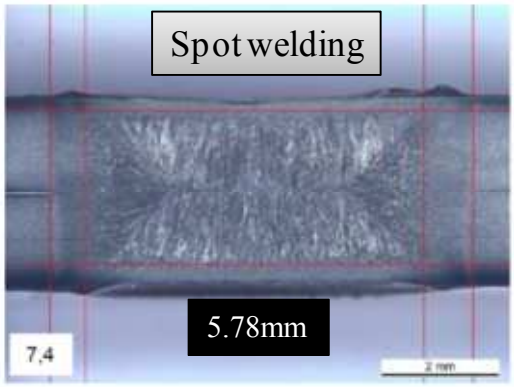

Figure 3-2 *spot weld diameter with optimized current*

1.2. Adhesive bonding

In adhesive bonded structures, the adhesive layer must have a controlled small thickness in order to have optimal mechanical properties [6]. In this thesis, the adhesive layer thickness is set to *0.3 mm* based on previous research works. To control the layer thickness and its uniformity, *0.3 mm* glass balls are added in the adhesive. It was found that the spew fillet between joined surfaces has important influence on the test result. To control this influence, the fillet is removed by specific tools as shown in Figure 3-3. For the adhesive curing, the specimens are heated at *180 °C* for *3 min* in a resistance furnace.

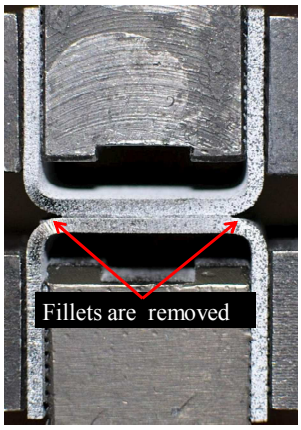

Figure 3-3 *A KS2 specimen without fillet*

1.3. Weld bonding (hybrid)

Hybrid joint combines spot weld with adhesive bonding. The presence of adhesive can significantly affect the spot welding process whereas the high temperature that results from spot welding deeply affects the adhesive in the vicinity of the spot weld. This will be discussed in detail in section 3.3.1. In this work, hybrid joining is performed in 4 steps: applying adhesive, assembling, spot welding and curing, as shown in Figure 3-4. Before applying, the adhesive should be heated at *60°C* in order to reduce its viscosity.

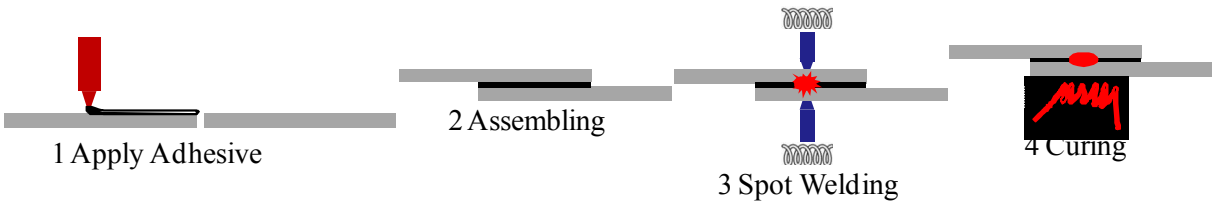

Figure 3-4 *Illustration of hybrid joint procedures*

The optimized process parameters used for spot welded joints are no longer appropriate for hybrid joints performing because the adhesive layer may modify the contact resistance. To find the optimal welding parameters, the procedure is the same as the one used for spot weld joints. Figure 3-5 clearly shows that spot welding is not complete when the current is below *7.2* in weld-bonded joint, whereas the minimum current in single spot weld is *6.8*. It reveals that the adhesive increases the electrical resistance of welding parts. Additionally, the squeeze time increases from *300 ms* to *500 ms* to improve the conductivity.

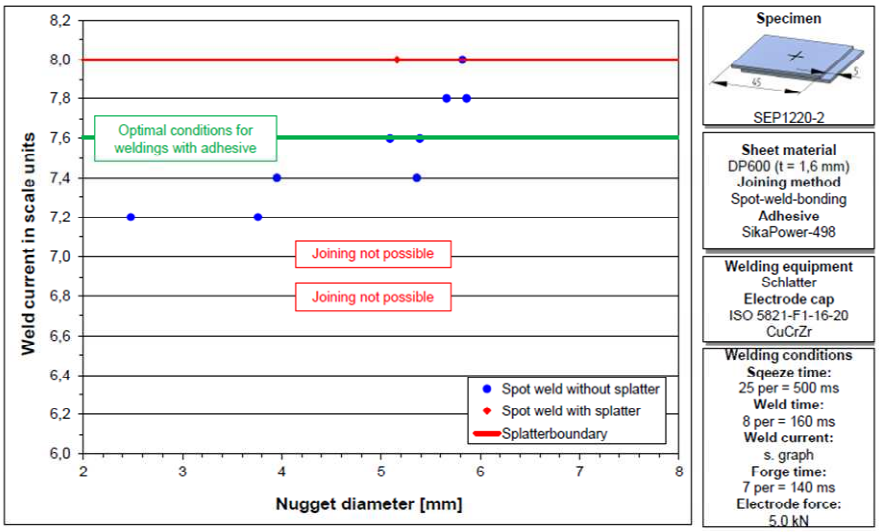

Figure 3-5 *Weldability of weld bonded joint*

Spot welding parameters in weld bonding are listed in Table 3-2, corresponding to a nugget diameter within a range of *5* to *5.5 mm*.

Table 3-2. *Welding parameters in weld bonding*

Welding Current In Scale Unit	**Welding Force** (*kN*)	**Squeeze Time** (*ms*)	**Welding Time** (*ms*)	**Holding Time** (*ms*)
7.6	*5*	*500*	*140*	*160*

Figure 3-6 shows a hybrid joint metallographic cross section. The measured nugget diameter is *5.39 mm* but the investigations of several specimens reveal that the nugget diameter is ranging between *5 mm* and *5.5 mm*.

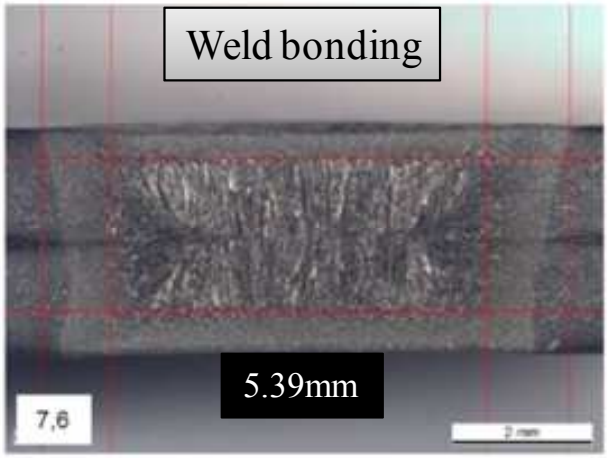

Figure 3-6 *Metallographic of spot weld in hybrid joint*

2. Description of simple characterization tests

All the tests are carried out using quasi-static loading with a velocity of *10 mm/min* under room temperature on a universal tension and compression testing machine (*Zwick Z100*) with a capacity of *100 kN*. The global displacement is measured by machine internal sensor. For each test, at least 5 specimens are tested to ensure the reliability of experiment. In order to calibrate constitutive model of different joints, KS2 specimen of SW, AB and WB joint are conducted in shear, tension and peeling.

2.1. KS2 test

KS2 specimens refer to combined tension-shear specimens. It is constituted by two "U" shaped parts, as shown in Figure 3-7 (a). Different joining methods can be applied to the faying surfaces, e.g. adhesive bonding, spot welding and hybrid joining. The adjustable fixture system gives control on the load direction. In this work *0°* (tension loading) and *90°* (shear loading) load directions are investigated. With the specially designed fixture system [51], local displacement is measured with the help of a digital image correlation (DIC) system between point 1 and point 2, as shown in Figure 3-7 (a). The measurement of local displacement for peeling is not shown here. The reference points are in the same location as KS2 specimens. The specimens are tested using a universal tension-compression testing machine as shown in Figure 3-7 (b). In fact, both global and local displacements are outputted but only the latter are used to be discussed and be compared with simulation.

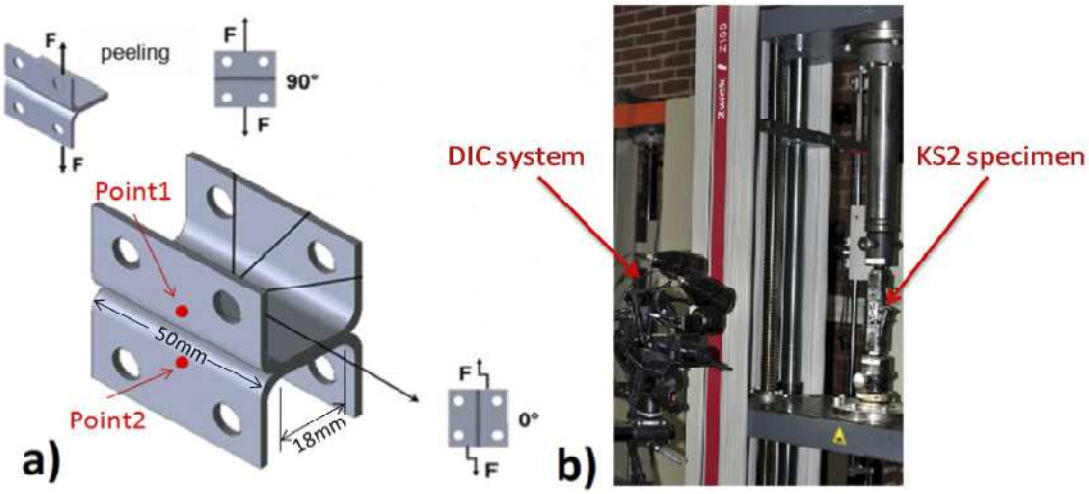

Figure 3-7 *KS2 specimens, a) schematic of KS2, b) universal tension machine*

KS2 specimen geometry is depicted in Figure 3-8. The faying surface is *50mm×18mm*. Four holes are drilled to fix the specimens on the clamps. The peeling test has the same faying surface as well as KS2 specimens. The geometry is depicted in Figure 3-9. The force is applied on the edges, as shown in Figure 3-7 (a) peeling.

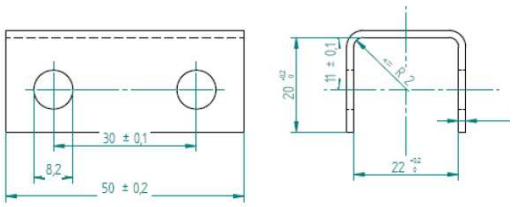

Figure 3-8 *Geometry of KS2 specimen*

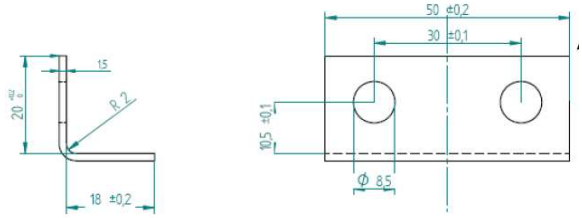

Figure 3-9 *Geometry of peel specimen*

2.2. Lap-shear tests

Lap-shear test is widely used for assessment of mechanical characterization of joints, like spot weld and adhesive, due to its simple geometry [55-58]. In lap shear tests, spot welds or adhesive bonding is carried out on the over-lapping surface, which is *16mm×45mm* in this work. Lap-shear has *100 mm* free clamping length. The two ends of extensometer, with *22 mm* gauge length, are fixed on both sides of the joint. Lap-shear geometry is shown in Figure 3-10. The faying surfaces can rotate with the loading in lap-shear differing from KS2 shear tests. In KS2 the faying surfaces are fully constrained by the grips.

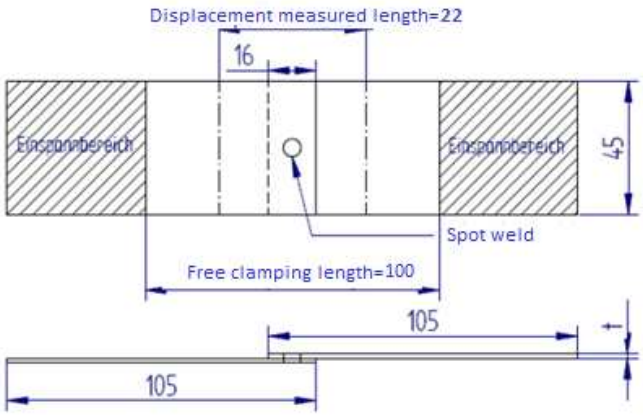

Figure 3-10 *Lap-shear geometry*

3. Test results

The results of different joints are discussed separately in this section. The discussion focuses on the microstructure of spot weld, the interaction between spot weld and adhesive, the measurements of force-displacement of each tests and the cross comparison of ultimate strength and damage energy.

3.1. Test results of spot welded joints

3.1.1. Structure of spot welds with DP600

Spot weld microstructure has significant influence on its mechanical properties. In what follows, spot weld microstructure with DP600 steel is investigated to assess the welding quality and nugget's dimension.

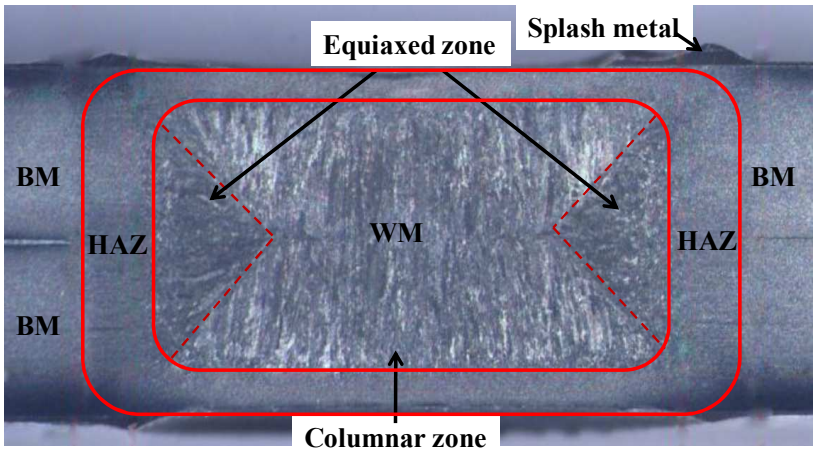

Figure 3-11 *Macrostructure in transverse section of spot weld*

The macrograph of spot weld transverse section depicted in Figure 3-11 shows that the spot weld consists of WM, HAZ and BM. The investigated cross sections are free of any defect. In the WM zone, liquid metal transforms into solidification structure, which can be divided into columnar zone and equiaxed zone. The metal in contact with electrodes is rapidly cooled and forms columnar zone with growing orientation perpendicular to contact surface. Equiaxed crystal is acquired in the zone adjacent to BM which can affect the solidification process of WM. The splashed metal can be observed in the vicinity of spot welds.

The specimen is polished and then etched with *4%* nital solution. The microstructure is investigated with the help of AFM in our laboratory. Figure 3-12 shows the microstructure in the different zones of spot welds.

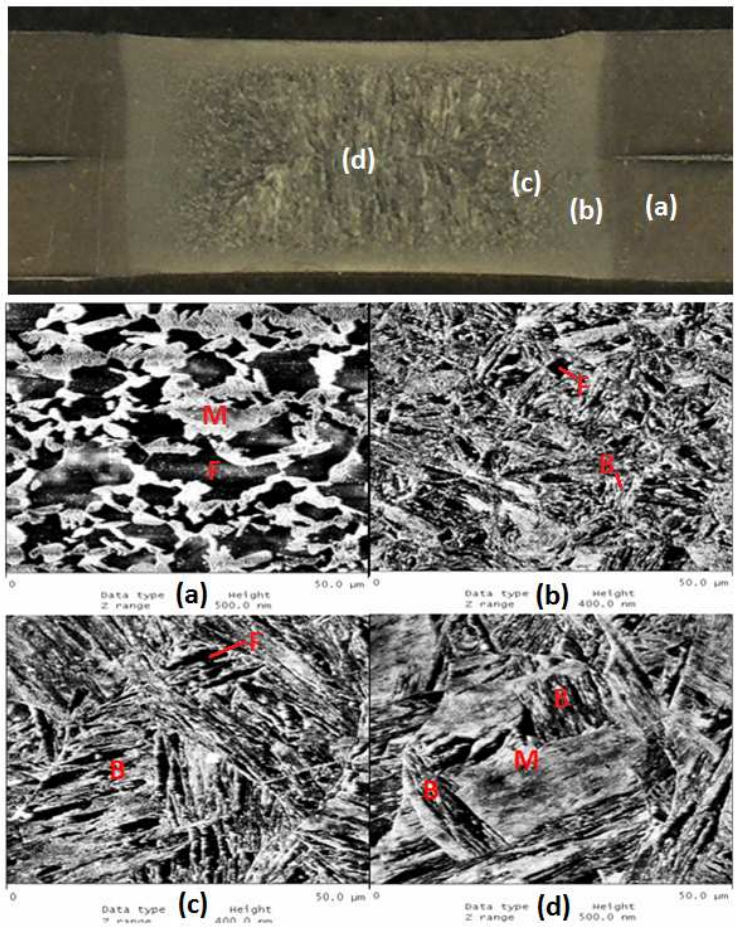

Figure 3-12. *Sample distribution on macrostructure (left-up) and AFM microstructure images (a)Base metal, (b) Tempered zone, (c) Quenching zone, (d) the center of welded metal*

Figure 3-12 (a) shows the microstructure of BM. It contains martensite (in white) islands dispersed through soft ferrite matrix (in dark). The heat affected zone, as shown in Figure 3-12 (b), was heated above recrystallization temperature. It is thus the seat of austenite to bainite transformation with small amount of residual ferrite. Figure 3-12 (c) shows the border of the welded metal (melted zone). It consists of bainite structure and a small quantity of ferrite. The center of melted zone generates a complex microstructure containing bainite and martensite, as depicted in Figure 3-12 (d). The microstructures of spot weld are in accordance with the literatures [27] and [59].

Figure 3-13 shows hardness tests results in the transverse section. It shows that the hardness distribution is in agreement with the microstructure observations. On average, WM has the maximum hardness *375 HV* and it exhibits large hardness variations that result from the heterogeneities in solidification structure, e.g. dendrite and the solidification defects. Comparatively, soft base metal exhibits lower hardness in BM zone. In HAZ, the hardness is intermediate between those of BM and WM.

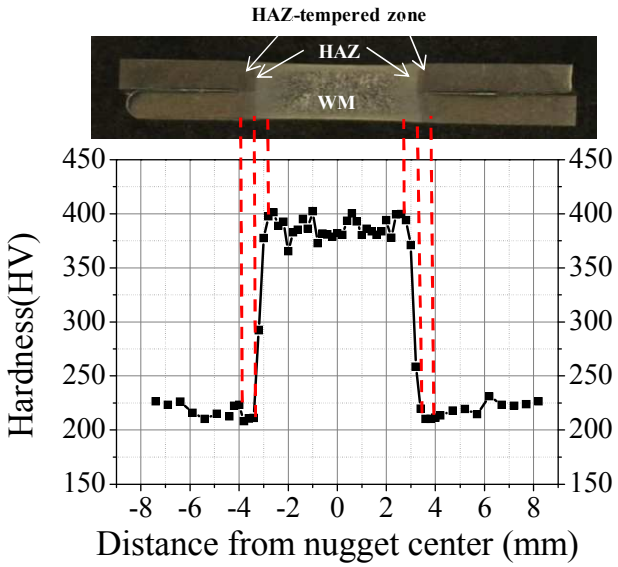

Figure 3-13. *Micro hardness distribution in spot weld transverse section*

3.1.2. Failure modes and load bearing capacity of spot weld joints

In spot welding, the plates are joined by welded zone. Hence, spot weld diameter is the key factor to influence the spot weld strength. Moreover, the HAZ and BM properties have significant influence on the fracture modes. Generally, a competition between two failure modes

is observed. These modes are the pull-out (plug) fracture and the interfacial fracture. Figure 3-14 shows the different fracture mode. The dotted lines represent potential crack path. In path (a), the strain localization leads to fracture in BM [60]. In path (b), (c) and (d), the crack initiates at the notch tip but it then propagates following different potential paths. Path (b) is located in the boundary BM/HAZ, path (c) is along the boundary HAZ/WM and path (d) produces partial pull-out fracture. In this case the crack propagates along the front of dendrite structure but the path can change when crack meets some localized defects that are common in welding structure.

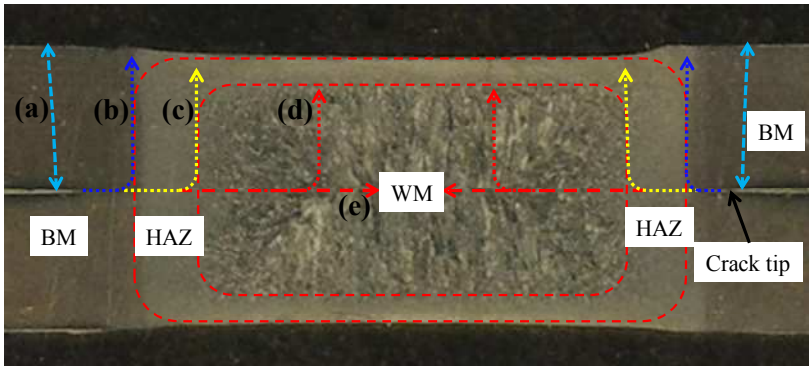

Figure 3-14. *Crack paths in different fracture mode of spot welded: (a) strain localization in BM, (b) pull-out in BM/HAZ, (c) pull-out in HAZ/WM, (d) partial pull-out in WM and (e) interfacial fracture*

In this work, the pull-out fracture mode at the HAZ/WM interface and the interfacial fracture mode are observed corresponding to tension and shear loading. This will be discussed in details in the following section.

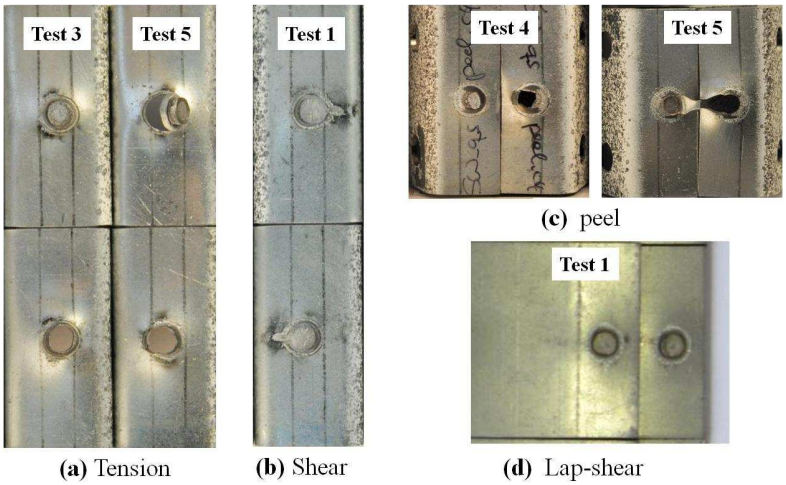

Figure 3-15. *Fracture modes of spot welded joint: (a) KS2 tension, (b) KS2 shear, (c) peel, (d) lap-shear*

In the tension test (KS2 *0*°) that corresponds to mode-I opening fracture, the spot weld shows pull-out fracture under tension force, as shown in Figure 3-15 (a). The average ultimate strength is *11.8 kN*, as shown in Figure 3-16 (a). The ultimate strength is well reproduced. The displacements at fracture are scattered and range between *5.7 mm* and *13* mm. The most important difference is observed between Test 3 and Test 5. It mainly comes from the different damage modes. In Test 3, the nugget separates from one side of the base metal; it experiences pull-out fracture, as shown in Figure 3-15 (a). Contrary, in Figure 3-15 (a) Test 5, the nuggets separate from the two sides of base metal.

In the shear tests the fracture mode-II is dominant. Therefore, all the specimens fail in interfacial fracture mode as shown in Figure 3-15 (b), which is not expected in the operating conditions. This kind of failure occurs without noticeable deformation and without warning. In addition, the interfacial fracture is not appropriate for crashworthiness as it has low energy absorption. In shear tests, the average ultimate strength is *20.8 kN*, as shown in Figure 3-16 (b). Average displacement is about *1.0 mm*. The ultimate strength of Test 2 and Test 5 are about *2 kN* lower than the other tests, this probably comes from the difference of nugget diameter.

Under peel, the crack initiates at HAZ/BM interface, and then it propagates in the vicinity of spot weld. There are generally two fracture modes namely the pull-out fracture depicted in Figure 3-15(c) Test 4 and the tearing fracture depicted in Figure 13-5 (c) Test 5. In tearing mode, crack propagates from nugget to the outer border of base metal in a longer path than pull-out mode. Consequently Test 5 shows the maximum displacement before the complete failure. Peel test has maximum average strength of about *3.1 kN*. The displacement scatters from *8.3 mm* to *19.2 mm*, as shown in Figure 3-16 (c).

Figure 3-15 (d) shows that lap-shear test exhibits interfacial fracture mode. Further analysis reveals that in lap-shear test, the spot weld experiences complex loading combining shear and tension. In fact the spot weld can rotate about an axis perpendicular to loading direction. Figure 3-16 (d) shows lap-shear force-displacement curve. The average ultimate strength is *15 kN*, lower than shear force. Due to the rotation of spot weld, the displacement is larger than that of pure shear.

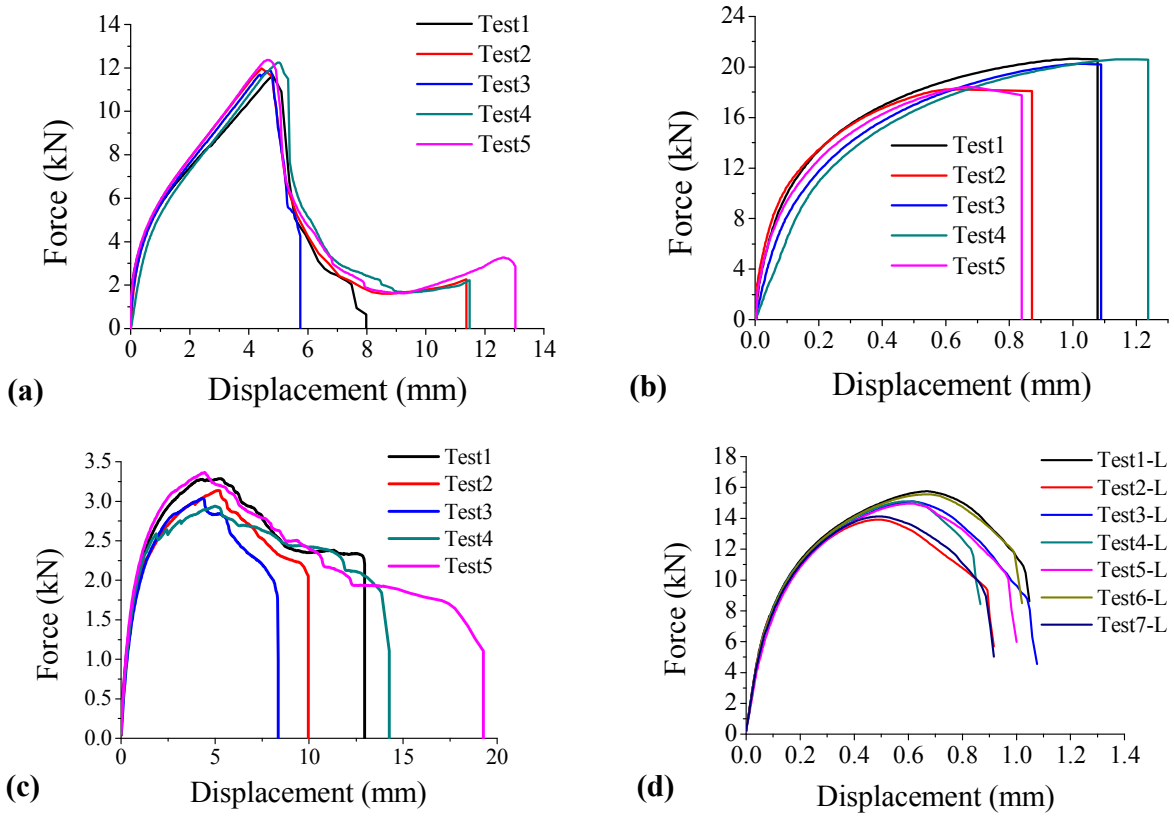

Figure 3-16. *Force-displacement curve of spot welded joint: (a) KS2 tension loading, (b) KS2 shear loading, (c) peeling, (d) lap-shear*

3.2. Test results of adhesive bonded joints

3.2.1. Load bearing capacity and failure modes of adhesive bonded joints

The adhesive is applied on the faying surface of KS2 through the usual strictly prescribed procedure. The adhesive fillets are removed from both edges to reduce the fillet influence. The specimen is then heated at *180 °C* for *3 min* in resistant furnace. Adhesive layer thickness is set to *0.3 mm* in order to ensure the optimal mechanical properties.

In tension test, the ultimate strength scatters from *7 kN* to *10 kN*. Test3 has the minimum force *6.8 kN* while Test 5 has the maximum force *10.1 kN*, as shown in Figure 3-17 (a). In Figure 3-18 (a), a dark black zone is observed in the center of fracture surfaces. This is probably due to the large strain rate in this zone caused by the release of the elastic strain energy stored in the adherends.

In shear test, adhesive bonded joint shows noticeable mechanical property against shear force, up to *34 kN*, as shown in Figure 3-17 (b). In peel, the adhesive exhibits the lowest ultimate

strength about *5 kN*, as shown in Figure 3-17 (c). Average ultimate strength of lap-shear joints is *23.1 kN*, lower than that *34 kN* in KS2 shear. The reason is that faying surfaces in lap-shear joint is smaller than shear KS2, *720 mm*^{2} compared with *900 mm*^{2}. Moreover, lap-shear joints undergo the component of tension load due to the rotation of faying surfaces.

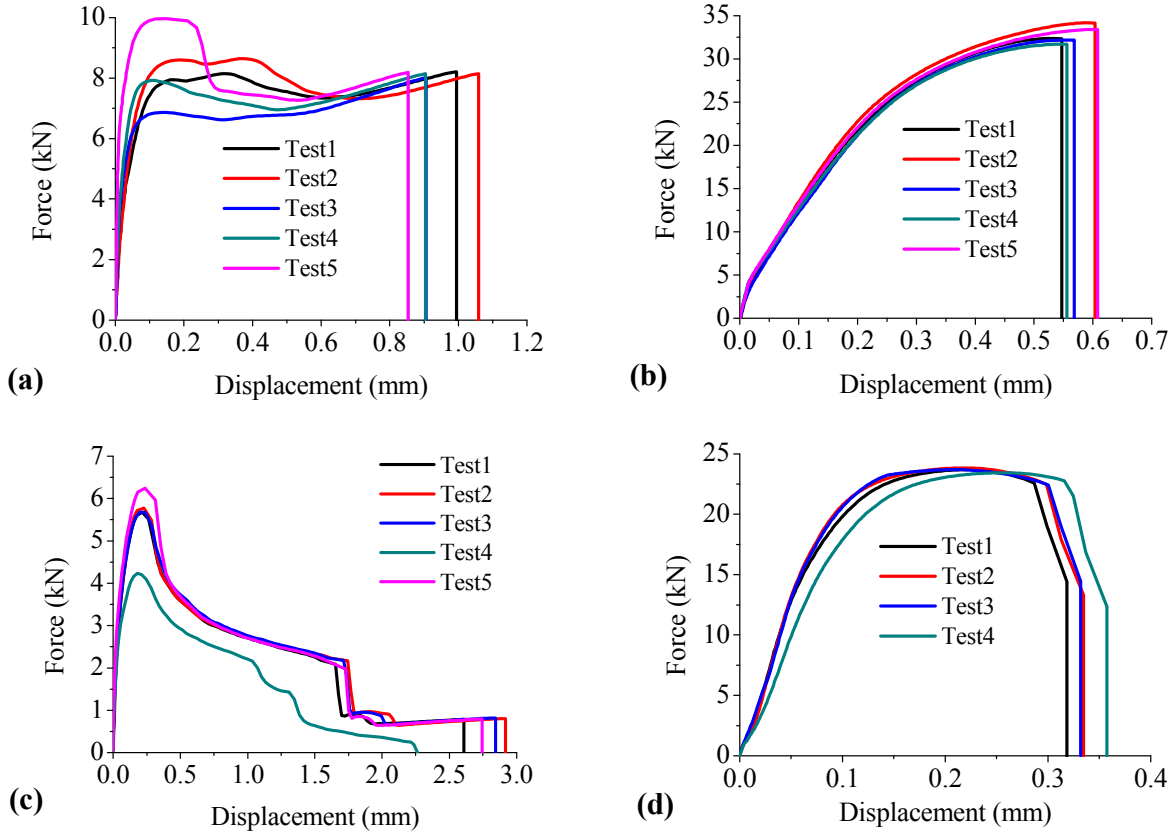

Figure 3-17. *Force-displacement curve of adhesive bonded joint: (a) tension loading, (b) shear loading, (c) peeling and (d) lap-shear*

The damaged specimens are depicted in Figure 3-18. A dark black zone is observed in damaged interfaces of tension test, as shown in Figure 3-18 (a). The reason is that the adhesive damaged under different strain rate. The adhesive layer has almost unique stain rate at the beginning of loading. However, when the adhesive layer remain a small zone before final damage, the strain rate may be large than the other zone. Similar phenomenon of damage can be observed in peeling test, as shown in Figure 3-18 (b). As regards KS2 shear and lap-shear, the both damaged surfaces are in the same colour. This also indicates that adhesive bonded joint has uniform stress distribution than that of tension and peeling loading.

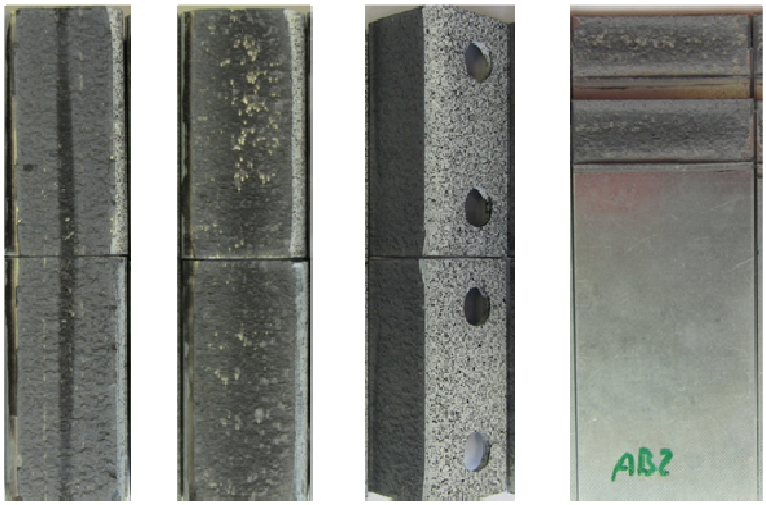

Figure 3-18. *Fracture modes of adhesive bonded joint: (a) tension, (b) shear, (c) peel and (d) lap-shear.*

3.3. Test results of hybrid joints

3.3.1. Interaction between bonding and welding

The macrostructure of weld bonded joint is depicted in Figure 3-19. The typical solidification structure is formed in the center of spot weld nugget, as shown in Figure 3-19 (a) [22]. There are no visible defects or voids found in WM. There is no apparent difference of hardness in WM between SW and WB. Werber *et al.* [5] also reported that the hardness and microstructure of spot weld is not influenced by the adhesive in weld bonded joint.

In Figure 3-19 (b), the adhesive in WM is burnt by the heat of spot welding. In HAZ and its peripheral zone, adhesive is deteriorated by the heat of spot welding. Hence, the adhesive in these zones, with width of 2 mm, cannot effectively join the BM together. In addition, a channel, which connects HAZ with exterior edge of specimen, was found in adhesive layer. The adhesive in fusion zone was burnt into high pressure gas, which damages the viscous uncured adhesive layer and escapes from WM zone. The channel leads to discontinuity of adhesive layer. It should be noted that the effective bonding surface of weld bonded joint is smaller than that of adhesive bonded joint due to spot weld process.

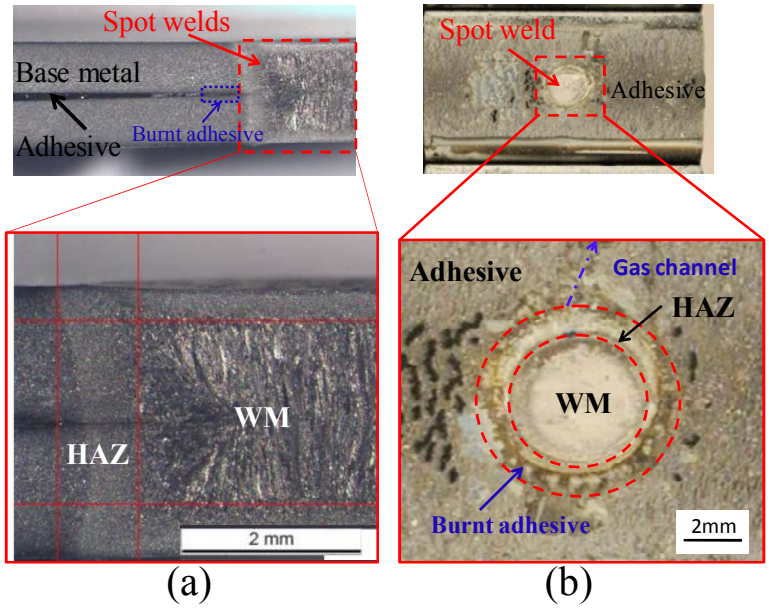

Figure 3-19. *Macrostructure of weld bonded joint: (a) transverse section, (b) in-plane section*

3.3.2. Load bearing capacity and failure modes of weld bonded joints

Weld bonding combines adhesive bonding with spot welding. The complex structure leads to two stage failure in WB: adhesive failure and spot weld failure. Two stage failures are observed in tension, peeling and lap-shear tests, as shown in Figure 3-20. Spot weld exhibits higher strength than adhesive under tension and peeling load. In tension test, the ultimate strength of Test 3 is *22.7%* higher than the other tests, as depicted in Figure 3-20 (a). It is observed that in Test 3, the cracks initiate in BM/HAZ while it initiate in HAZ/WM in the other tests, as shown in Figure 3-21 (a). The ultimate strengths of peeling are scattered ranging from *3.7 kN* to *5.4 kN*. This could be explained by the variation of nuggets diameters, as shown in Figure 3-21 (c).

Spot weld failure peak was not observed in force-displacement curve of KS2 shear tests, as shown in Figure 3-20 (b). This indicates that the spot weld fails prior to the adhesive layer. The reasons will be discussed in section 3.4.

Pull-out fracture of spot weld was observed in tension, as shown in Figure 3-21 (a). It should be pointed out that the crack initiated from BM/HAZ in Test 3 while it takes place in HAZ/WM in the other tests. It indicates that spot welds in weld bonded joint are prone to damage in HAZ/WM. This phenomenon can be proved when investigating the T-joint test. Interfacial fracture was observed in shear and lap-shear tests, as depicted in Figure 3-21 (b) and (d). Pull-out

fracture of spot weld was observed in peeling, but the crack can propagate to the base metal, as shown in Figure 3-21 (c).

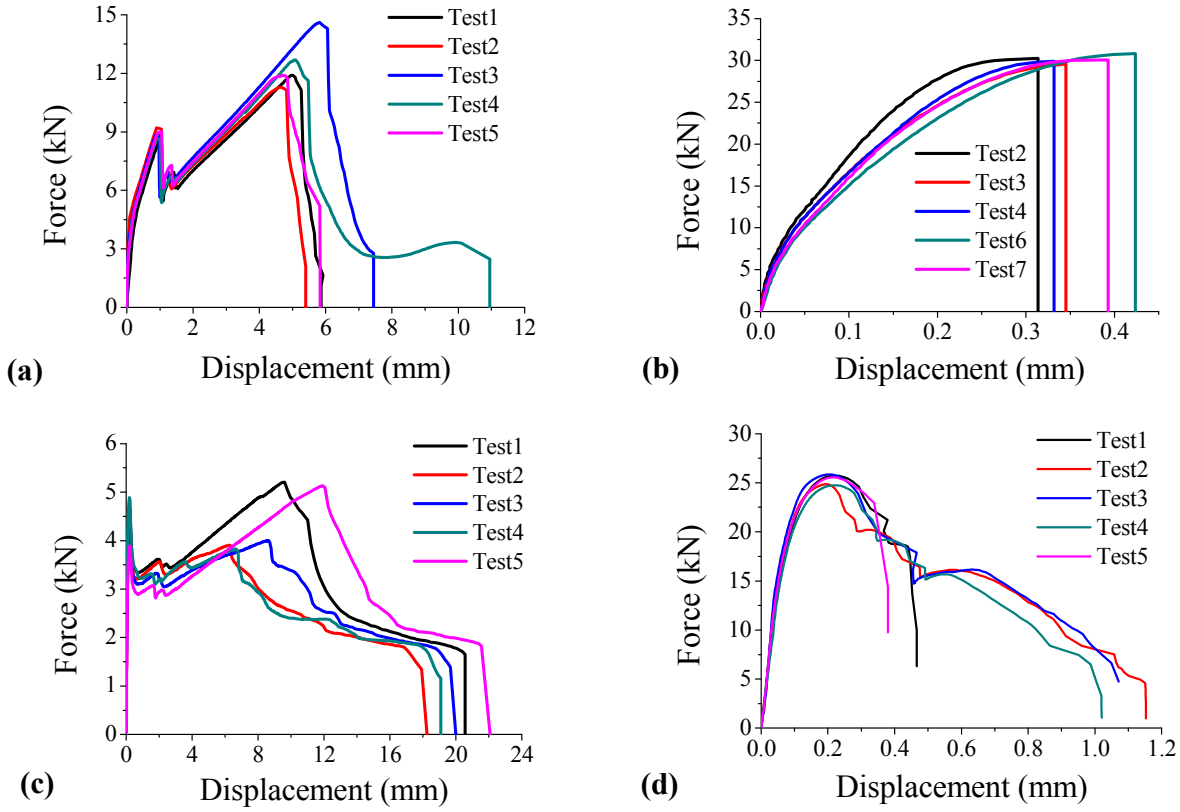

Figure 3-20. *Force-displacement curve of WB joint: (a) tension, (b) shear, (c) peel and (d) lap-shear*

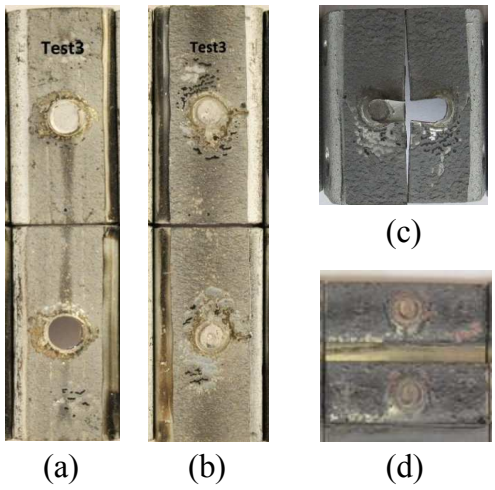

Figure 3-21. *Images of WB joint fracture: (a) tension, (b) shear, (c) peeling and (d) lap-shear.*

3.4. Comparisons between test results of different joints

In order to assess the behavior of different joining methods, tests results are compared in terms of load bearing capacity and energy absorption under the same loading condition. WB joint provides excellent properties in both load bearing and energy absorption under tension loading, as shown in Figure 3-22. WB joint combines high stiffness of adhesive and large plastic deformation of spot weld, as shown in Figure 3-22 (a). The energy absorption of WB joint is increased by *19.9%* compared with SW joint while this value is increased by *8 times* compared with AB joint, as shown in Figure 3-22 (b). A small amount of adhesive added to spot weld can markedly increases the ultimate strength and energy absorption.

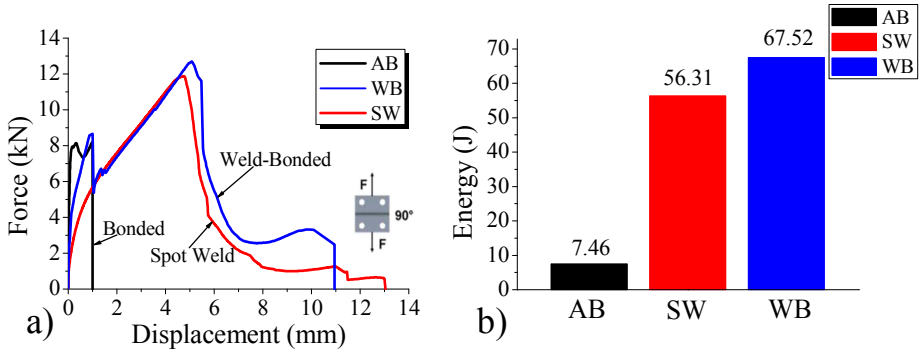

Figure 3-22. *KS2 tension test: a) force-displacement curve, b) energy absorption*

Figure 3-23 (a) shows load capacities and energy absorptions of different joints under shear loading. SW joint exhibits the lowest loading capacity among the three joints but it has the largest displacement before complete failure. As a result, SW joint provides the largest energy absorption, increased by *1.46 times* compared with that of WB joint.

AB joint exhibits the highest ultimate strength among the three joints while its energy absorption is lower than that of SW joint.

The ultimate strength of WB joint is lower than that of AB joint due to the diminishment in adhesive surfaces by spot welding process and also some adhesive deterioration. It is notable that WB joint has the lowest energy absorption among the three joints. The contributions of plastic deformation to energy absorption are limited because spot welds fails prior to adhesive under shear force.

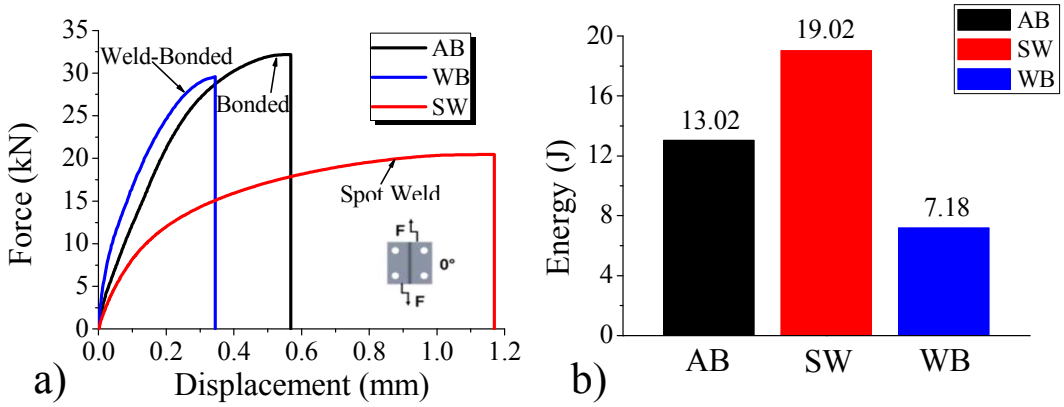

Figure 3-23. *KS2 shear: a) force-displacement curve, b) energy absorption*

Force-displacement curve under peeling is depicted in Figure 3-24 (a). AB joint and WB joint acquire high stiffness from adhesive layer. Hence both them exhibit higher ultimate strength than that of SW joint. In addition, the large deformation of spot welds enables WB joint to improve the energy absorption, which is increased by *8.5 times* compared with that of AB joint, as shown in Figure 3-24(b).

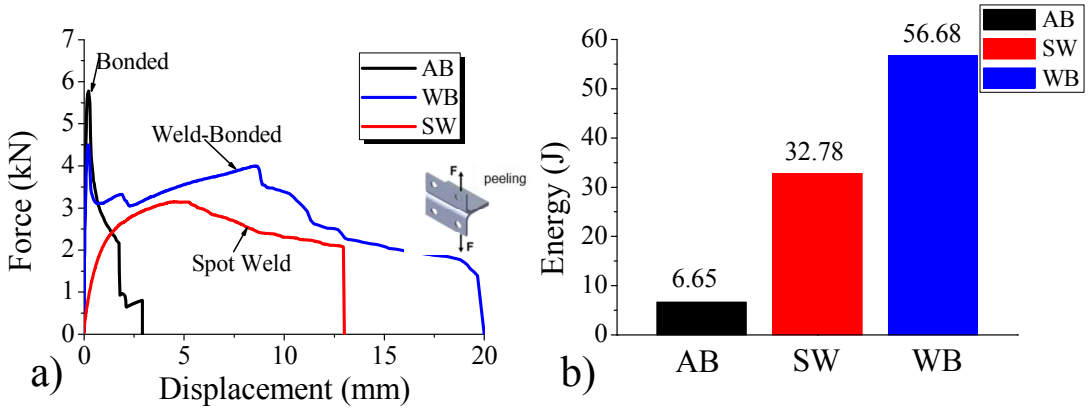

Figure 3-24. *Peel test: a) force-displacement curve, b) energy absorption*

In lap-shear, the joined zone has a slight rotation which leads to a combined load on the faying surface (shear and separation). As a consequence, lap-shear joint fails under tension and shear complex load. AB joint and WB joint exhibit higher ultimate strength than that of SW joint, as shown in Figure 3-25 (a). WB joint offers the highest energy absorption among the three joints, as shown in Figure 3-25 (b).

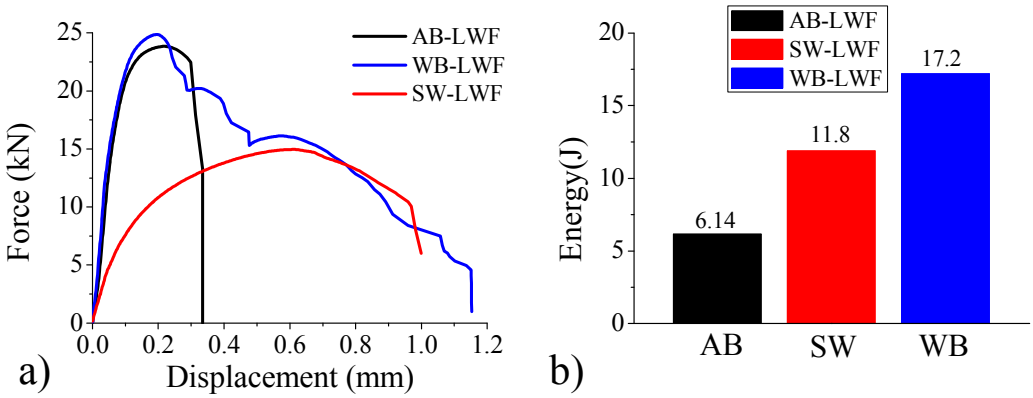

Figure 3-25. *Lap-shear test: a) force-displacement curve, b) energy absorption*

3.5 Conclusion

Welding parameters are optimized for spot welding and adhesive bonding in terms of welding current, squeeze force and squeeze time. A complex structure of columnar grains and equiaxial grains is formed in molten zone of SW. The materials are hardened in HAZ due to phase transformation as evidenced by the hardness tests.

WB joint is successfully produced by combining SW with AB. The adhesive is burnt in the vicinity of spot weld nugget due to the heat of SW. Adhesive layer must have a controlled small thickness in order to have optimal mechanical properties, *0.3 mm* for SikaPower®-498 in this work.

KS2 and lap-shear specimens are used to assess the different joining techniques (SW, AB and WB) under tension, shear and peeling load.

SW joint always provides excellent energy absorption due to the large plastic deformation in base metal. SW joint exhibits the highest ultimate strength under tension among the three joints, whereas it lacks capacity to sustain pure shear force.

AB joint can provide high stiffness under complex loading condition while it exhibits noticeable high ultimate strength under shear force. AB joint has lower energy absorption due to the lack of ductility compared with SW joint.

WB joint is a compromise solution between AB joint with SW joint. It exhibits two stages failure: adhesive failure and spot weld failure except KS2 pure shear. WB joint can benefit from the AB high stiffness and the SW large plastic deformation. As a consequence, WB joint offers largest energy absorption under tension and peeling among the three joints. In pure shear (KS2 shear), WB joint particularly exhibits the lowest energy absorption among the three joints.

Chapter 4. Numerical aspects

1. Constitutive Models

1.1. Elastoplastic model with damage

For linear elastic behavior, the stress increases proportionately with the strain. Hooke's law represents the material behavior and relates the stress to the strain. The general Hooke's law equation [63] states:

$$\boldsymbol{\sigma} = \mathbf{C} \times \boldsymbol{\varepsilon} \tag{4.1}$$

where $\boldsymbol{\sigma}$ is Cauchy stress tensor, $\boldsymbol{\varepsilon}$ is strain tensor; $\boldsymbol{C}$ is a fourth-order constitutive tensor.

For isotropic materials, $\boldsymbol{C}$ can be fully determined with the help of two material parameters: the bulk modulus K and the shear modulus G, that quantify the material's resistance to changes in volume and shear (isochoric) deformations, respectively.

Hooke's law for isotropic materials can then be expressed as a function of the Young's modulus E and Poisson's ratio v [64]

$$\boldsymbol{\sigma} = \lambda \operatorname{tr}(\boldsymbol{\varepsilon})\mathbf{I} + 2\mu\boldsymbol{\varepsilon} \tag{4.2}$$

where $\mathbf{I}$ is the second order identity tensor. λ and μ are Lamé's parameters:

$$\lambda = \frac{\nu E}{(1+\nu)(1-2\nu)} \tag{4.3}$$

and

$$\mu = \frac{E}{2(1+\nu)} \tag{4.4}$$

A typical stress-strain curve of steel loaded under purely uniaxial tension is plotted in Figure 4-1. The total strain can be partitioned into two parts: an elastic part and a plastic part. This additive partition of strain is generally used [65]

$$\boldsymbol{\varepsilon} = \boldsymbol{\varepsilon}^{\mathrm{e}} + \boldsymbol{\varepsilon}^{\mathrm{p}} \tag{4.5}$$

where $\boldsymbol{\varepsilon}^{\mathrm{e}}$ is the elastic strain and $\boldsymbol{\varepsilon}^{\mathrm{p}}$ is the plastic strain.

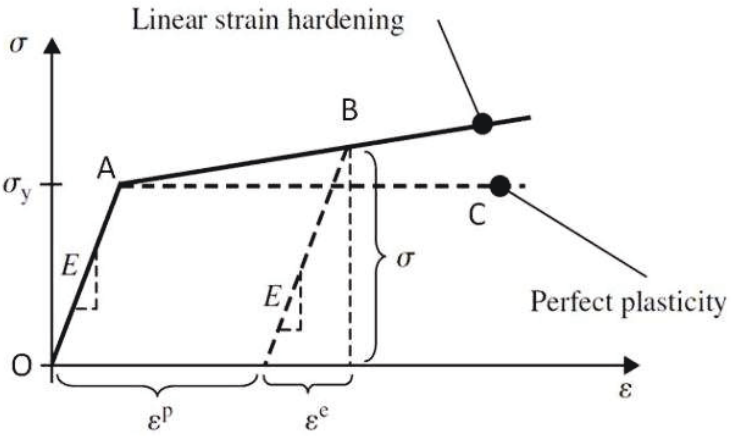

Figure 4-1. *Stress-strain curve of a metal specimen under uniaxial loading [65]*

In this thesis, a classical von Mises isotropic yield criterion was used. The material starts yielding when the von Mises stress reaches a critical value σ_y.

The yield function can be expressed as [66]:

$$f_y = \sigma_e - \sigma_y = \left(\frac{3}{2}\boldsymbol{\sigma}' : \boldsymbol{\sigma}'\right)^{1/2} - \sigma_y \tag{4.6}$$

When $f_y < 0$: Elastic deformation

$f_y = 0$: Plastic deformation

Where σ_e denotes the equivalent stress; σ_y is the yielding stress. σ' is deviatoric part of Cauchy stress tensor given by

$$\boldsymbol{\sigma}' = \boldsymbol{\sigma} - \frac{1}{3}\mathrm{Tr}(\boldsymbol{\sigma})\mathbf{I} \tag{4.7}$$

In the case of plane stress, as shown in Figure 4-2, the part into the elliptic domain remains elastic, where a point on the elliptic domain starts to yield. Under continuing deformation, most metal undertake work-hardening when deforming plastically. Figure 4-2 represents the expansion of the yielding surface and the corresponding stress-strain curve under isotropic hardening conditions. The original yielding surface expands uniformly outwards.

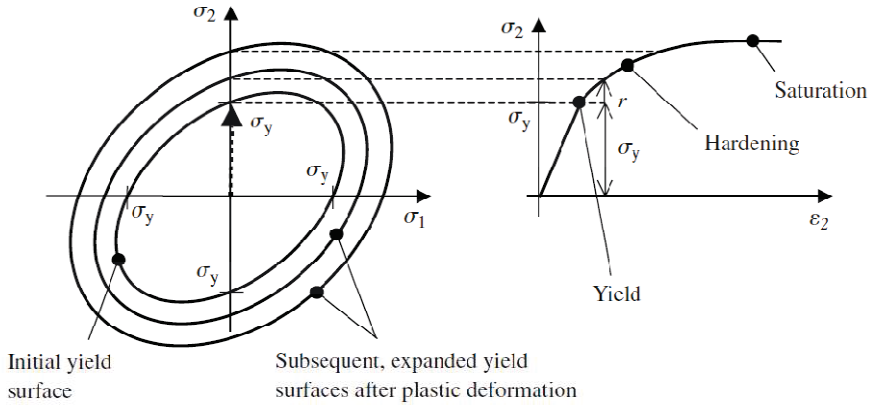

Figure 4-2. *Isotropic hardening, in which the yield surface expands with plastic deformation, and corresponding uniaxial stress-strain curve [65].*

For a tensile test, the relationship between stress and plastic strain can be expressed by the Swift's equation [67]:

$$\sigma = \sigma_y = \mathrm{K}\left(\varepsilon_0 + \bar{\varepsilon}_p\right)^n \tag{4.8}$$

where σ and $\bar{\varepsilon}_p$ represent the equivalent stress and the equivalent plastic strain respectively. ε_0, K and n are material parameters. Figure 4-3 shows the comparison between measurements and the fitting curve obtained from equation 4.8, in which the parameter K is *1051.7 MPa*, the hardening exponent n is *0.16* and σ_y is *378 MPa*. The so-fitted material parameters will be used as input data for base metal in the FE software Abaqus.

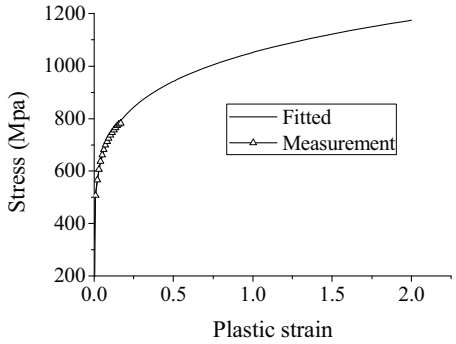

Figure 4-3. *Test data and fitted curve of DP600 steel*

For polycrystalline metals, it has been observed that ductile fracture is controlled by nucleation, growth and coalescence of microvoids [68]. Gurson [69] introduced a micro-mechanical damage model for describing ductile fracture by means of void volume fraction as an additional internal variable. The initially proposed yielding function was modified to introduce the variable f^* by Tvergaard and Needleman [70]

$$\Phi = \left(\frac{\sigma_e}{\sigma_y}\right)^2 + 2q_1 f^* \cosh\left(-q_2 \frac{3p}{2\sigma_y}\right) - \left(1 + q_3 f^{*2}\right) = 0 \tag{4.9}$$

Where σ_e is the macroscopic equivalent von Mises stress and σ_y is the yield stress of the matrix material surrounding the voids. p is the hydrostatic stress. q_1, q_2 and q_3 are constants introduced by Tvergaard [71]. Here, we take the original $q_1 = 1.5$, $q_2 = 1$ and $q_3 = q_1^2 = 2.25$ by Tvergaard. f^* is a bilinear function of the void volume fraction f, such as:

$$f^*(f) = \begin{cases} f, & for \quad f \le f_c \\ f_c + \dfrac{f_u^* - f_c}{f_f - f_c}(f - f_c), & for \quad f > f_c \end{cases} \tag{4.10}$$

Where, $f_u^* = 1/q_1$. f_c is the critical value of voids coalescence. The value of f_c is a material constant that can be determined experimentally or numerically [72]. f_f is the void volume fraction at final fracture. Zhang [68] pointed out that f_f is strongly dependent on the initial void volume fraction f_0 and that it is also influenced by stress triaxiality. When the void volume fraction reaches f_c, void coalescence starts and the void volume fraction rapidly increases, whereas the material load carrying capacity decreases progressively. When the void volume fraction reaches the final value f_f, the material suddenly loses its load carrying capacity.

The total void volume change can be split into two parts: the growth of existing voids and the nucleation of new voids.

$$\dot{f} = \dot{f}_{growth} + \dot{f}_{nucleation} \tag{4.11}$$

Where the growth of existing voids is driven by the volumetric plastic strain (the plastic flow is compressible),

$$\dot{f}_{growth} = (1-f)\dot{\varepsilon}^{p} : \mathbf{I}. \tag{4.12}$$

where $\dot{\varepsilon}^{p}$ is the plastic strain rate. The nucleation of void is mainly controlled by the matrix equivalent plastic strain rate $\dot{\bar{\varepsilon}}_{m}^{p}$ [72], such that:

$$\dot{f}_{nucleation} = A\dot{\bar{\varepsilon}}_{m}^{P} \tag{4.13}$$

where A is a function, in the form of Gaussian distribution:

$$A = \frac{f_N}{S_N\sqrt{2\pi}} \exp\left\{-\frac{1}{2}\left(\frac{\bar{\varepsilon}_{m}^{P} - \varepsilon_N}{S_N}\right)^2\right\} \tag{4.14}$$

Here, f_N is the volume fraction of particles available for news voids nucleation. ε_N and S_N are the mean voids nucleation burst strain and the standard deviation for the normal distribution respectively.

Gurson model predicts no increase in damage if continuous void nucleation is not invoked. As a consequence, no damage induced softening takes place under shear in materials with inherent strain hardening capacity, and neither localization nor material failure occurs [74-75]. Consequently, the Gurson model shows over prediction of ultimate force for KS2 test with shear loading because the lacks of voids prediction under shear. For this reason, cohesive zone model is used to predict the failure of WM under shear and tension force in spot weld. Indeed, cohesive zone model is successfully used to predict spot weld fracture by Cavalli *et al.* [76-77].

1.2. Cohesive zone model (CZM)

In certain cases, fracture can occur at physical interfaces, such as adhesive or coating between two substrates. In these cases the continuum damage modeling is not recommended because it cannot predict the interface debonding or cracks propagation path under complex loading [78]. Instead, it is common to introduce cohesive zone elements to simulate crack initiation and crack growth in finite element programs. Cohesive zone elements connect substrates made of bulk elements and govern their separation in accordance with a cohesive law [79].

Figure 4-4 shows CZM where cohesive zone elements are placed between continuum bulk elements. Cohesive zone elements start to open in order to simulate crack initiation or crack

growth when forces are applied on the bulk element. The crack propagates along the path formed by cohesive elements.

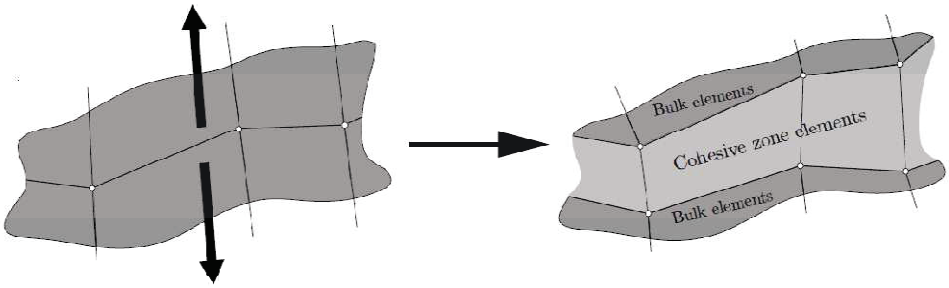

Figure 4-4. *Cohesive zone elements between bulk continuum elements [78]*

There are two kinds of model to describe the cohesive behaviors: continuous approach model and traction-separation laws. The continuum-based modelling is appropriate when the materials between substrate matrixes have a finite thickness. The macroscopic properties, such as stiffness and strength, of the material can be measured experimentally and used directly for modeling purposes.

In the case of very thin material layer, the behavior of the interface prior to initiation of damage is often described as traction-separation laws (TSLs) but is unaffected by pure compression. The advantages of TSLs are a simplified parameters identification process and computational efficiency.

The constitutive behavior of CZM governed TSLs describes the tractions as a function of separations. There is a large variety in traction separation laws [80] but they all exhibit the same global behavior. The separations displacements are denoted by δ_n, δ_s and δ_t. The original thickness of the cohesive element is denoted by T_0. The nominal strains (one normal and two shear components) are defined as:

$$\begin{cases} \varepsilon_n = \delta_n / T_0 \\ \varepsilon_s = \delta_s / T_0 \\ \varepsilon_t = \delta_t / T_0 \end{cases} \tag{4.15}$$

The nominal traction stress vector t consists of three components (two shear components): t_s, t_t, and (one in thickness) t_n, which represent the two shear and the normal tractions respectively. The relationship between traction and separation is described by:

$$\mathbf{t} = \begin{Bmatrix} t_n \\ t_s \\ t_t \end{Bmatrix} = \begin{pmatrix} K_n & 0 & 0 \\ 0 & K_s & 0 \\ 0 & 0 & K_t \end{pmatrix} \begin{pmatrix} \varepsilon_n \\ \varepsilon_s \\ \varepsilon_t \end{pmatrix} = \mathbf{K}\boldsymbol{\varepsilon} \tag{4.16}$$

Where K_n is normal stiffness, K_s and K_t are shear stiffness. ε_n is the separation displacement in the normal direction, ε_s and ε_t are separation strain in shear directions 1 and 2, respectively.

Figure 4-5 shows the linear elastic and linear damage evolution (bilinear) of the traction-separation law under normal mode-I and shear mode-II of fracture. Here, the traction and separation along first and second directions of mode-II are supposed to be isotropic shear behavior, $K_s = K_t$. The response is linear elastic until damage initiation. As the cohesive surfaces separate, the traction stress first increases until a critical value is reached (t_o or t_s), and subsequently decreases to zero. G_{Ic} and G_{IIc} are fracture energies to open the cohesive zone under normal and shear modes respectively. The two parameters can be calculated with the J-integral. The main disadvantage of TSLs is that they do not consider elasto-plastic deformation. Jousset [6] reported that TSLs cannot predict yielding in small scaled specimens with thick metal substrates accurately. However it has capacity to predict the force-displacement curve in large T-joint benchmark made of thin-bonded metal plates, in which the overall response is not sensitive to the plasticity in adhesive layer. TSLs are used in this research in the FE simulation of both KS2 and T-joints, since the final aim is to develop models for large components simulation.

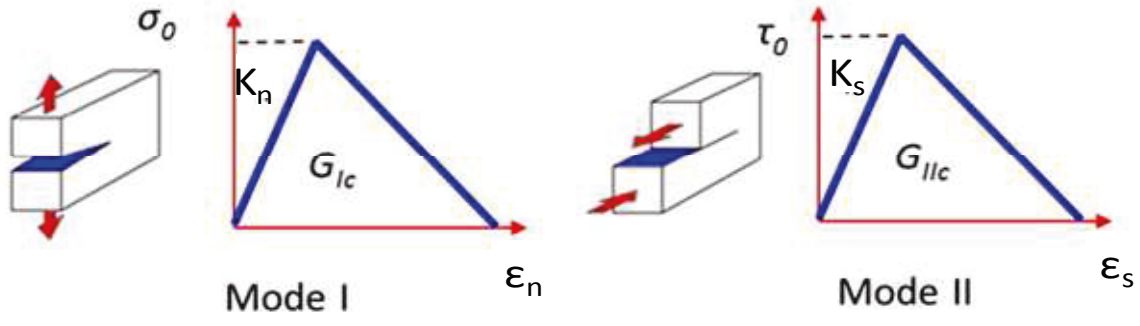

Figure 4-5. *Mode-I and Mode-II traction-separation law[62]*

In this thesis, TSLs is used in a simple linear elastic, stress-based damage initiation and Benzeggagh-Kenane damage evolution, implemented in Abaqus with interface (or cohesive) elements. To use this TSLs model, parameters K_n, K_s, σ_0, G_{Ic}, τ_0 and G_{IIc} have to be identified.

The stiffness K_n *and* K_s are given by

$$K_n = \frac{E}{T_0} \tag{4.17}$$

and

$$K_s = \frac{E}{2(1+\nu)T_0} \tag{4.18}$$

where T_0 is the initial thickness of cohesive elements.

A maximum traction criterion is used for damage initiation such that:

$$\max\left(\frac{<t_n>}{\sigma_0}, \frac{t_s}{\tau_0}\right) = 1 \tag{4.19}$$

where <> is Macauley bracket. σ_0 and τ_0 are critical nominal stress and shear stress respectively. An energy based criterion is used for damage evolution. The Benzeggagh-Kenane fracture criterion [81] is suggested where the critical fracture energies along the first G_s^C and the second shear directions G_t^C are the same in this work, i.e. $G_s^C = G_t^C = G_{IIC}$. The criterion is given by:

$$G_{IC} + (G_{IIC} - G_{IC})\left\{\frac{G_S}{G_T}\right\}^{\xi} = G^C \tag{4.20}$$

where G^C is mixed-mode fracture energy and ξ is Benzeggagh-Kenane mix model parameter.

$$\begin{cases} G_S = G_s + G_t \\ G_T = G_n + G_S \end{cases} \tag{4.21}$$

where G_n, G_s and G_t refer to the work done by the traction and its conjugate relative displacement in the normal, the first, and the second shear directions, respectively.

2. Modeling strategy and results

In this section, the modeling and simulation results for SW joints, AB joints and WB joints will be discussed separately since the 3 kinds of joining methods are investigated for comparison purpose.

2.1. Modeling strategy and results for spot welded joint

2.1.1. FE model for spot weld joint

There are several models of SW joints used for failure analysis under static and dynamic conditions [24][36-37][39]. Modeling spot weld is difficult, because many factors can influence spot weld properties such as geometrical irregularities, residual stresses, material inhomogeneities and defects in spot weld nuggets. These factors are even not taken into account by finite element modeling [80].

Generally, spot weld models can be classified into two types: solid models and simplified models. In the former, detailed geometries and materials inhomogeneities of spot weld are taken into account. Material constitutive parameters of different zones must be calibrated and refined mesh must be used. Solid models can capture the stress distribution and concentration in vicinity of spot welds. Moreover, it can predict interfacial failure and pull-out failure. Seeger *et al.* [35] developed a method to characterize the spot welded joint failure by using a highly detailed simulation model. Sommer [53] successfully predicted the peak loading and fracture modes under different loading combining Gurson model with shear induced fracture model. Dancette [37] *et al.* introduced a finite element model combining cohesive elements and a ductile fracture model for the prediction of interfacial and pull-out fracture. Nielsen and Tvergaard [82] used a modified Gurson model with shear prediction capacity to simulate shear failure or pull-out failure. However, for a large structure which contains thousands of spot welds, e.g. car body in white, solid models are not appropriate as they require too high computational efforts to reach a useful solution [83]. Hence, simplified models are introduced to reduce computational costs, such as connector elements [84], elastic or rigid beams models [85] or brick elements [86].

In this section, both detailed solid models and simplified models are developed to simulate small-scale specimens.

The material in spot weld is heterogeneous. It can be split into three different zones in terms of materials properties: BM, HAZ and WM, as shown in Figure 4-6. WM has a radius of *2.9 mm*

and HAZ a width of *0.8 mm*. HAZ and WM flow stresses are scaled from the flow stress of BM using scaling factors α_1 and α_2:

$$\sigma_{HAZ} = \alpha_1 \sigma_{BM} \tag{4.22}$$

$$\sigma_{WM} = \alpha_2 \sigma_{BM} \tag{4.23}$$

where, σ_{HAZ} and σ_{WM} are flow stresses of HAZ and WM, respectively. Inverse identification is used to calibrate these factors.

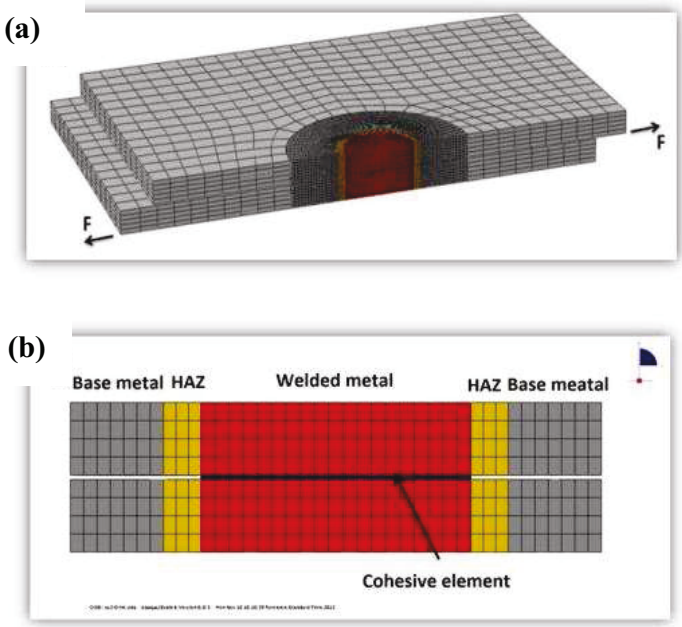

Figure 4-6. *FE model of spot weld: (a) half mesh, (b) meshes in different zones.*

HAZ and WM zones are meshed using very fine meshes as plastic deformations and necking occur in HAZ/BM or HAZ/WM in tests where spot welds collapse, as shown in Figure 4-6 (a). Because of the symmetry, only half of the spot welded KS2 joints is modeled, in order to save computational time. The simulations of spot weld were performed with 8-node, linear brick, reduced integration elements (C3D8R) with COH3D8 cohesive element in faying surface, as shown in Figure 4-6 (b). Cohesive elements are used to predict shear fracture under shear loading since Gurson model cannot predict voids growth in pure shear.

2.1.2. Sensitivity analysis in spot welds simulation

2.1.2.1. Mass scaling

ABAQUS/Explicit provides the capability to analyze large deformation and fracture, in nonlinear, quasi-static analyses. It often provides a faster solution and robust modeling capabilities for highly nonlinear problems. In explicit analysis the hope is that if the increments are small enough the results will be accurate. One problem with this method is that you do need many small increments for stability and it is time consuming. If the numbers of increments are not sufficient the solution tends to drift from the correct solution. The stable time increment is estimated by the equation [87]:

$$\Delta t \leq \min\left(L_c / C_d\right) \tag{4.24}$$

where L_c is a characteristic length associated with an element over all elements in the mesh and C_d is the dilatational wave speed given by:

$$C_d = \sqrt{\frac{\lambda + 2\mu}{\rho}} \tag{4.25}$$

where ρ is the density of the material in the element. For non elastic behaviour effective hypoelastic model should be used.

Mass scaling is very useful to improve the computational efficiency in explicit quasi-static simulation while ensuring the necessary degree of accuracy for a particular problem class. In this thesis, variable mass scaling is used to increase the stable time step to a target value.

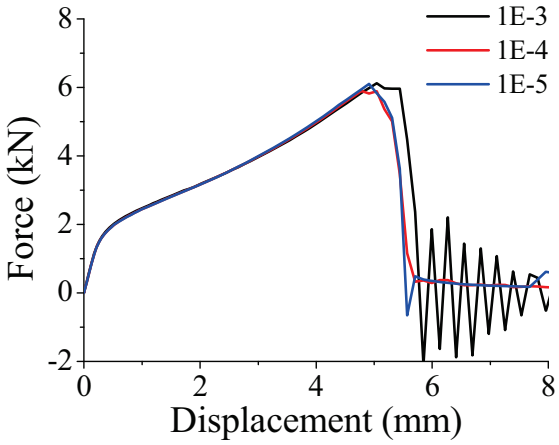

Figure 4-7. *Analysis of KS2 specimen with different time step increment*

Variable mass scaling are investigated on the whole models of KS2 tension. Three kinds of mass scaling are performed with different stable time step target values, *1.0E-3s*, *1.0E-4s* and *1.0E-5s*, respectively. Figure 4-7 shows that the response does not exhibit significant change prior to fracture. The ultimate strength for Δt*=1.0E-3s* is slightly higher than the others. It can be concluded that even a high mass scaling value has only a slight effect on the response of our simulation under quasi-static loading. Hence, the mass scaling producing a stable time step value of *1.0E-3s* is chosen for this research.

2.1.2.2. Mesh size

It was discussed that fine mesh in the vicinity of nugget is essential. However, too fine meshes will decrease the stable time step size and increase the computational time. The mesh sizes and simulation accuracy are investigated in spot weld firstly. In Figure 4-8, different mesh sizes are used in the HAZ and WM from *0.2 mm* to *1.0 mm*, while 1mm coarse meshes are used in base metal. The simulation is carried out on lap-shear test without considering damage.

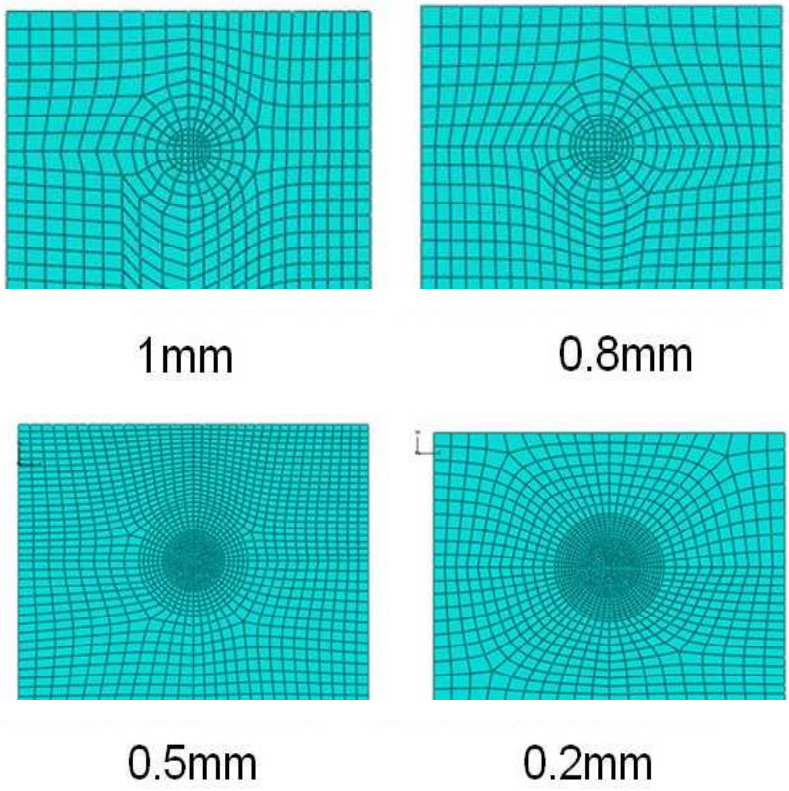

Figure 4-8. *Different mesh sizes in spot weld in a lap-shear specimen*

Figure 4-9 shows the predicted force-displacement curves corresponding to different mesh sizes. When the mesh size is refined up to *0.2 mm*, the response does not show significant change. Therefore, a *0.5 mm* mesh size is used in nuggets for spot weld simulations.

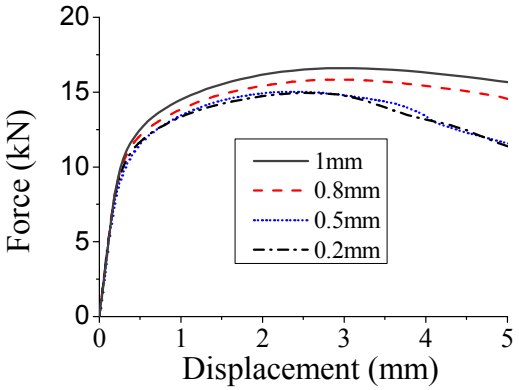

Figure 4-9. *Force-displacement curves obtained with different element sizes*

2.1.2.3. Nugget diameter

The nugget's diameter is considered as the key factor affecting spot weld strength. Interfacial fracture will occur when the diameter is under a critical value. The sensitivity to the nugget diameter is carried out without damage. The results show that the strength of SW increases with the increasing of WM diameters, as shown in Figure 4-10. However, the nuggets of spot weld always scatter in a certain range under fixed welding parameters. In this work, we take an average diameter of 5 tests for each experiment.

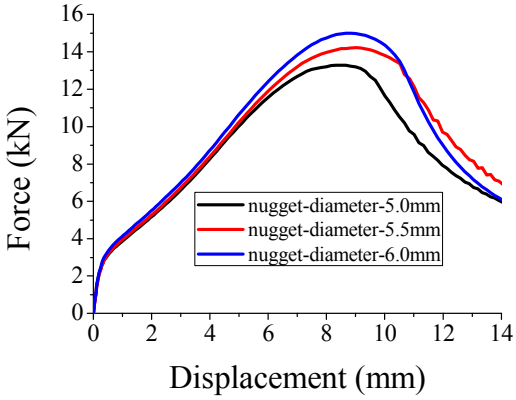

Figure 4-10. *Force-displacement curves obtained with different nugget's diameters*

2.1.2.4. Flow stress of HAZ and WM

In this section, the sensitivity of flow stress of HAZ and WM to the simulation result is investigated by the scaling of flow stress of BM. A set of scaling factors is defined artificially: α_1=*1.5* and α_2= *1.8*. Figure 4-11 shows the force-displacement curve of different joints without considering damage. The maximum strength increases by *23.1%* for cross-tension, *18.7%* for lap-shear and *29.7%* for peel loading after scaling of flow stress. It indicates that scaling of flow stress of HAZ and WM has a significant effect on the force-displacement response of spot weld.

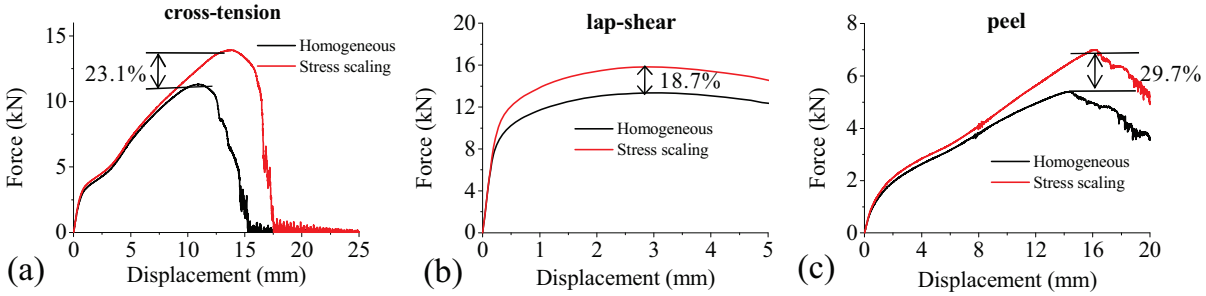

Figure 4-11. *Comparisons between predictions from homogeneous and heterogeneous spot weld models*

2.1.3. Inverse identification

Since materials properties of HAZ and WM have significant effect to the response of spot weld, inverse identification method is used to find the adequate scaling factor of WM and HAZ. This method can avoid the conventional mechanical testing, i.e. miniature bar tests [53] or simulated heat affected specimens [88]. This process consists in finding a set of material parameters in such a way that the simulated response calculated by the constitutive model matches the corresponding experimentally measured response. The difference between computed and measured responses is represented by a least square function of the form:

$$f(x)=\sum_{i=1}^{n}\left[m_i(x)-c_i(x)\right]^2 \tag{4.26}$$

Where $m_i(x)$ and $c_i(x)$ are the measured and the computed response corresponding to the same displacement. The optimization problem is to identify a set of materials parameters x minimizing *f(x)* via using local methods such as gradient algorithms or global methods such as genetic algorithms.

A fully automated procedure has been developed in the frame of this thesis by associating Abaqus with the optimization code Altaire Hyper Study through a Python script. The FEM simulation starts based on a set of initial parameters defined by the user. In this study, all the initiate parameters are set at 1, i.e. homogeneous in all sections of spot weld. The comparison of response between simulation and measurement is limited in the range of elastoplasticity. If *f(x)* matches the minimization of objective function, these parameters are outputted as the optimal parameters. If not, a set of new parameters will be calculated and a new simulation will be run. This process will be repeated until optimal parameters are obtained, as shown in Figure 4-12.

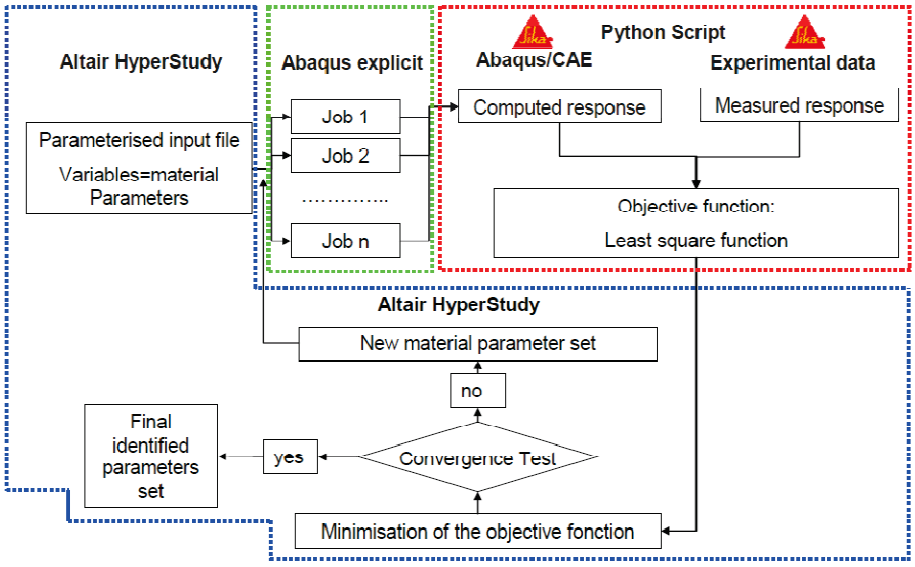

Figure 4-12. *Flow chart of the inverse identification procedures*

The identification processes are carried out on KS2 shear, KS2 tension and peeling to search the unique set of scaling factors which could match all the loading cases. The optimized scaling factors are: $\alpha_1 = 1.7$ to HAZ and $\alpha_2 = 1.9$ to WM. The measured, initial and optimized response of different loading cases from unique set of parameters is depicted in Figure 4-13. The start, target and optimized result are represented by red dot line, black solid line and blue dash line, respectively. Figure 4-13 (a) show that simulation from optimized parameters and the target response are well matched. As regard tension and peeling loading, the difference of response between simulation and measurement are larger than that of shear loading, as shown in Figure 4-13 (b).

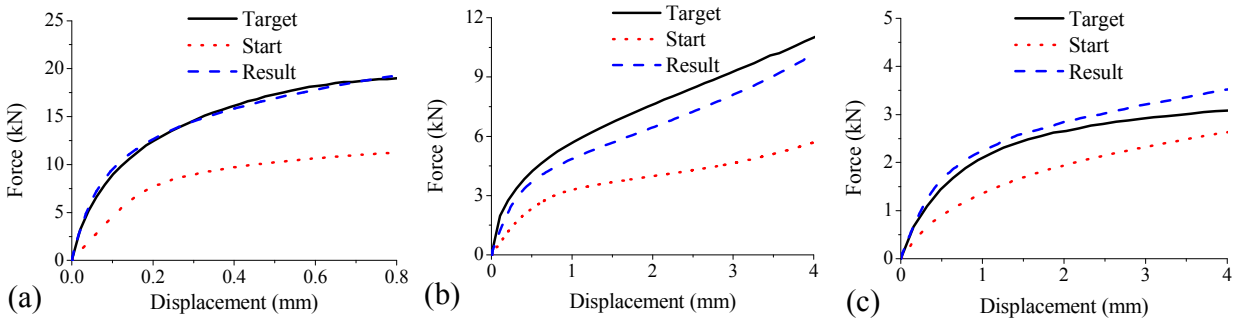

Figure 4-13. *The measured, initial and optimized response of different loading cases: (a) KS2 shear, (b) KS2 tension and (c) peel*

The flow stress of WM and HAZ are computed by Equation 4-22 and 4-23 using the optimized scaling factor. Figure 4-14 shows the flow stress of WM and HAZ and fitted flow stress of BM. These flow stresses are used in the simulation as materials input data.

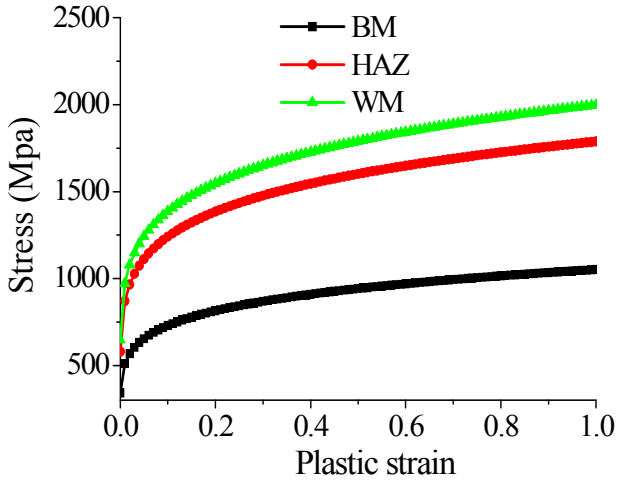

Figure 4-14. *Flow stress of BM, HAZ and WM zone*

2.1.4. Material parameters calibration

2.1.4.1. Parameters of the Gurson model

Gurson model is widely used by many authors to predict ductile metal fracture [53][75][82][89]. There are 8 parameters to be calibrated for a given materials. In this work, the spot weld can be divided into 3 different zones; each zone has a set of parameters. Hence, there are totally 24 parameters that need to be calibrated. q_1, q_2 and q_3 are constants introduced by

Tvergaard [71]. Here, we take $q_1 = 1.5$, $q_2 = 1$ and $q_3 = q_1^2 = 2.25$. The mean voids nucleation burst strain ε_N and the standard deviation S_N for DP600 can be found in [36].

The volume fraction of particles available for new voids nucleation, f_N, is related to the pre-existed voids or defects in materials. DP steels contain small fractions of hard martensite particle in soft ferrite matrix. The weak grain boundary between martensite and ferrite could be the sources of voids nucleation. In DP600, the martensite fraction ranges from *2%* to *10%*. In HAZ and WM, martensite fraction increases due to the heat affection of spot weld process. Hence, f_N is set at 0.02 for base metal and 0.1 for WM. The volume fraction of particles f_N of HAZ is considered close to that of WM, f_N is 0.08 at this work.

f_C is a material constant that can be determined experimentally. f_F is the void volume fraction at final fracture. These two parameters can be calibrated by the so-called "trial-error" process which needs to run the simulation several times till the predicted result agrees with the measurement. The parameters of Gurson model for spot weld simulation are summarized in Table 4-1.

Table 4-1. *Parameters of Gurson model for simulation*

	Material Constant	**Porous Nucleation and Distribution**			**Porous Coalescence**	
BM	q_1=1.5 q_2=1.0 $q_3=q_1^2$=2.25	f_N=0.02	ε_N=0.35	S_N=0.5	f_C=0.056	f_F=0.10
HAZ		f_N=0.08	ε_N=0.25	S_N=0.5	f_C=0.03	f_F=0.06
WM		f_N=0.1	ε_N=0.2	S_N=0.5	f_C=0.03	f_F=0.08

2.1.4.2. Calibration of traction separation model for spot weld

Cavalli *et al.* introduced the cohesive zone model to predict the interfacial and pull-out fracture of spot weld in aluminum alloy [90]. Then, Zhou *et al.* used the same model to simulate ultrasonic spot weld on same metal [91]. These two authors calibrated cohesive parameters with the help of experiments under different loading modes. Dancette *et al.* predicted interfacial fracture of spot weld using cohesive element on the faying surface [88]. For casting aluminum, spot weld keep the same materials properties, and parameters can be calibrated on base metal. For DP steel, fracture mechanics is employed to calculate the energies to create the new damage surface. *J-integral*, proposed by James Rice in 1968, is used to calculate energy release rate in fracture surface by means of path contour integral around the crack [92]. Rice also showed that if

monotonic loading is assumed then the J-integral could be used to compute the energy release rate of plastic materials. The *J-integral* calculation is implemented in Abaqus. Figure 4-15 shows the model used to calculate *J-integral*. Here, we suppose that the crack tip is embedded into WM guarantying isotropic material surrounding the tip. Very fine meshes are required around the crack-tip.

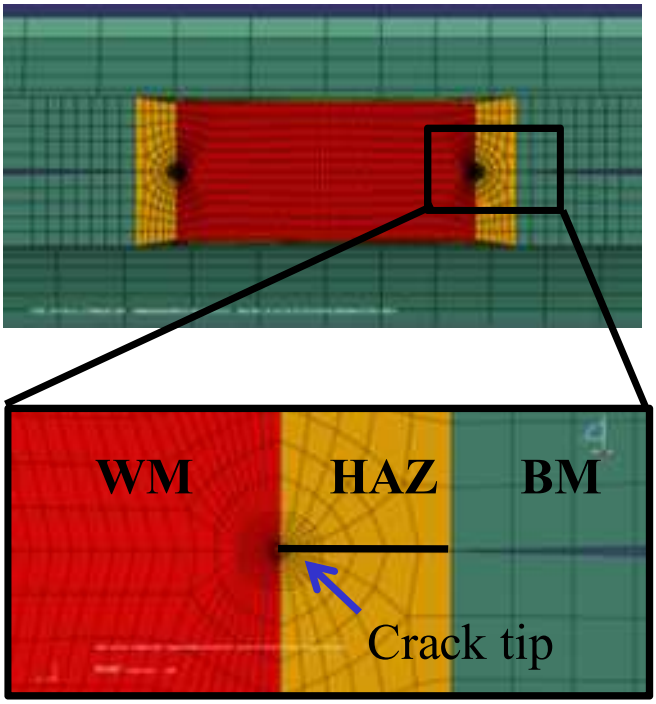

Figure 4-15. *FEM model for the computation of J-integral*

The simulation is carried out under shear and tension loading, as shown in Figure 4-16. For each loading condition, 5 contours of *J-integral* are outputted. The one close to crack tip is neglected due to plastic deformation. The average value of the rest is used to calibrate energy release rate for cohesive zone model.

In Figure 4-16, the vertical black dash lines represent the maximum load from experiment; the corresponding *J-integral* at notch tip is read following the corresponding horizontal dash line.

The cohesive zone model parameters for interfacial damage of spot welds are summarized in Table 4-2. The parameters were used for all the spot welds and also weld bonding in the following simulations.

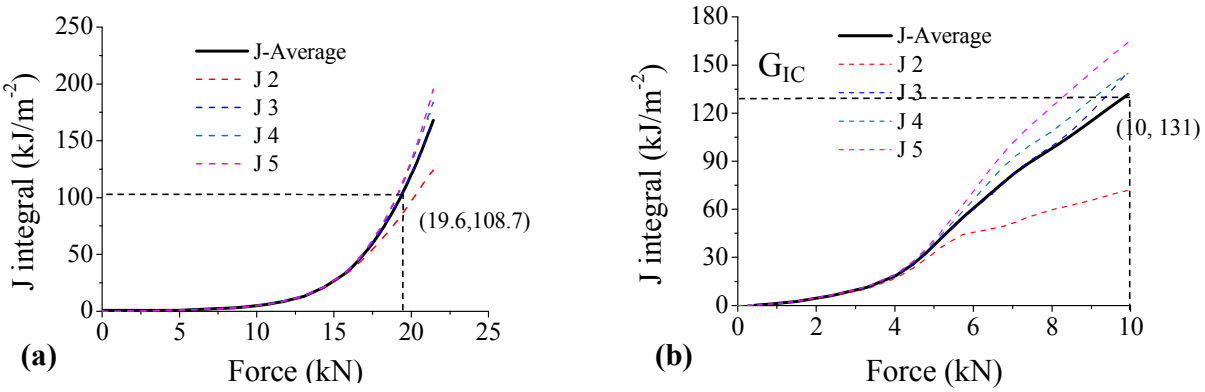

***Figure 4-16**. J-integral under (a) shear loading and (b) tension loading*

***Table 4-2.** Cohesive parameters for interfacial fracture prediction of spot weld*

Stiffness		**Mode I**		**Mode II**	
$K_I\ (N/mm^3)$	$K_{II}\ (N/mm^3)$	$\sigma_0\ (MPa)$	$G_{Ic}\ (mJ/mm^2)$	$\tau_0\ (MPa)$	$G_{IIc}\ (mJ/mm^2)$
2100000	*807690*	*1250*	*131*	*930*	*108.7*

2.1.5. FE Predictions from spot welded joint models

Figure 4-17 shows the simulation boundary conditions used for spot welded joints: (a) KS2 shear, (b) KS2 tension, (c) peeling and (d) lap-shear. Because of symmetry, only half of specimen is discritized in all the simulations. In addition, the griped parts of specimens are not modeled as they do not experience noticeable deformation. The clamping effect is modeled using kinematic coupling constraints. The general contact is trigged with *0.1* friction coefficient between the two sheets. Displacement boundary condition is applied on the loading point to match the loading velocity at 10 mm/min. Smooth step amplitude is used to avoid discontinuities. Local displacement is outputted between point 1 and point 2 depicted in Figure 4-17.

Figure 4-18 shows comparison between the predicted and the measured load-displacement responses. For shear test, the ultimate strength as well as the displacement at fracture is accurately predicted. For tension test, the simulation result gives good prediction of maximum strength. It should be noted that predicted crack is only located on one of spot welded sheets.

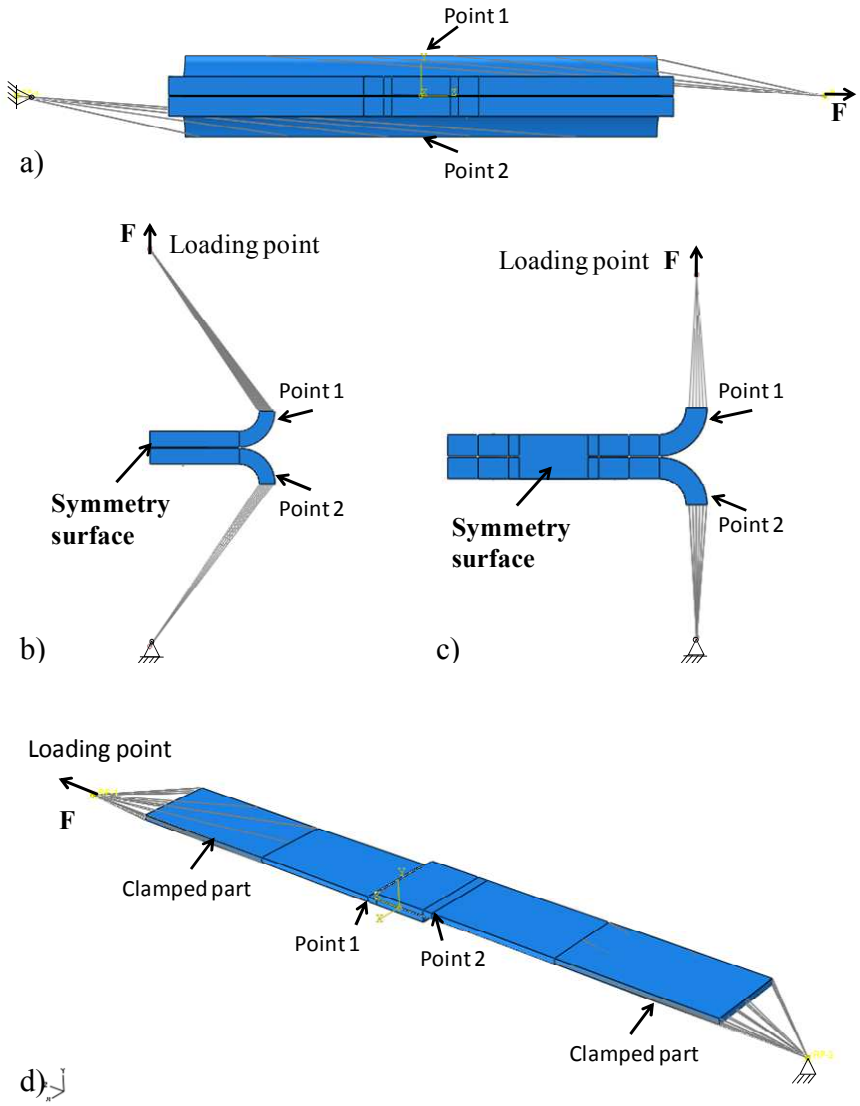

Figure 4-17*. Boundary condition used for SW analysis: (a) KS2 shear, (b) KS2 tension, (c) peeling and (d) lap-shear.*

For the peeling test, the ultimate strength is over estimated when using a *5.8 mm* nugget's diameter as shown in Figure 4-18 (c). A subsequent investigation revealed that the peeling specimens have smaller nugget's diameter than the other specimens in the experiments. Hence, the simulations with *5.4 mm* nugget's diameter were carried out. Figure 4-18 (c) shows that using *5.4 mm* nugget's diameter improves the results accuracy.

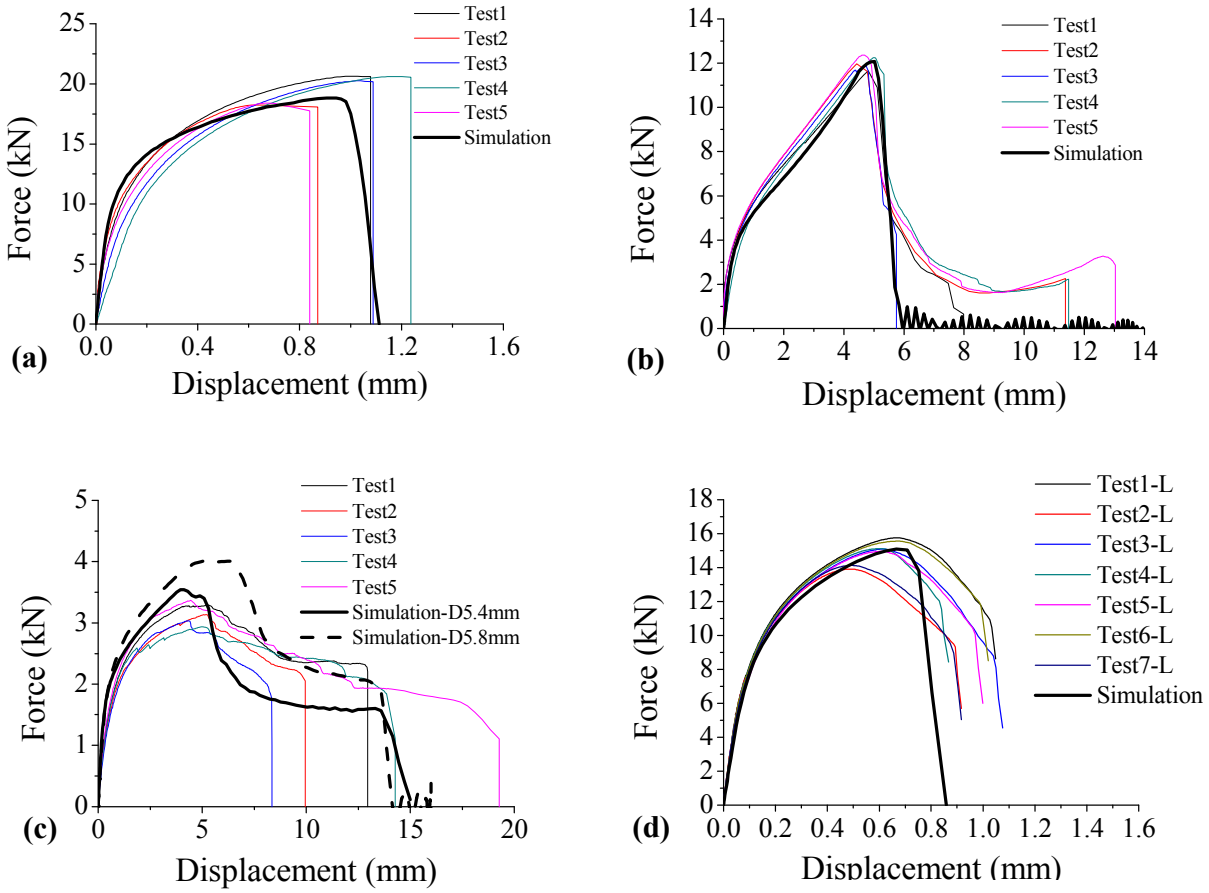

Figure 4-18. *Prediction* vs. *measurement of load-displacement curve of SW joint: (a) shear, (b) tension, (c) peeling and (d) lap-shear*

As illustrated in Figure 4-19, strain localization leads to necking in BM while shear band located in faying surface. These two fracture mechanisms can occur simultaneously in one test. Necking leads to pull-out fracture whereas shear causes interfacial fracture.

Spot weld rotates under bending moment resulting in an opening component in crack tip. Therefore lap-shear sustains tension-shear rather than pure shear in KS2 shear. In KS2 shear, spot weld exhibits limited rotation in simulation. Simulation results show that cohesive element damage in WM prior to the ductile fracture in BM; this leads to interfacial fracture in the spot weld.

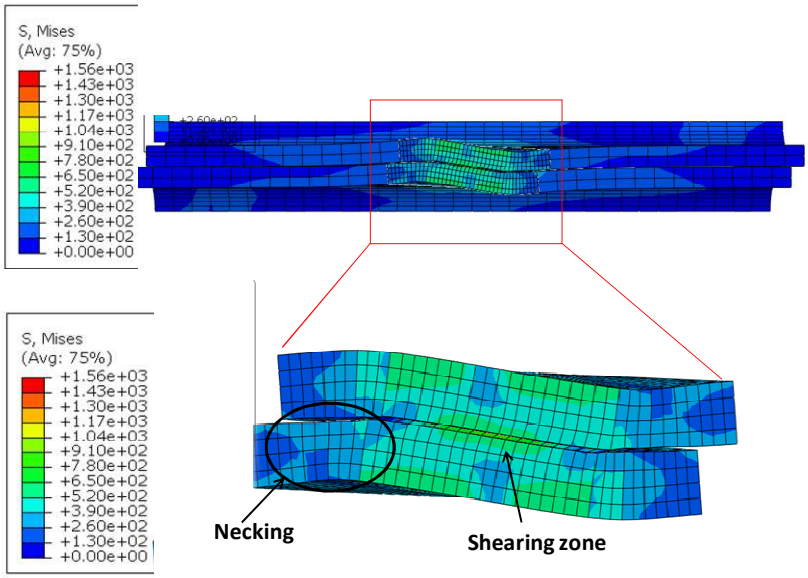

***Figure 4-19**. Stress and deformation of spot weld under shear loading*

Under tension loading, the main cracks tend to open the nugget under mode-I fracture, corresponding to K_I direction in Figure 4-20, while the circumference (HAZ/WM) of spot welds could damaged by kinked cracks. The kinked cracks propagate along the border of HAZ/WM or HAZ/BM.

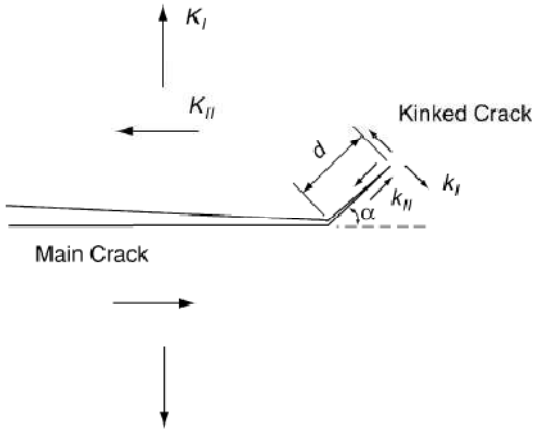

***Figure 4-20.** Main crack and kinked crack under tension loading of spot weld [93]*

Figure 4-21 shows that the crack initiates at the crack tip and propagates to the external surfaces. The elements in HAZ reached the critical value f_F of Gurson model and were deleted.

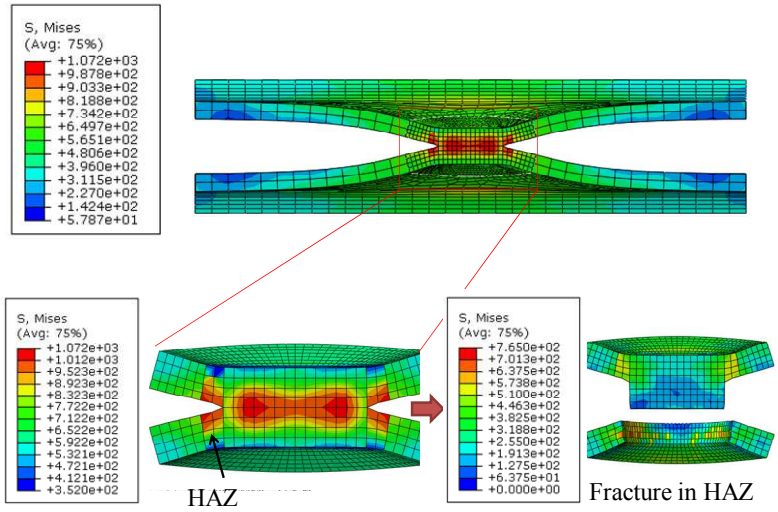

Figure 4-21. *HAZ fracture under tension loading*

In peeling test simulation, the cracks initiate in HAZ, as shown in Figure 4-22 (a). The element near loading path reach the threshold value of damage firstly, then, the cracks propagate in the periphery of WM until further loading pull the nugget out from BM, as shown in Figure 4-22 (b) and (c). It should be noted that the model cannot predict the "tear-out" mode fracture illustrated by Figure 3-15 (c) of Chapter 3.

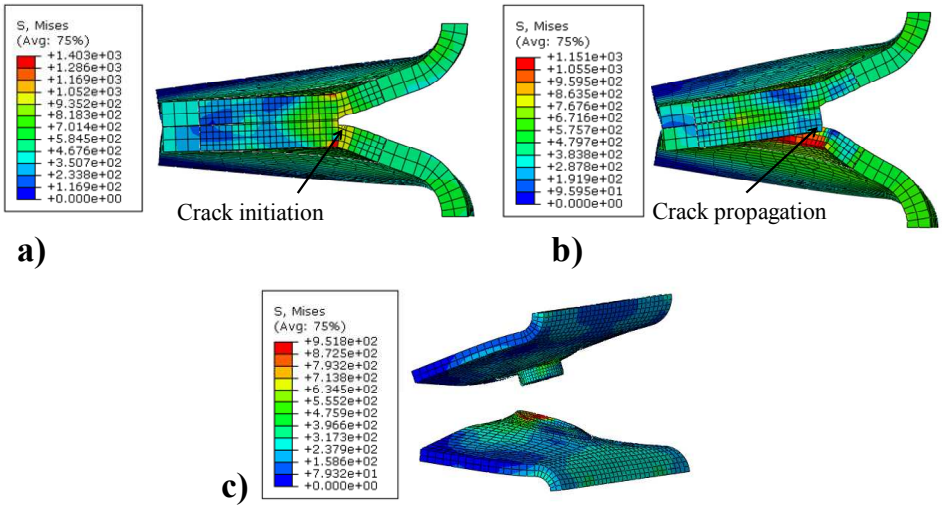

Figure 4-22. *Stress contour of peeling: a) cracks initiation in HAZ, b) cracks propagation, c) pull-out damage.*

The stress state of lap-shear is similar to KS2 shear at the beginning of loading. The model can predict necking in WM and shearing in faying surface, as shown in Figure 4-23. Simulation results show interfacial fracture in lap-shear.

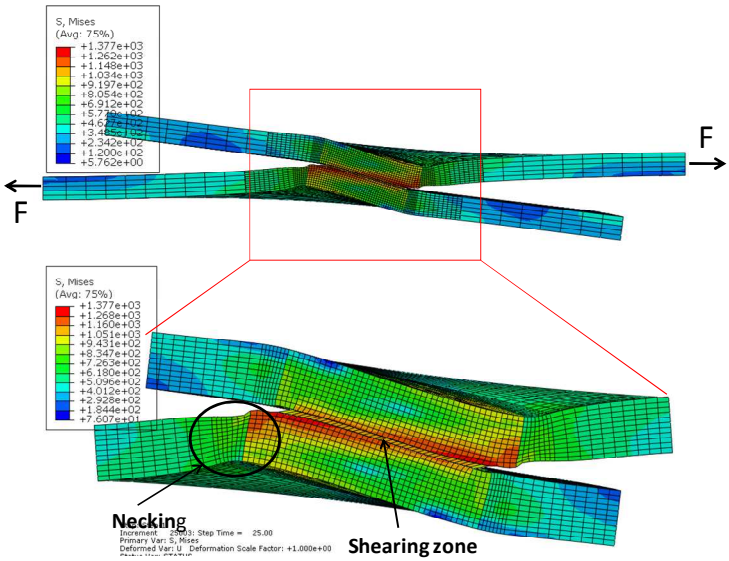

Figure 4-23. *Stress contour before fracture in lap-shear.*

Lap-shear exhibits a larger rotation angle (*17.7°*) than that of KS2 shear loading (*10.4°*), as shown in Figure 4-24. The amplitude of tension component increases when increasing spot weld rotation.

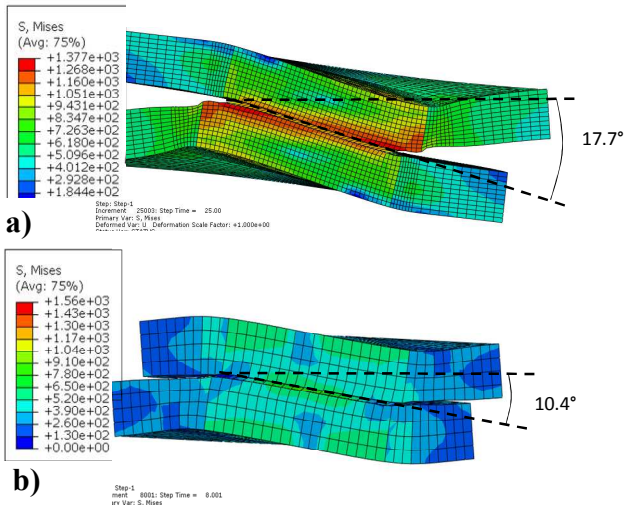

Figure 4-24. *Comparison of rotation angle between (a) lap-shear and (b) KS2 shear*

2.2. Modeling strategy and results for adhesive bonded joint

2.2.1. FE models for adhesive bonded joints

The BM has the same geometry as in the case of spot welded joints, only a half of the model is meshed due to symmetry reasons. The simulations were performed with 8-node, linear brick, reduced integration elements (C3D8R) in BM and cohesive element (COH3D8) in adhesive, as shown in Figure 4-25. Adhesive is modeled as a single layer with interface elements. The nodes in faying surfaces between adhesive and BM are tied together. The simulation boundary conditions are the same as with that of SW illustrated in Figure 4-17.

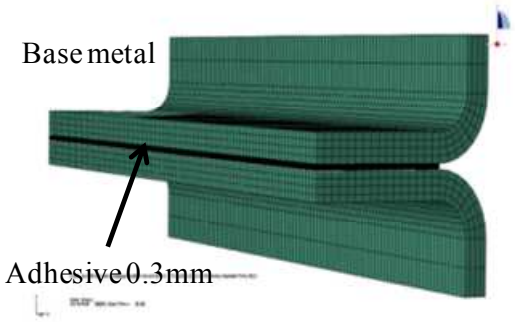

Figure 4-25. *FE mesh of adhesive bonded joint*

2.2.2. Calibration of traction-separation model for adhesive

Traction-separation laws (TSLs) are used to represent cohesive debonding in this research. Biel *et al.* [94] [95] use *double cantilevered beam* (DCB) and *end notched flexure* (ENF) to calibrate the parameters, corresponding to tension and shear load, as shown in Figure 4-26 (a) and (b). The energy release rate can be calculated using the J-integral [96].

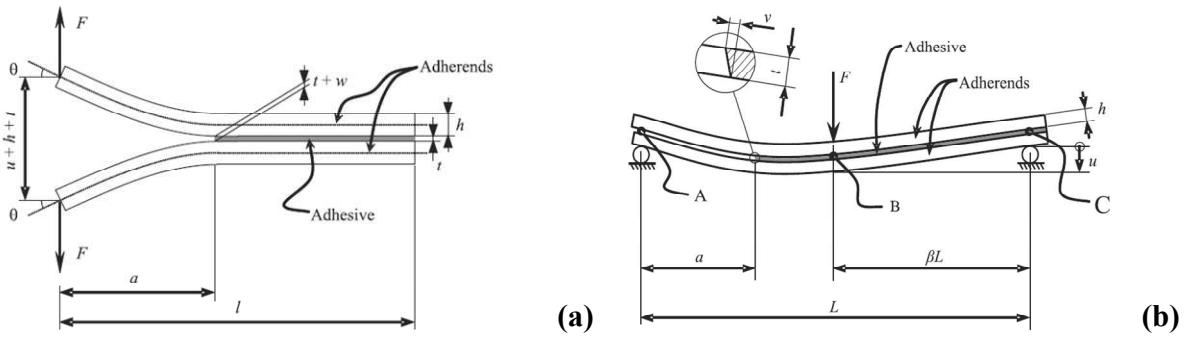

Figure 4-26.*Schematic description of (a) DCB specimen and (b) ENF specimen*

The material parameters are identified by DCB and ENF specimens by Sika Techonology for the adhesive SikaPower®-498. All parameters are summarized in Table 4-3.

Table 4-3. *Cohesive parameters for fracture prediction of adhesive*

Stiffness		**Mode I**		**Mode II**	
$K_I\ (N/mm^3)$	$K_{II}\ (N/mm^3)$	$\sigma_0\ (MPa)$	$G_{Ic}\ (mJ/mm^2)$	$\tau_0\ (MPa)$	$G_{IIc}\ (mJ/mm^2)$
7070	*2600*	*46*	*3.15*	*36*	*12.9*

2.2.3. FE predictions from adhesive bonded joints

Figure 4-28 shows the comparison between prediction and measurement of different joints loaded under different loading-paths.

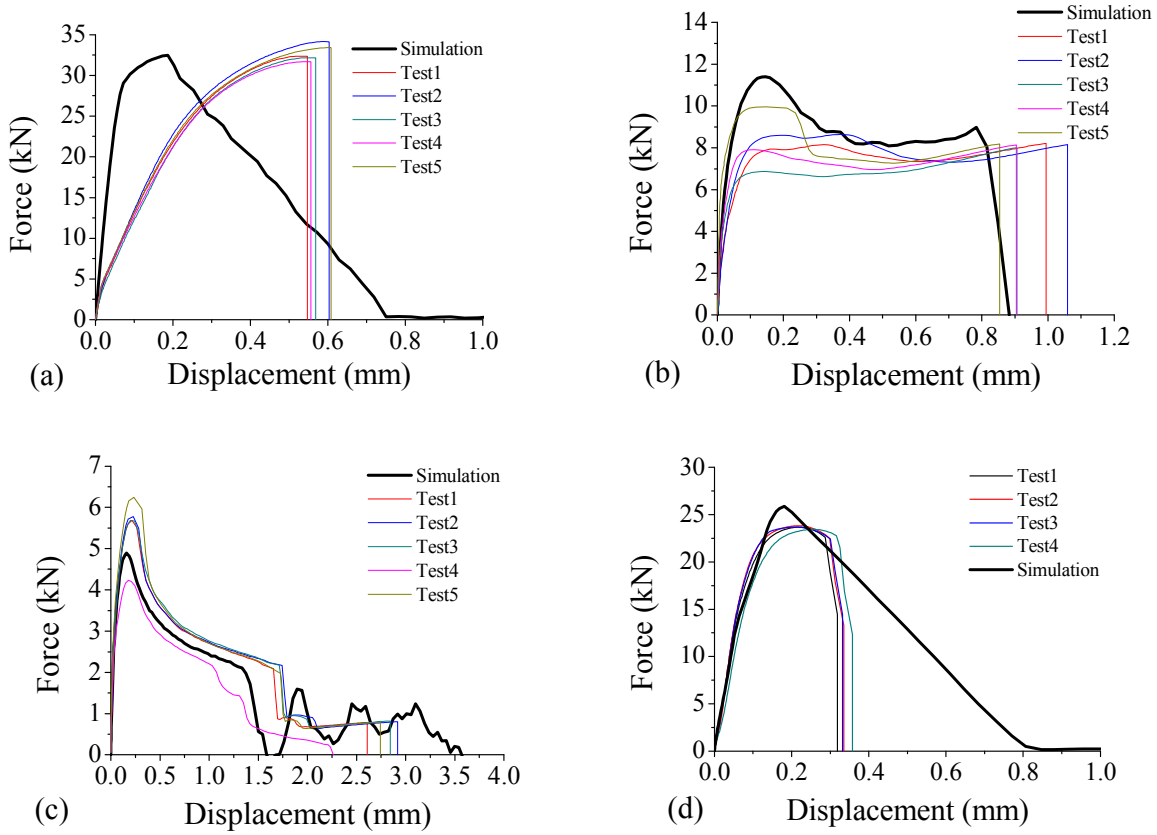

Figure 4-28. *Simulation vs. measurement on load-displacement curve of adhesive bonded joint: (a) shear, (b) tension, (c) peeling and (d) lap-shear.*

TSLs can predict the ultimate strength under shear, but the predicted stiffness is far from the measured one. The difference is supposed to come from the error made when measuring local displacements during the test, which is difficult to measure. One reason is that the load direction could not align with the center of specimen. It should be noted that the whole displacement is 0.6 mm; any small rotation of specimens or sliding between specimen and grips can cause significant alteration in local displacement. In order to prove this assumption, simulations using Mahnken-Schilimmer model [6] and J2 elastoplastic models are carried out, as shown in Figure 4-29. The different models predict the same stiffness in shear.

Under tension and peel, the ultimate strength and the displacement at fracture are accurately predicted.

TSLs cannot predict displacement of catastrophic fracture under shear and lap-shear as it inherently has bilinear shape, as shown in Figure 4-5.

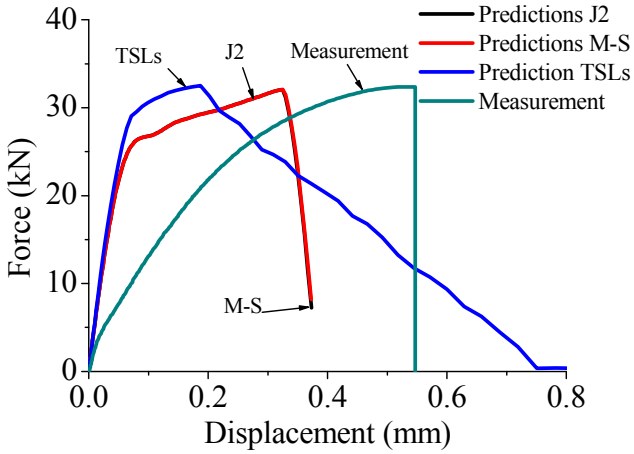

Figure 4-29. *Prediction from different constitutive models for KS2 shear loading*

Adhesive exhibits different failure modes under multi axial loadings. Figure 4-30 shows the scalar stiffness degradation of cohesive elements under different loadings. In KS2 shear, Figure 4-30 (a) shows that AB joint has a uniform stress distribution in the center where a maximum of elements were damaged simultaneously. Contrarily, under tension and peeling damage propagates progressively from external edges to the center as shown in Figure 4-30 (b) and (c). This can also explain the occurrence of different strain rate in the adhesive layer in tension test. Consequently, adhesive shows good ability to withstand shear loading.

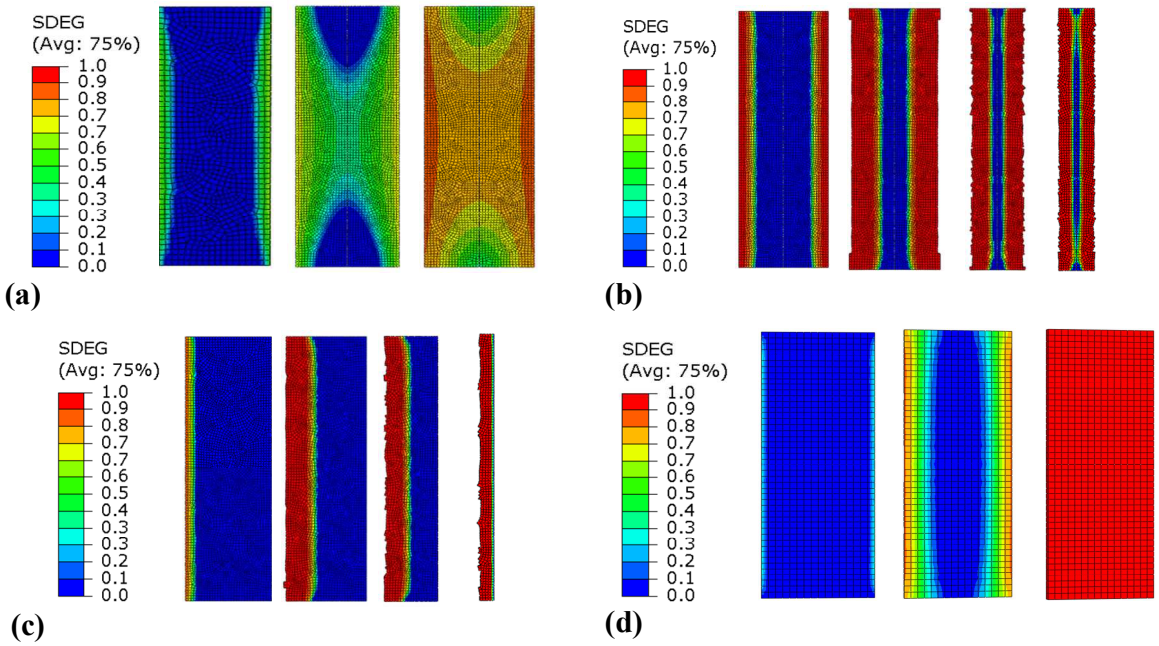

Figure 4-30. *Adhesive failure process under (a) shear, (b) tension, (c) peeling and (d)lap-shear*

Lap-shear has less uniformities of stress than pure shear due to the rotation of faying surface. The components of tension force increase with the increasing of in faying surface rotation.

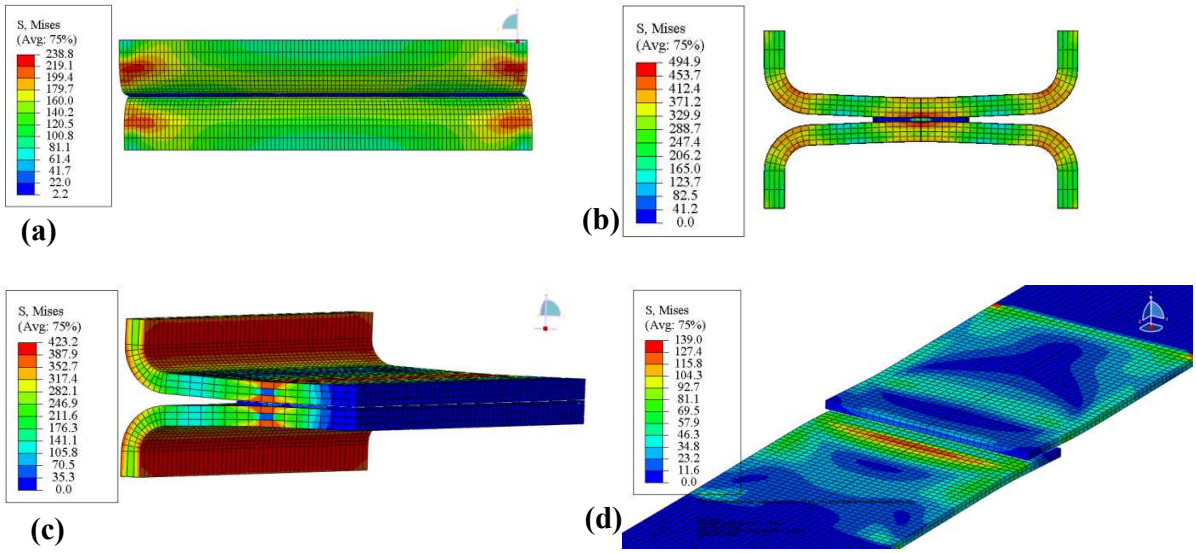

Figure 4-31. *Mises Stress prediction of (a) shear, (b) tension, (c) peel and (d) lap-shear loading*

Figure 4-31 shows predicted Mises stress and deformed BM under different loadings. Maximum stress is observed in BM in the vicinity of the crack fronts in all the simulations, as

shown in Figure 4-31. It is common that the fracture occurs in substrate when adhesive is applied on large area or when low strength steels joints are tested [6].

2.3. Modeling strategy and results for hybrid joint

2.3.1. FE model for hybrid joint

In this section, a model combining a spot weld model with an adhesive model is used to simulate weld bonded joints. Figure 4-32 shows the mesh of the weld bonded joint. The adhesive is meshed with *0.3 mm* single layer cohesive element using TSLs (in black). A *2 mm* gap between adhesive layer and spot weld is created as the adhesive is burnt in this zone. BM is meshed with *1 mm* coarse mesh while HAZ and WM are meshed with *0.4 mm* fine elements with Gurson model. Cohesive elements are associated with TSLs used to predict shear failure of spot welds. The thicknesses of cohesive elements are *0.1 mm*.

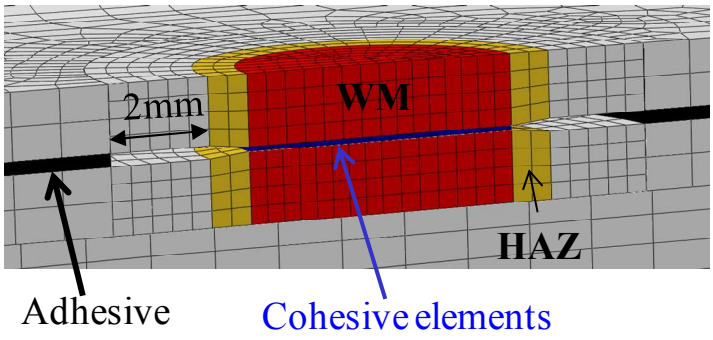

Figure 4-32. *FE model of weld bonded joint*

2.3.2. Predictions from hybrid joint model

The previously described finite element model is used to investigate shearing, tension, peeling and lap-shear tests. The comparisons between the predictions from the model and the measurement are presented in Figure 4-33.

As regards the AB joints, as shown in Figure 4-28 (a), the predicted elastic slope is not in accordance with measurement whereas it was matched in lap-shear, as shown in Figure 4-33 (d). The load carriage capacity is overestimated due to the poor capacity of plastic prediction of TSLs under shear and lap-shear.

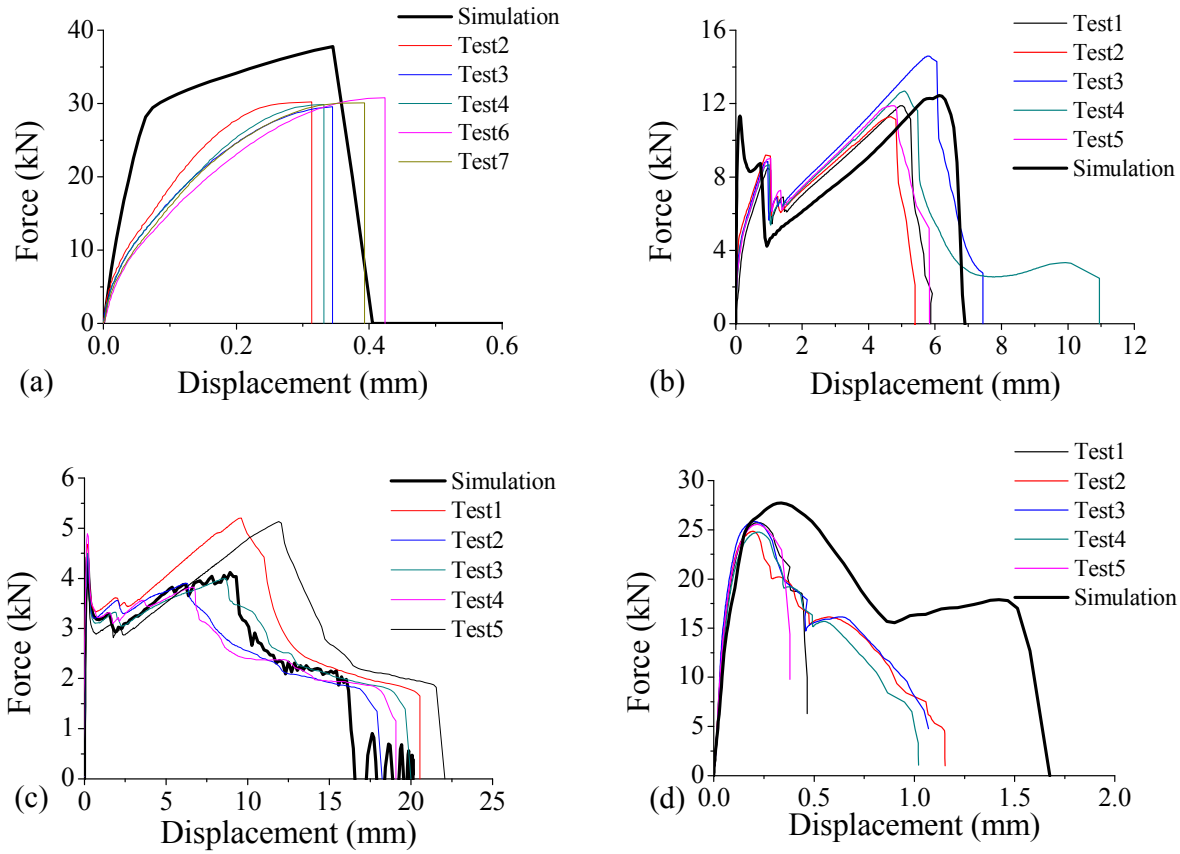

Figure 4-33. *Predictions vs. measurements of load-displacement curves of weld bonded joints: (a) shear, (b) tension, (c) peeling and (d) lap-shear.*

Spot weld failure peak was not observed in shear loading. It indicates that spot weld was damaged prior to adhesive. This phenomenon can be explained by simulation of hybrid model. Figure 4-34 shows that spot weld fails in interfacial manner in KS2 shear. Adhesive remain in place and can bear additional loading.

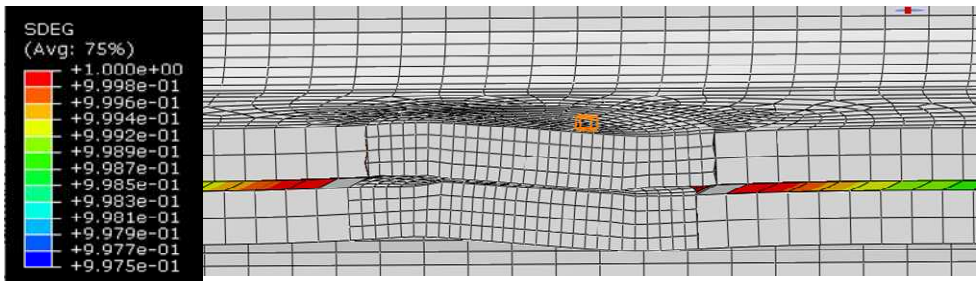

Figure 4-34. *WB failure under shear loading*

In Figure 4-34, spot weld rotation is also observed, however the angle is smaller than that of SW joint because the deformation of rotation in the spot weld vicinity is constrained by adhesive bonding. Figure 4-35 shows that rotation angle is *10.4°* in SW KS2 while it is *5.6°* in WB KS2. This indicates that in KS2, sheared spot weld sustains more shear in WB joint than in SW joint. Increasing shear force can lead to a premature failure of spot weld.

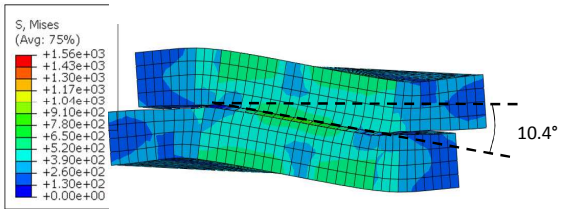

a) KS2 shear of SW

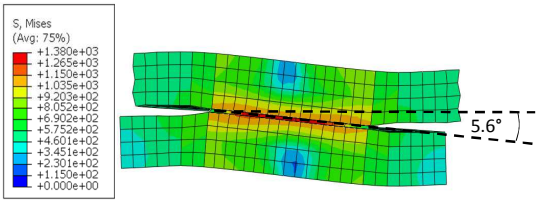

b) KS2 shear of WB

Figure 4-35. *Adhesive failure process under shear of weld bonded joint*

As recalled in Chapter 3, the WB joint ultimate strength is lower than that of AB joint. This could be explained by the diminution in adhesive area caused by the spot weld process. In the simulation, adhesive in the periphery of spot welds can be the new source of crack initiation after spot weld failure. Figure 4-36 shows element damaged near the spot weld.

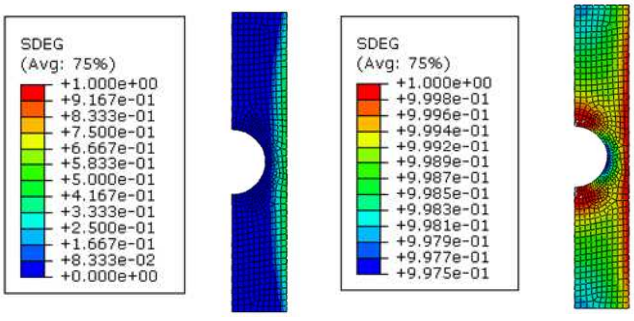

a) Step at loading start **b)** Step at spot weld failure

Figure 4-36. *Adhesive failure under shear near spot weld of WB joint*

In tension, peeling and lap-shear, two fracture stages (adhesive failure and spot weld failure) can be observed. Figure 4-37 shows the simulated damage process of WB joint under tension. After adhesive layer firstly fails in Figure 4-37 (b), cracks initiate at the notch tip of spot weld causing pull-out fracture, as shown in Figure 4-37 (c). It is obvious that the spot weld is the major contributor to the plastic deformation in WB joint.

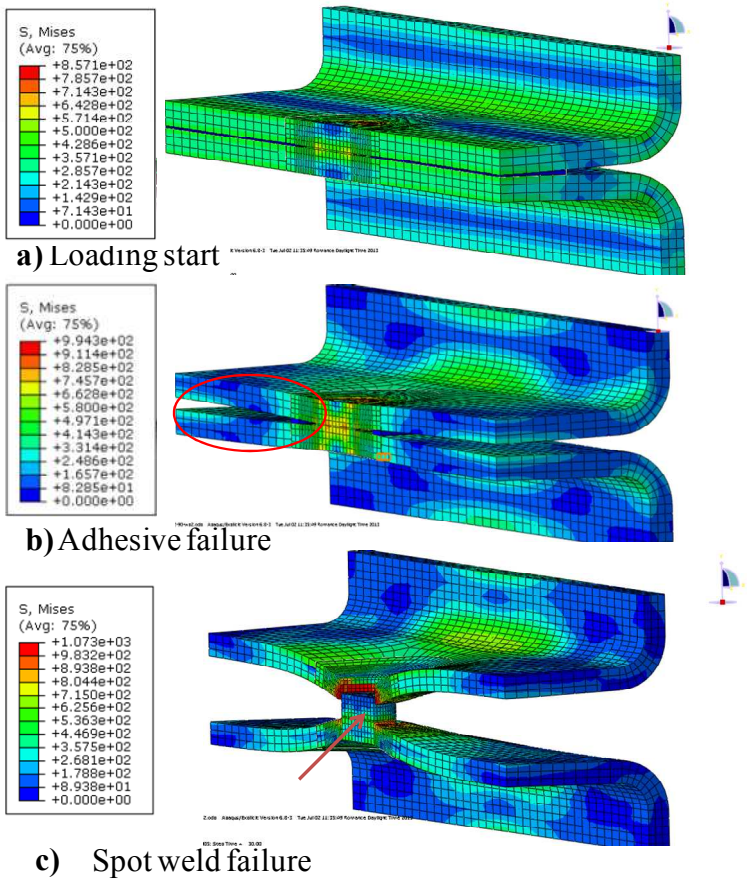

Figure 4-37. *Damage process of WB joint under tension loading*

Hybrid model gives good prediction for peeling load, as shown in Figure 4-33 (c). WB joint damage process is illustrated in Figure 4-38. Adhesive fails progressively till the front of cracks reached spot weld. Spot weld exhibits pull-out fracture with tearing of base metal.

In WB lap-shear joints, the whole faying surface can rotate with loading. The rotation leads to increasing components of tension force in adhesive layers and spot weld, like the AB lap-shear joint, as discussed in Figure 4-33. Adhesive has lower strength in pure tension than pure shear; hence WB lap-shear joints exhibit lower strength than KS2 shear.

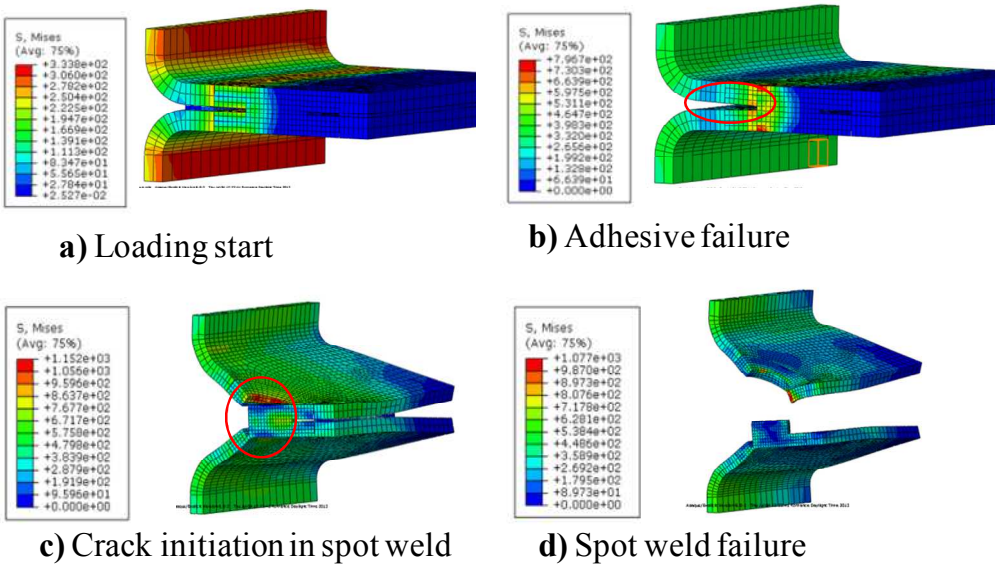

Figure 4-38. *Damage process of WB joint under peeling*

Additionally, increased component of tension force can defer the damage of spot weld because spot welds can provide large displacement under tension force. Consequently the adhesive is damaged prior to spot weld, as shown in Figure 4-39.

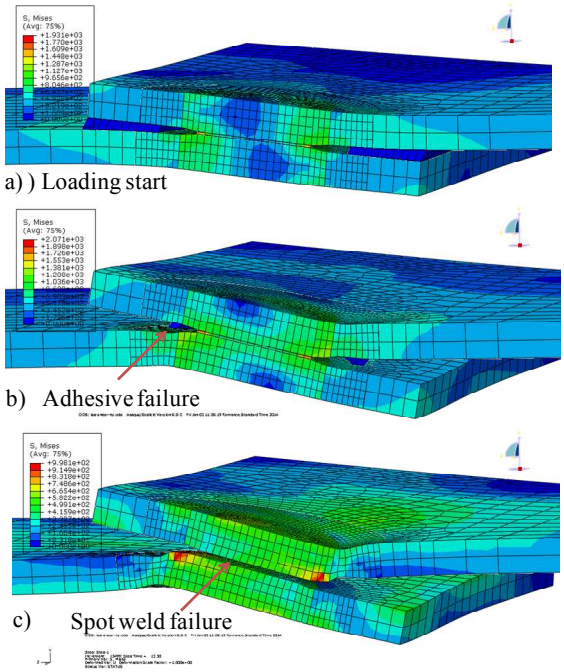

Figure 4-39. *Fracture process of WB lap-shear joint*

3. Connector model for spot weld

Automobiles body or aircrafts frames may contain more than thousands of spot welds or rivets [97]. The simulations of such structures are often faced with computational efficiency problems when using solid elements [98-99]. Hence, simplified models are developed to improve computation efficiency in crash simulation of whole car body. Various connector elements are available to represent different fasteners in Abaqus [87]. In this section, bushing type connector is selected to describe the spot weld behavior under complex loading condition.

3.1. Mesh independent fastener

The mesh-independent fastener is a convenient method to define point-to-point connection between two nodes. It can be easily applied to large structures such as spot welded car body since these systems contain large number of connections. The fastener can be located anywhere on the surface regardless of the mesh.

The fastener can be assigned variable connectors section for different purpose. Figure 4-40 shows fastener configuration. The connector is attached to two parts A and B in the attachment point position. Radius of influence determinates the fastener region in which the points are kinematicaly coupled with attachment points.

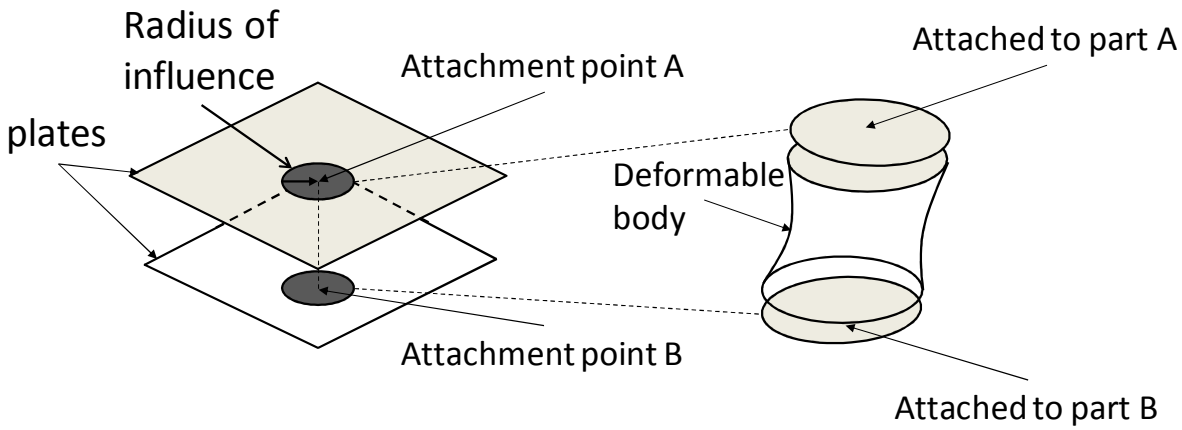

Figure 4-40. *Schematic description of mesh independent fastener*

3.2. Connector elements

3.2.1. Connector components

Connector elements can be used to represent connections such as spot welds or rivets [84]. Figure 4-41 shows the schematic description of bushing to model spot welds. Bushing type connector has six available components of relative motion: three translations along each axis (components 1-3) and three rotations around each axis (components 4-6).

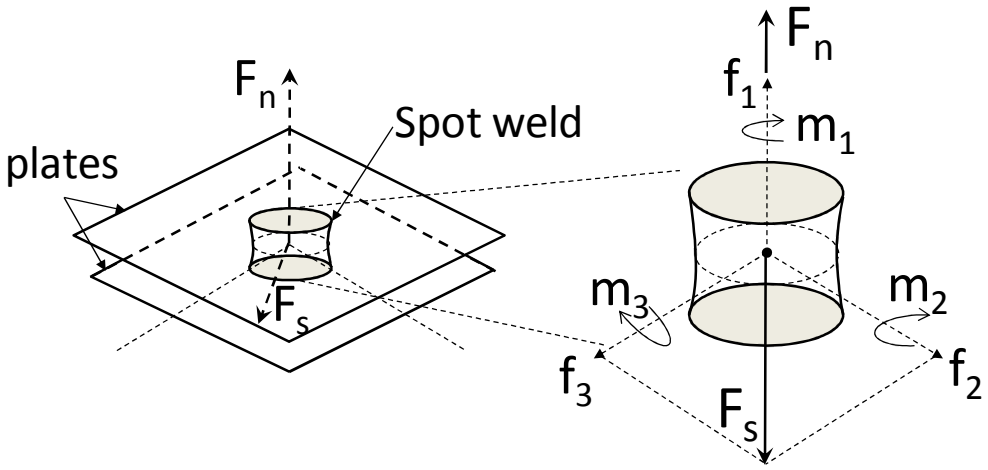

Figure 4-41. *Connector element modeling a spot weld (modified from [87])*

Since experimental data are available only in shear, tension and peeling by KS2 specimen, the connector can be defined in terms of normal, shear and bending force, as shown in Figure 4-41. Normal force can be defined by derived component f_1:

$$f_n = \langle f_1 \rangle \tag{4.27}$$

Shear force can be derived from f_2 and f_3:

$$f_s = \sqrt{f_2^2 + f_3^2} \tag{4.28}$$

Similarly, bending moment can be defined by moment around axis 2 and axis 3; torsion moment is defined by moment around axis 1.

$$m_b = \sqrt{m_2^2 + m_3^2} \tag{4.29}$$

$$m_t = m_1 \tag{4.30}$$

3.2.2. Connector elasticity and plasticity

Connector elastic behavior is defined by spring-like elasticity, as shown in Figure 4-42. The constitutive equation is given by:

$$F_i = D_{ii} u_i \ \ (no\ sum\ on\ i) \tag{4.31}$$

Where F_i is the force or moment in the i^{th} component of relative motion; D_{ii} is coming from the connector stiffness matrix; and u_i is the connector displacement or rotation in the i^{th} direction.

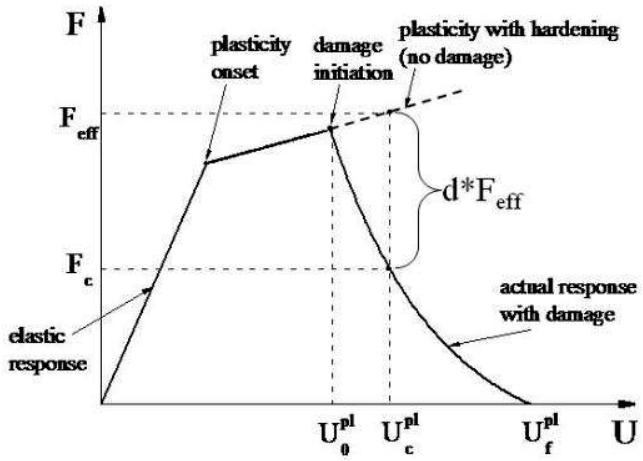

Figure 4-42. *Elastoplastic connector behavior with damage initiation and evolution.*

Connector plastic behavior is analogous to the plasticity formulation in classic metal plasticity. In connectors the stress (**σ**) corresponds to the force (**f**), the strain (**ε**) corresponds to the constitutive motion (**u**), the plastic strain ($\boldsymbol{\varepsilon}^{pl}$) corresponds to the plastic relative motion ($\mathbf{u}^{pl}$), and the equivalent plastic strain ($\bar{\varepsilon}^{pl}$) corresponds to the equivalent plastic relative motion ($\bar{u}^{pl}$). The yield function Φ is defined as:

$$\Phi(\mathbf{f}, \bar{\mathbf{u}}^{\mathbf{pl}}) = P(\mathbf{f}) - F^0 \le 0 \tag{4.32}$$

Where **f** is collection of forces and moments in the available components of relative motion that ultimately contribute to the yield function; P(**f**) defines a magnitude of connector tractions similar to defining an equivalent state of stress in von Mises plasticity. F^0 is the yield force/moment. The connector relative motions, **u**, remain elastic as long as $\Phi<0$; when plastic flow occurs, $\Phi=0$.

If yielding occurs, the plastic flow rule is assumed to be associated; thus, the plastic relative motions are defined by

$$\dot{u}^{pl} = \dot{\bar{u}}^{pl} \frac{\partial \Phi}{\partial \mathbf{f}}, \tag{4.33}$$

where $\dot{u}^{pl}$ is the rate of plastic relative motion and $\dot{\bar{u}}^{pl}$ is the equivalent plastic relative motion rate.

3.2.3. Connector damage

Damage initiation criterion of connector is defined in equation 4.34

$$\left(\frac{\langle f_n \rangle}{F_n}\right)^{a_1} + \left(\frac{f_s}{F_s}\right)^{a_2} + \left(\frac{m_b}{M_b}\right)^{a_3} + \left(\frac{m_t}{M_t}\right)^{a_4} = 1 \tag{4.34}$$

where, <> is Macauley bracket, $< \bullet >=0$ if $\bullet \leq 0$ and $< \bullet >= \bullet$ if $\bullet > 0$. It means negative normal force does not contribute to failure. F_n is measured ultimate normal force and F_s is measured ultimate shear force from KS2 tests. M_b and M_t are critical bending and torsion moment at failure respectively. M_b is difficult to measure directly; it can be calibrated by "trial-error" process on peeling test. a_1, a_2, a_3, and a_4 are parameters which define the damage surface. Figure 4-43 shows failure surface in 3D space when a quadratic function for damage initiation is used.

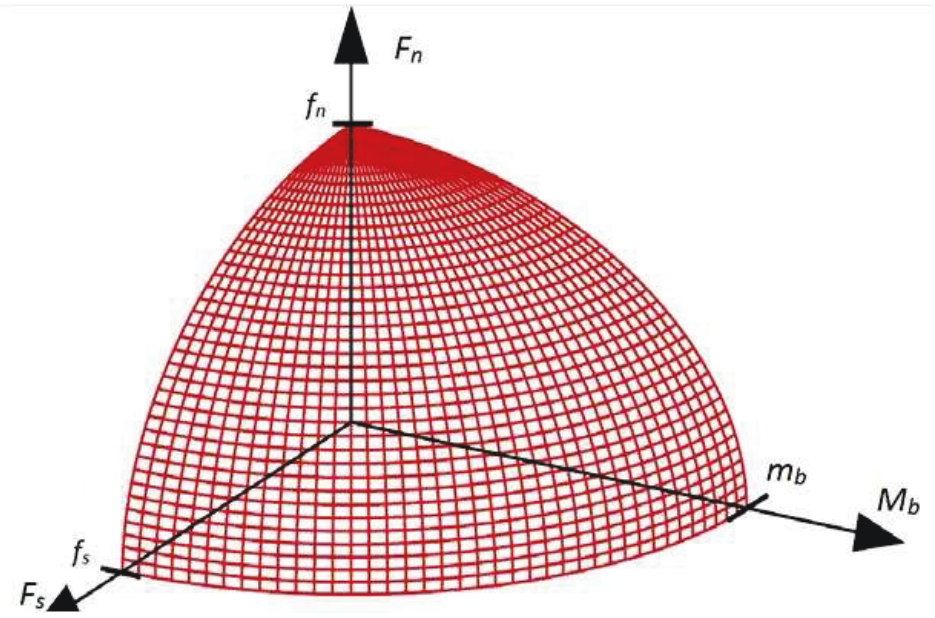

Figure 4-43. *Failure surface of connector in 3D (modified from [52])*

When the forces reach the critical value, connector will lose the force bearing capacity immediately. This is not realistic in pull-out fracture of spot welds. Consequently, damage

evolution criterion is needed to describe the degradation behavior in terms of damage variable *d*. The current force is calculated by:

$$F_c = (1-d)F_{eff} \tag{4.35}$$

where F_c is actual response at point c and F_{eff} is effective response with no damage. The damage variable d is defined as:

$$d = \frac{1-e^{-\alpha\frac{\bar{u}-\bar{u}_0^{pl}}{\bar{u}_f^{pl}-\bar{u}_0^{pl}}}}{1-e^{-\alpha}} \tag{4.36}$$

where $\bar{u}_0^{pl}$ is equivalent motion at plasticity initiation and $\bar{u}_f^{pl}$ is equivalent motion at ultimate failure, the difference $\bar{u}_f^{pl}-\bar{u}_0^{pl}$ must be specified. Parameter α is used to control the shape of damage evolution slope in the region of $\bar{u}_f^{pl}-\bar{u}_0^{pl}$, as shown in Figure 4-44. The evaluated force after damage initiation decreases rapidly as the exponent α inecreases.

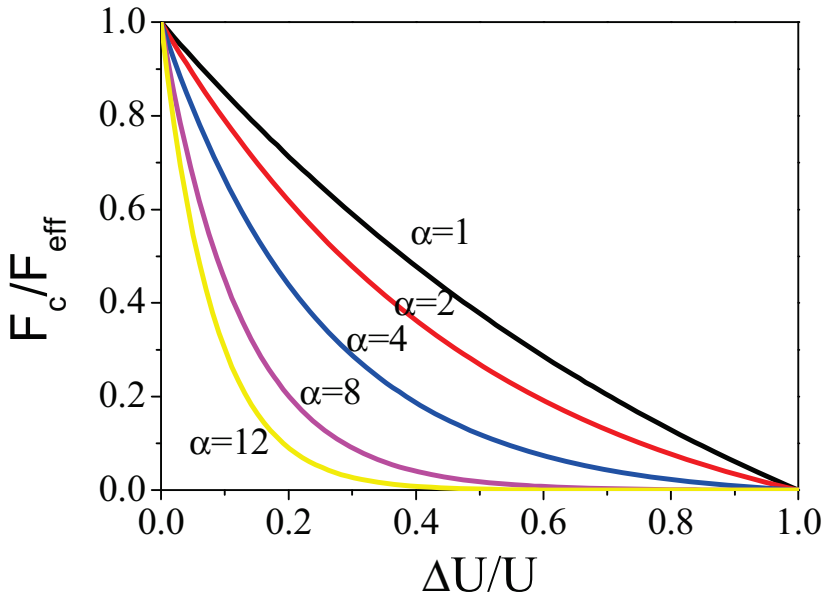

Figure 4-44. *Parameter α to describe the damage evolution*

In equation 4.36, $\bar{U}$ is defined as coupled motion-based damage evolution by the following equation

$$\bar{U} = \left(\frac{\Delta u_n}{U_n}\right)^{b_1} + \left(\frac{\Delta u_s}{U_s}\right)^{b_2} + \left(\frac{\Delta u_b}{U_b}\right)^{b_3} + \left(\frac{\Delta u_t}{U_t}\right)^{b_4} \tag{4.37}$$

where U_n, U_s, U_b and U_t are the equivalent relative motion in normal, shear, rotation and torsion, respectively. These parameters can be calibrated with the help of comparison of damage evolution between measurements and simulations. The connector fails totally when $\bar{U} = \bar{u}_f^{pl} = 1$.

A quadratic function for damage initiation is used, hence we can give $a_1=a_2=a_3=a_4=2$. Coupled motion-based damage evolution was used, a quadratic function can be used to depict the coupled behavior, $b_1=b_2=b_3=b_4=2$. Spot weld diameter r_{inf} is given by 2.9, equal to measurement value. The parameters of connector for spot welds simulation are reported in Table 4-4. The moment parallel to panel surface is ignored since the torsion damage is not taken into account in this work. Hence, torsion moment can be defined as rigid.

Table 4-4. *Parameters of connector for damage initiation and evolution of spot welds joint*

F_n (kN)	F_s (kN)	M_b (Nm)	M_t (Nm)	a_1	a_2	a_3	a_4	r_{inf} (mm)
12	20.4	15600	10^6	2	2	2	2	2.9
U_n (mm)	U_s (mm)	U_b (Rad)	U_t (Rad)	b_1	b_2	b_3	b_4	α
5	1	2	10^6	2	2	2	2	3.5

3.3. Validation of the connector element for spot weld

Based on the previously described simplified constitutive model, a finite element model is developed for the SW joint analysis. The BM is meshed with 3D shell elements. The material property of BM has an elastoplastic model without damage. Spot welds are represented by connector elements. The two sheets are connected by bushing fastener. The boundary conditions for simulation keep the same as that of KS2 solid model. Figure 4-45 shows predicted force-displacement curves under different loadings.

As regards shear loading, the model can accurately predict the strength as well as the displacement, as shown in Figure 4-45 (a). For tension, Figure 4-45 (b) shows that predicted strength are also acceptable while the stiffness is under-prediction. The model can predict the ultimate strength of peeling. However, the prediction cannot capture the “tear-out” damage mode.

It can be concluded that the simplified model can predict the overall response of spot weld with compromise between accuracy and computational cost.

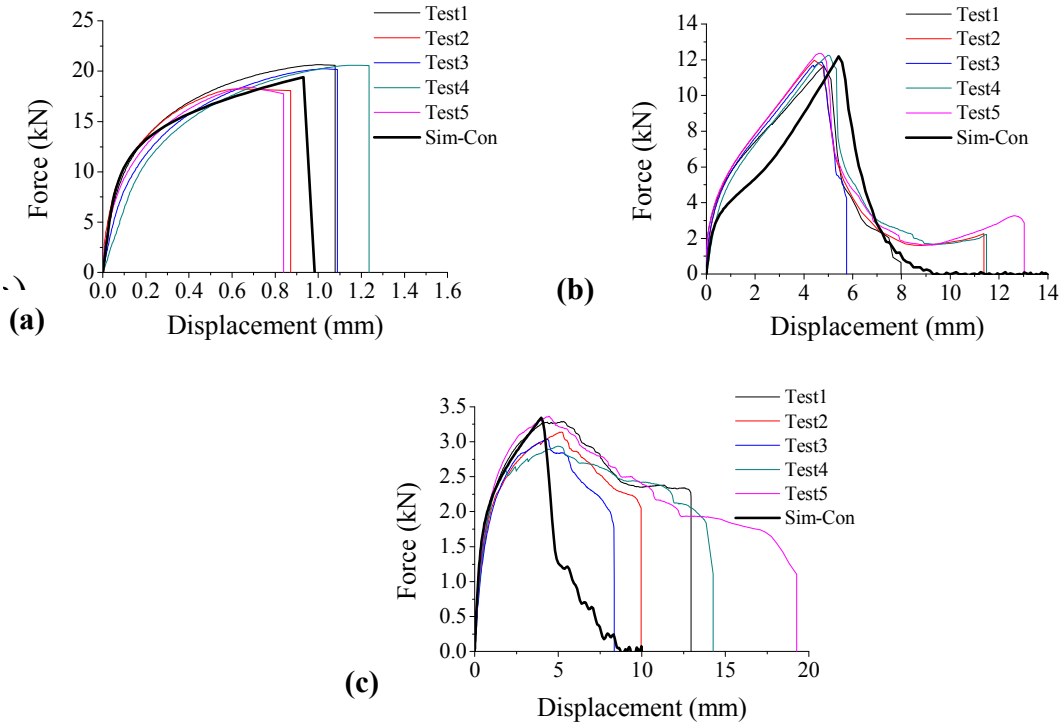

Figure 4-45. *Prediction from shell connector model of spot welded KS2 specimen: (a) shear, (b) tension and (c) peeling*

Figure 4-46 shows connector damage and deformation of base metal in spot welded zone. Connector elements can fully capture the spot welds behavior including elasticity, plasticity and damage. The links between the two sheets are deleted when connector element are totally damaged. Simplified model can predict the rotation of spot weld in shear and base metal deformation of tension and peeling.

The aim of simplified model is to simulate large components with reasonable computational cost. In Explicit method, the stable time step is the key factor that influence the total computational time. Jousset reported that the acceptable stable time step by BMW is Δt=1E-06 *s* for car body simulation [6]. In this work, with the help of mesh-independent fastener and shell element, the stable time step can be increased.

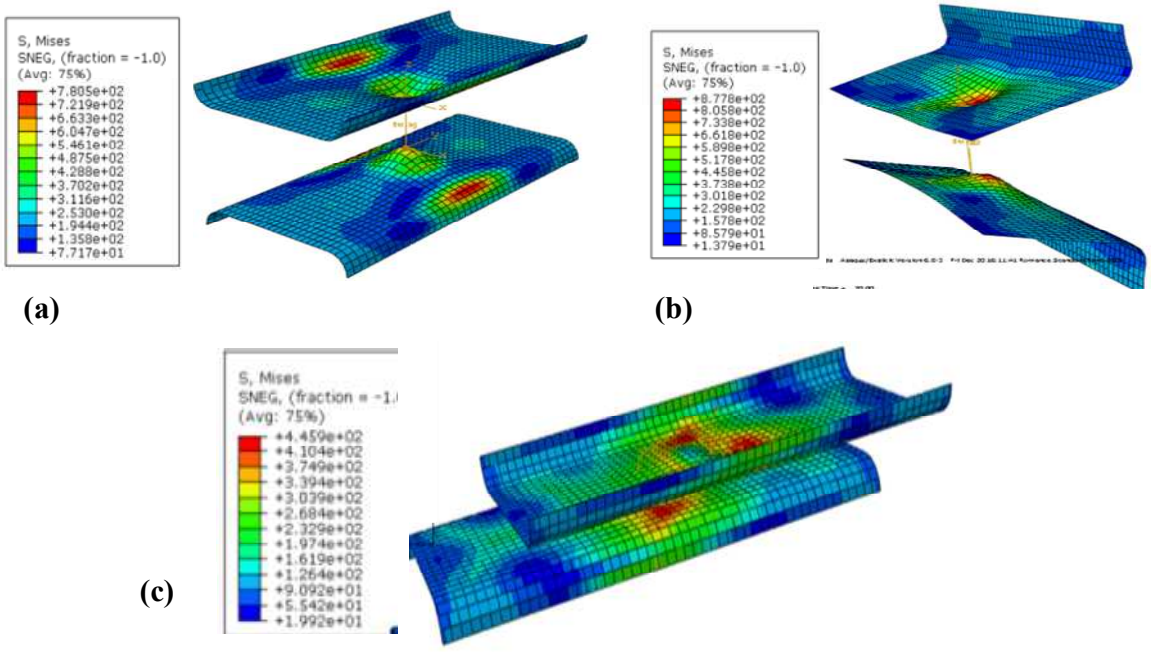

Figure 4-46. *Simulation of connector damage by shell connector model (a) tension (b) peeling and (c) shear*

Table 4-5 gives the comparison of CPU time between solid model and connector model. Connector element for spot welds can increase initial time increment and cut CPU time for the same KS2 simulation. Moreover, coarse meshes can be assigned to base metal by the help of mesh independent fastener.

Table 4-5. *CPU time for KS2 analysis comparison between solid model and connector model*

	Minimum element length	**Initial time increment**	**Total CPU time**
Solid model	*0.5 mm*	*1.36966E-09 s*	*1.23s*
Simplified model	*2 mm*	*1.507481E-07s*	*0.34s*

4. Conclusion

The Gurson model and CZM are used to predict spot weld rupture under different loading conditions. Additionally, simplified model (shell+connector) is developed for large spot welded structure simulations because of their computational efficiency. The adhesive behavior is

predicted by CZM. Finally, complex model combining spot weld model and adhesive model is used to estimate WB joints response. The main conclusion can be summarized as follow:

- HAZ and WM properties have significant influence on damage modes and strength of spot weld. The heterogeneity of material in spot weld can be taken into account by scaling the flow stress of BM.
- Inverse identification can be efficiently used to calibrate scaling factors of BM and HAZ.
- Gurson model can accurately predict ductile fracture in BM and HAZ of spot weld. However, it has no capacity to predict quasi-shear fracture in WM, e.g. KS2 shear loading.
- CZM has the advantages of requiring limited input data and enable higher computational efficiency. It can efficiently be used to predict interfacial fracture of spot welds.
- The Gurson model combined with CZM can predict various fracture modes of spot welds.
- CZM has limited capacity to predict the ultimate strength of AB in small scale specimens due to the impossibility to predict plasticity. It can be used to predict the behavior of T-joints in which the overall response is not sensitive to adhesive plasticity. This will be discussed in the next chapter.
- A complex model combining spot weld model and adhesive model can be used to predict the mechanical behavior of WB joints under different loading condition even if it slightly over-predicts the strength.
- Simplified model (shell+connector) can efficiently estimate the strength and displacement of spot welded joints under complex loading. Their computational efficiency allows simulating large T-joint specimens.

Chapter 5. Case study

The joints in car body are cause of potential failure during vehicle crash. Such a failure should be accurately predicted by numerical model if the latter is to be reliably used in the design process [103]. As discussed in Chapter 4, only simplified models are acceptable for simulation of large structures. Therefore, CZM and connector elements are used, in this chapter, to investigate a T-joint that can represent the B-pillar junction. The results of T-joint tests under longitudinal and transverse loading are firstly discussed in terms of loading capacities and energy absorptions. Then the T-joints are analyzed using finite element models. The predictions from the models are compared with measurements for validation purpose.

1. Description of T-joint specimens

The so-called T-joints are widely used to assess the behaviors of different joints [84] [104] in particular the B-pillar junction. The B-pillar is designed to support the vehicle's roof panel, as well as for latching the front door and mounting the hinges for the rear doors [105]. B-pillar is thought to be the most complex of all the vehicle structures as it may undergo longitudinal and transverse loading in car crash test, corresponding to front and side impact respectively, as depicted in Figure 5-1.

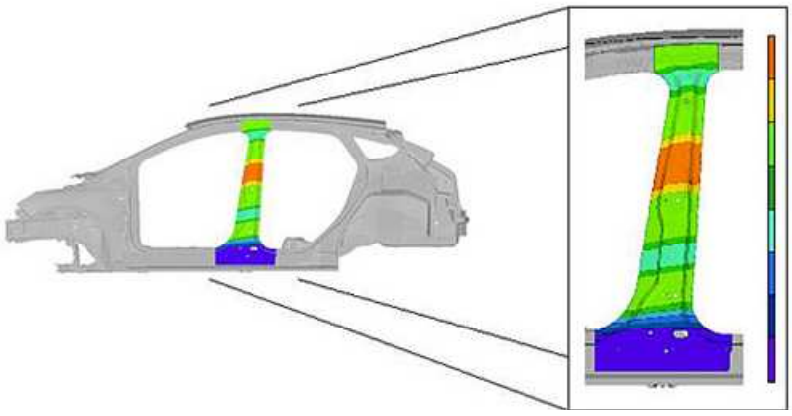

Figure 5-1. *B-pillar of car body [106]*

T-joint consists of a vertical column and a horizontal beam, as shown in Figure 5-2. The two parts are joined together on faying surfaces. Single spot weld is performed in the center of each horizontal faying surface while three spot welds are achieved in the vertical faying surface as

illustrated in Figure 5-2 (a). The spot welds are numbered from 1 to 5. In the adhesively bonded joint, the spot welds are replaced by adhesive on the same surfaces, as shown in Figure 5-2 (b). The thickness of adhesive layer is *0.3 mm*. The dimension of the two horizontal faying surfaces is *16× 45 mm*. The vertical faying surface is *18×50 mm*. All the spew fillets are removed to control accurately the bonded surface. Figure 5-2 (c) shows weld bonded T-joint, in which spot welds are combined with adhesive to make hybrid joint.

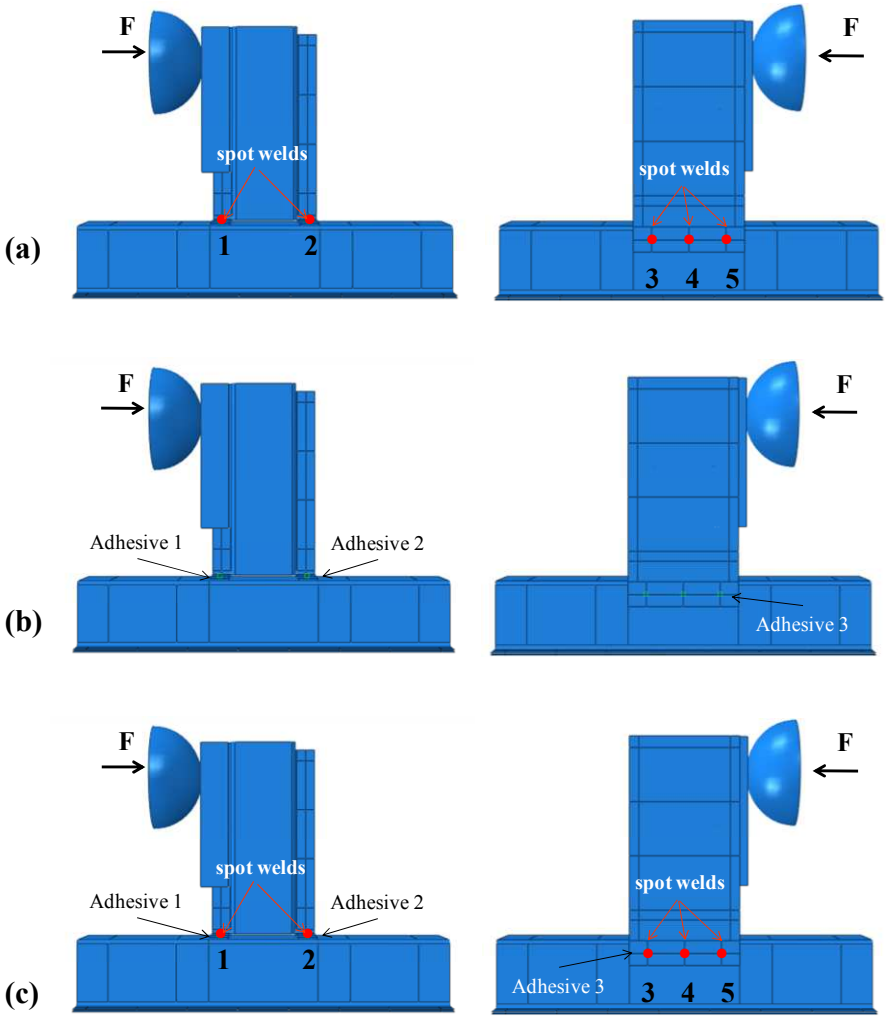

Figure 5-2. *Illustration of T-joints: (a) spot welded, (b) adhesive bonded and (c) weld bonded*

2. Testing of T-joints

Horizontal beams of T-joint are fixed on both ends by clamps, which consist of internal massive block and exterior clamps, as depicted in Figure 5-3. The exterior clamps are bolted to

guarantee full contact between internal blocks and horizontal beam. Loading is applied by a hemispherical punch on the exterior block, which is associated with an internal block to enhance the stiffness of vertical column. These blocks prevent excessive plastic deformation which would affect the measured displacement.

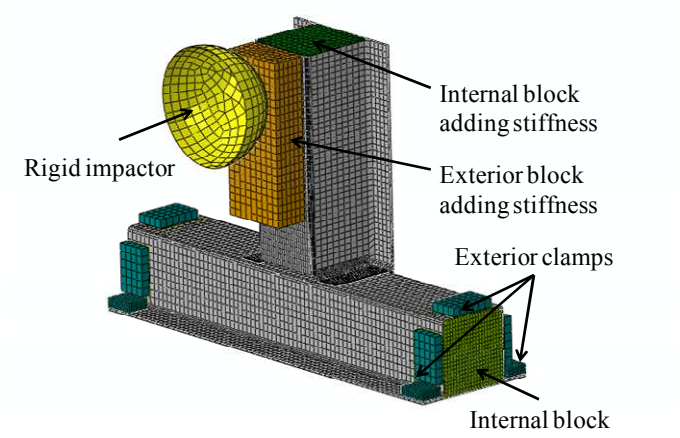

Figure 5-3. *Configuration of T-joint tests setup*

Preliminary investigation shows that excessive deformation took place on base metal in hybrid joints, instead of the damage of joints. Therefore, a block is placed inside the horizontal beam to increase the stiffness of T-joint, as shown in Figure 5-4.

Figure 5-4. *Stiffness block placed inside the horizontal beam*

Figure 5-5 shows the setup of longitudinal loading. The loading force, parallel to the horizontal beam and located *25 mm* from the end of the vertical column, is measured by internal loading cell. For the quasi-static test, the punch velocity is *10 mm/min* and the punch displacement along the edge of the horizontal beam is measured.

Figure 5-5. *T-joint test setup under longitudinal loading*

The setup for the transverse loading is the same as that of longitudinal loading with the exception of the force direction that is perpendicular to the horizontal beam as depicted in Figure 5-6. As the hybrid joint performance is assessed by comparison with adhesively bonded joint and spot welded joint, all three types of joints are tested.

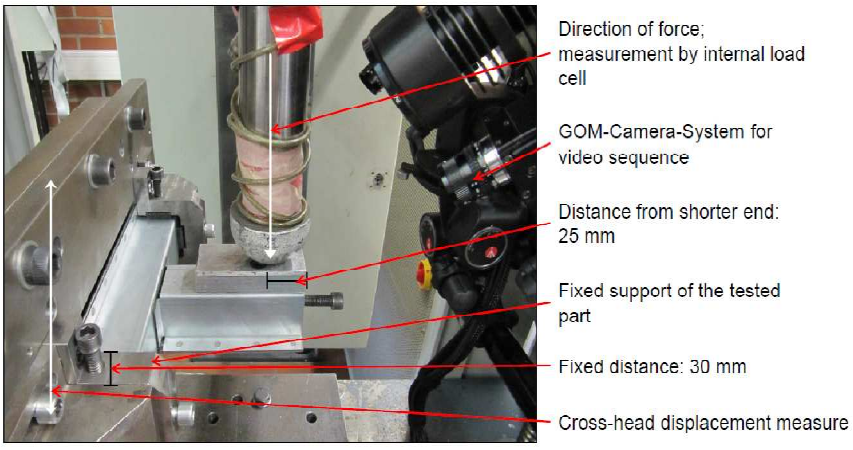

Figure 5-6. *T-joint test setup for transverse loading*

2.1. Test results from SW T-joint

Figure 5-7 (a) shows the measurements of force-displacement curve of SW T-joint under longitudinal loading. Except the spot weld N° 2, the other spot welds damaged successively at the different peaks of force. Both interfacial damage and pull-out damage modes of spot weld are observed in T-joint. Under transverse loading, as shown in Figure 5-7 (b), the two spot welds on horizontal surface (N°. 1 and N°. 2) are damaged almost at the same time while the spot welds on vertical surface (N°. 3, N°. 4 and N°. 5) remain undamaged.

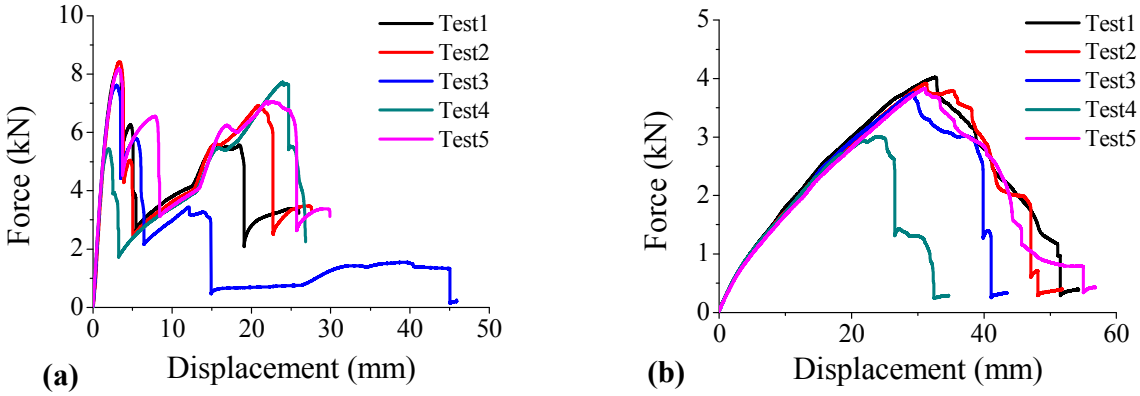

Figure 5-7. *T-joints test of SW: (a) longitudinal loading and (b)transverse loading*

2.2. Test results of AB T-joint

AB T-joint tests are well reproducible in both transverse and longitudinal loading. Under longitudinal loading, adhesive layer on vertical surface (adhesive-3) undergoes shear loading while the layer adhesive-1 on horizontal surface undergoes complex loading combining tension and shear. The ultimate strength is about *13 kN*, as shown in Figure 5-8 (a).

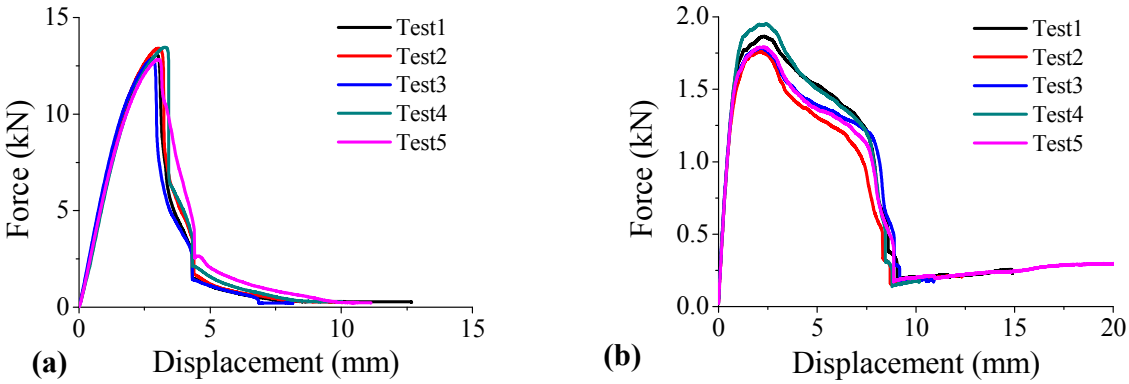

Figure 5-8. *AB T-joints test : (a) longitudinal loading and (b)transverse loading*

Under transversal loading, two layers on horizontal surfaces (adhesive-1 and adhesive-2) are damaged simultaneously. The force-displacement curve is shown in Figure 5-8 (b). Average ultimate strength is about *1.7 kN*.

2.3. Test results from WB T-joint

Among the five tests under longitudinal loading, four are fairly well reproducible. As depicted in Figure 5-9 (a), the WB T-joints exhibit damage modes similar to those exhibited by SW T-joints. It should be noted that Test 1 is carried out without the stiffening block inside the horizontal beam which leads to low strength compared to the other tests.

As regards the transversal loading, two-stage failure is observed as depicted in Figure 5-9 (b). Test 1 is again performed without any block inside the horizontal beam and the low strength exhibited by Test 3 is due to its small spot weld nugget diameter.

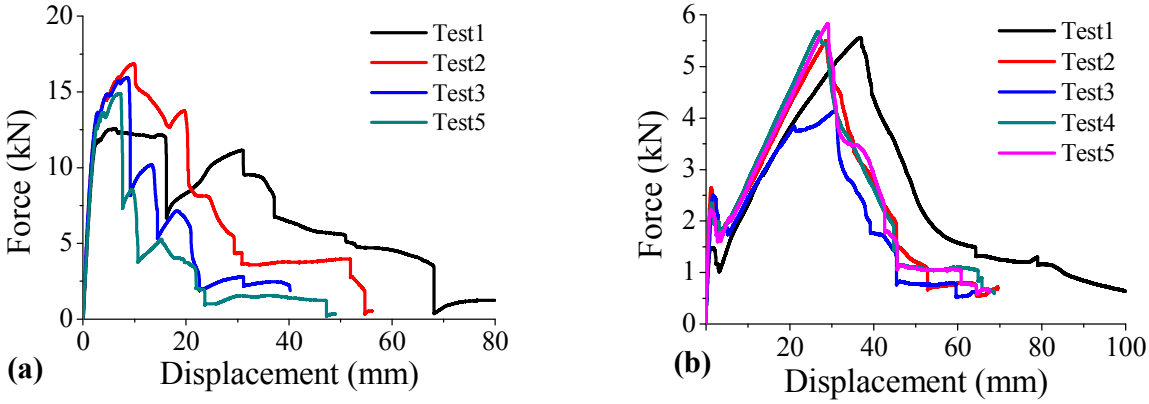

Figure 5-9. *WB T-joints test: (a) longitudinal loading and (b)transverse loading*

2.4. Cross comparison of different joining methods

The comparison between different KS2 and lap shear specimens reported in section 3.4 showed that the WB joints exhibit a distinctive behavior both in terms of strength and energy absorption. Similarly, cross comparisons are carried out to investigate the influence of joining method on the behaviors of large T-joints. The energy absorption was obtained by calculating the surface under force-displacement curves. Figure 5-10 (a) gives the comparison between SW, AB and WB joint under longitudinal loading. WB joint exhibits the highest strength and displacement, due to the combination of high stiffness conferred by the adhesive and large plastic deformation conferred by the spot welds. The strength of AB joints is higher than SW joint because of severe

shear on the vertical surface that causes large displacement with SW joint. Therefore, SW joint has higher energy absorption than AB joint. The energy absorption by WB joint is the highest one, *6.3 times* than that of AB joint, and *2 times* than that of SW joint, as shown in Figure 5-10 (b).

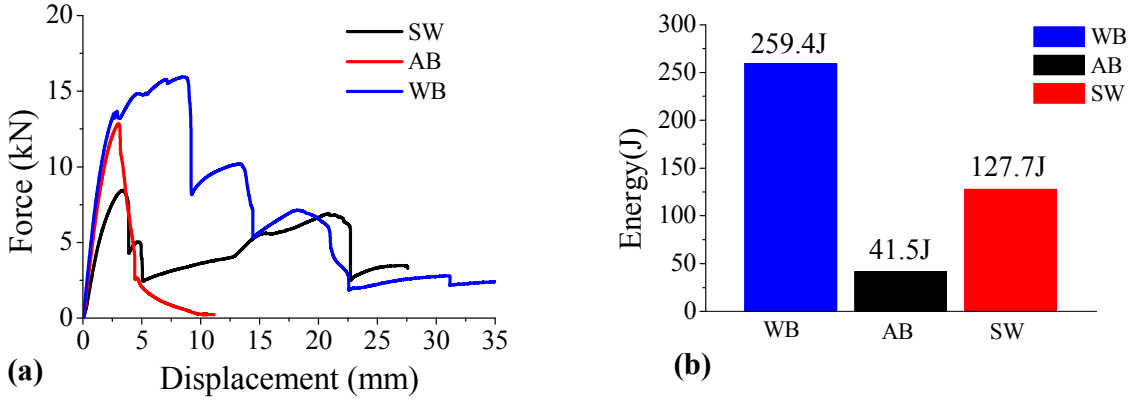

Figure 5-10. *Comparison between different T-joints under longitudinal loading: a) force-displacement curve, b) energy absorption*

Figure 5-11 shows the damaged SW and WB T-joints. Spot welds on vertical surface exhibit same damage modes on both SW and WB T-joint.

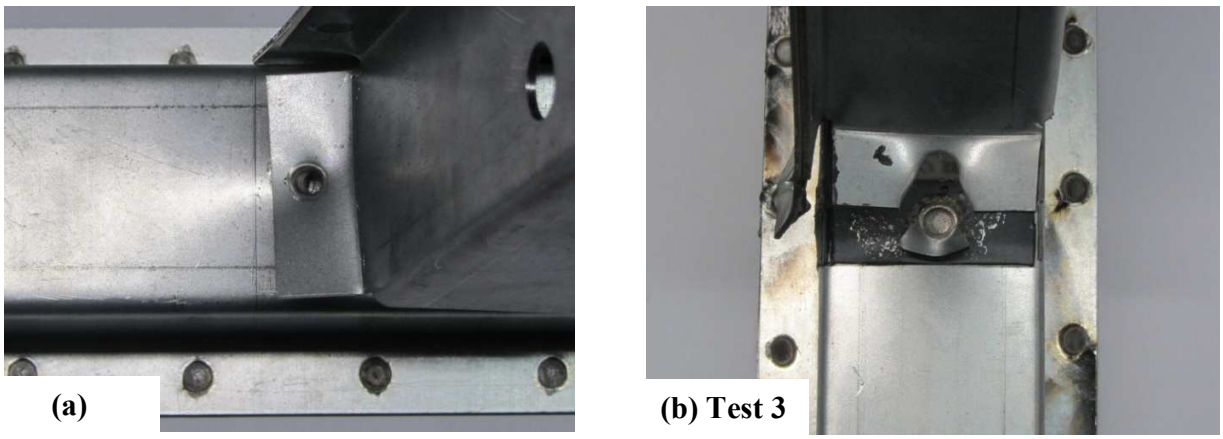

Figure 5-11. *Images of damaged T-joints specimens: (a) SW T-joint (b) WB T-joints*

However pull-out fracture was observed on SW while mixed fracture mode combining pull-out and tearing was observed on WB T-joints due to the adhesive, as shown in Figure 5-11 (a) and (b). In the mixed mode of WB T-joint, cracks initiate at the interface of HAZ/WM, and then propagate to the exterior edge by tearing the spot welds out of BM. Consequently, WB provides the highest strength and energy absorption among the 3 kinds of joints.

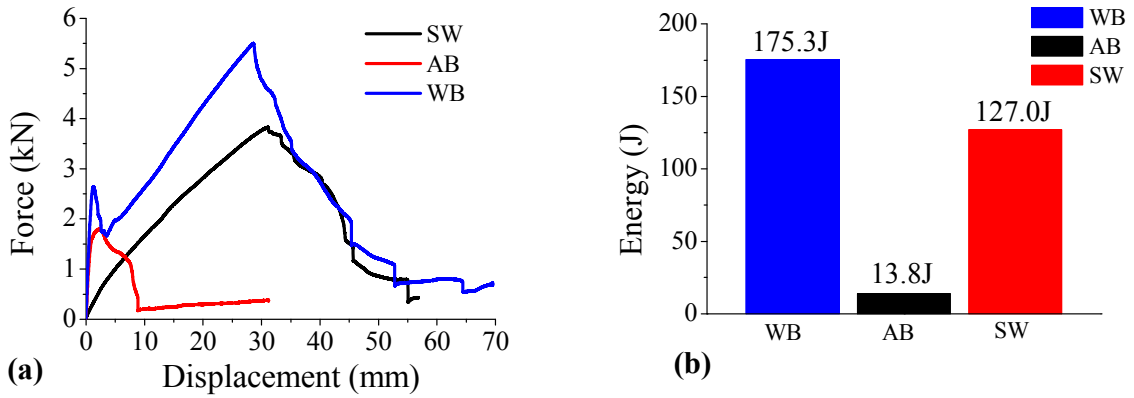

Figure 5-12. *Comparison between different T-joints under transverse loading: a) force-displacement curve, b) energy absorption*

Figure 5-12 shows the cross comparison between different T-joints under transverse loading. Similarly to the previous comparisons, weld bonded joints exhibit the maximum strength and energy absorption, two stages damage was observed in WB T-joint, as shown in Figure 5-12 (a), the energy absorption of WB joints is up to *175.3 J*, *38%* more than that of SW T-joints and the AB T-joint exhibits the lowest energy absorption.

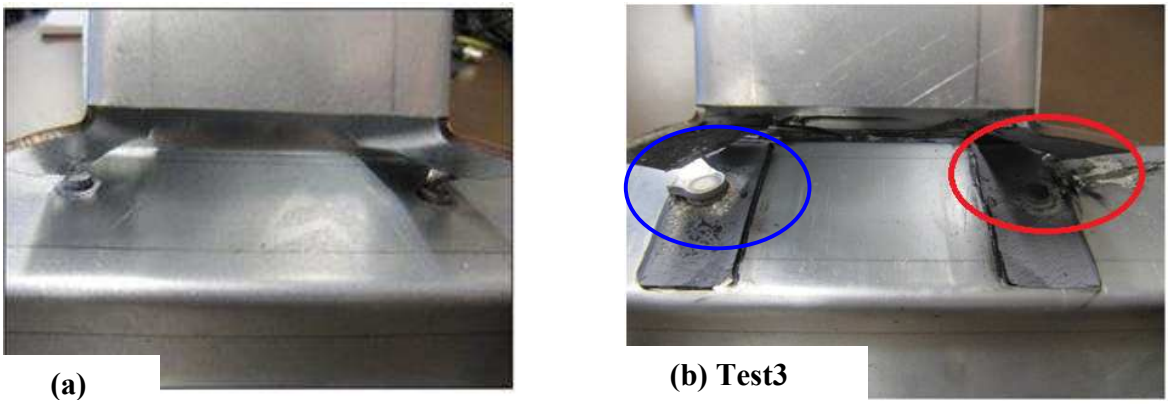

Figure 5-13. *Images of damaged T-joints specimens: (a) spot welds on vertical surface of SW T-joints, (b) spot welds on vertical surface of WB T-joints*

The damaged specimens are depicted in Figure 5-13. All spot welds exhibit "pull-out" fracture mode over the 5 tests of SW T-joint, as shown in Figure 5-13 (a). As regards WB T-joint, only one of two spot welds (outlined in red) in Test 3 shows pull-out fracture while all the spot welds of other tests of WB T-joint exhibit "tear-out" mode (outlined in blue), as shown in Figure 5-13 (b). It should be noted that the "tear-out" mode can exhibit higher strength than "pull-out" mode.

Consequently, Test 3 exhibits lower strength than the others in WB T-joints, as shown in Figure 5-9 (b).

It should be also noted that although a small amount of adhesive is used, adding adhesive to spot welds deeply affects both the strength and the energy absorption of large scale component joints. Furthermore, WB T-joint shows the tendency of spot welds to change from pull-out fracture mode to mixed fracture mode. This brings benefit to joined structure as tearing fracture mode provides high energy absorption, especially in the case of crash.

3. FEM analysis of T-joints

3.1. Predictions from the spot welded T-joint model

Large structures are generally meshed with structural elements, such as shell element, beam, truss, etc…, for computational efficiency purpose. Meanwhile, the joints are represented by special elements.

Figure 5-14 shows that the predictions are in good agreement with measurements both in terms of strength and displacement under both longitudinal and transverse loading. As regards longitudinal tests, spot welds failed consecutively with displacement and their damage results in a peak on force-displacement curve, as shown in Figure 5-14 (a). The two spot welds in horizontal surface are damaged simultaneously in transverse loading. This can be proved by single peak on the force-displacement curves, as shown in Figure 5-14 (b).

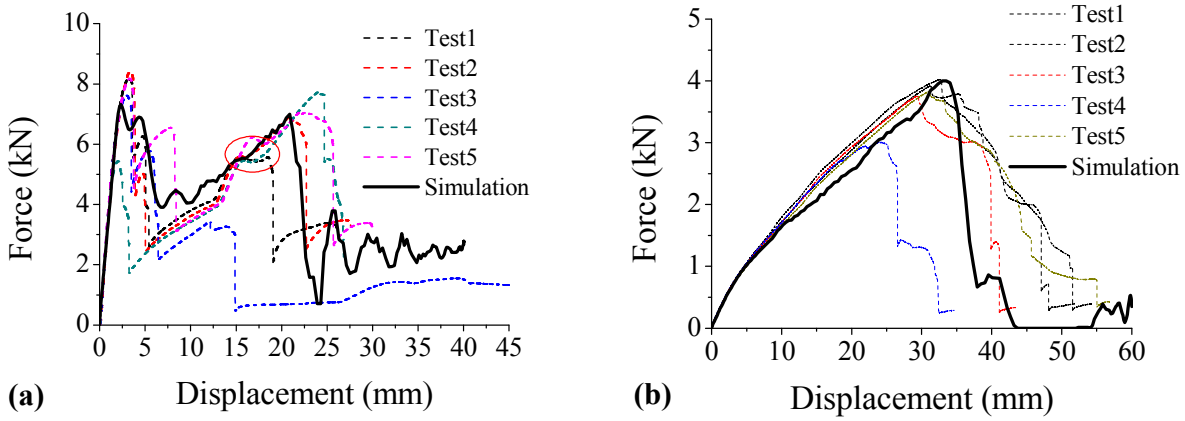

Figure 5-14. *Comparison between predictions and measurements of spot welded T-joint: (a) longitudinal load, (b) transverse loading*

In this work, T-joint components are meshed with shell elements (S8R) and spot welds are represented by fastener with connector section as described in section 3 of Chapter 4.

For each joining method, the simulations are carried out under longitudinal and transverse loading.

Figure 5-15 shows the predicted spot weld failure under longitudinal loading. Right Y axis represents the damage of spot weld. Spot weld loses load carrying capacity when damage evolution reached its criteria. S1, S4 and S5 are damaged in different modes, as shown in Figure 5-15 (a) and (b).

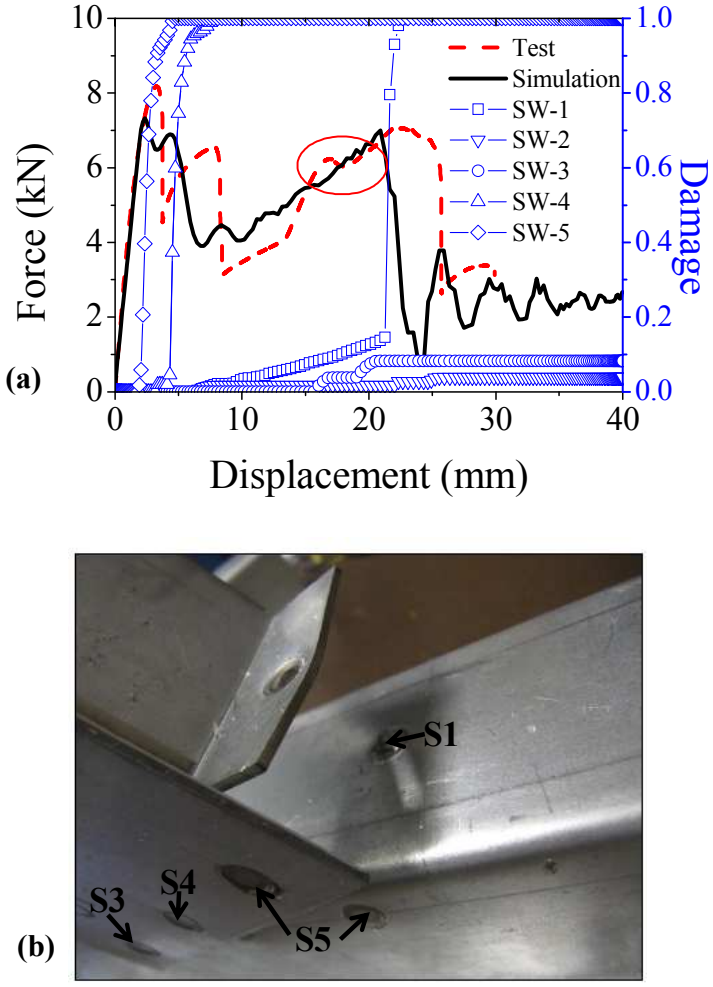

Figure 5-15. *Failure of spot welds under longitudinal loading*

Simplified model of spot weld cannot predict the damage due to torsion force. Consequently the failure peak on test (red dash line) of spot weld outlined by red circle in Figure 5-15 (a) is not predicted by simulation. This spot weld is denoted S3 in Figure 5-15 (b).

Figure 5-16 shows the deformed shape and the contour plot of equivalent plastic strain. It clearly shows that the deformed shape is well captured by the model. Plastic strain is observed in the vicinity of two damaged spot welds. In longitudinal loading, the maximum plastic strain occurs close the spot weld S3.

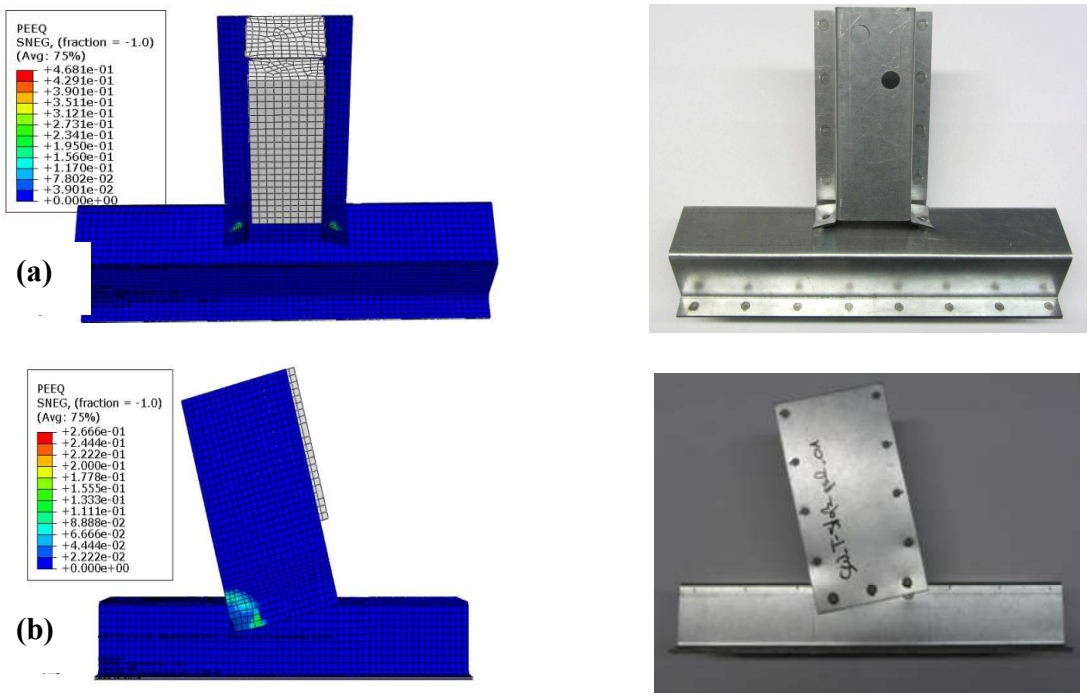

Figure 5-16. *Predicted deformed shape* vs. *experiment image and equivalent plastic strain of SW T-joint under (a) transverse loading and (b)longitudinal loading*

3.2. Predictions from the AB T-joint model

Previous research [6] reported that the spew fillet can affect the response of AB joint. That is why the internal spew fillets, that are difficult to remove, are taken into account in our finite element model as depicted in Figure 5-17.

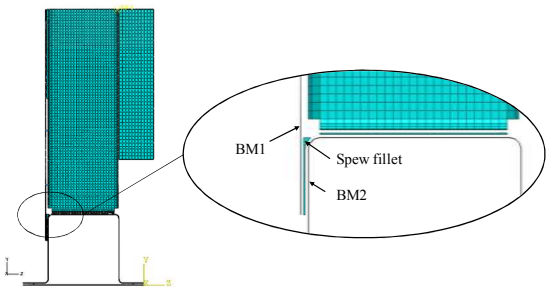

Figure 5-17. *Modeling spew fillet in vertical surface of AB T-joint*

Figure 5-18 shows comparison between the predictions from the finite element model and measurements under longitudinal and transverse loading. The predictions are considered acceptable although the strength is slightly underestimates under longitudinal loading, as shown in Figure 5-18 (a).

As regards the transverse loading, the predicted strength is in good agreement with measurements, as shown in Figure 5-18 (b), while the model cannot capture the plastic softening in base metal.

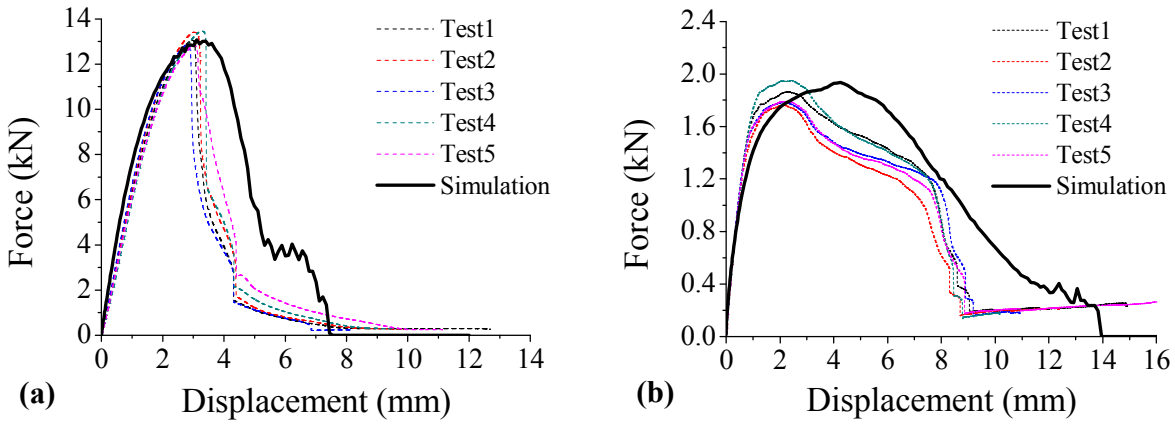

Figure 5-18. *Predictions vs. measurements of AB T-joint under (a) longitudinal loading and (b) transverse loading*

As regards AB T-joint, Figure 5-19 shows a comparison between the deformed shape from the finite element model and the damaged image from test. It clearly shows that rupture is limited to the adhesive layer. There is no significant plastic strain in base metals. Therefore stress contour is plotted to compare with experiments.

Only small stress concentration is observed in the vicinity of bonded area of base metal. The stresses within the faying surfaces are uniform in both loading cases.

Since adhesive can provide uniform stress distribution, it can be supposed that increasing faying surface can efficiently increase the strength of adhesive bonded joint.

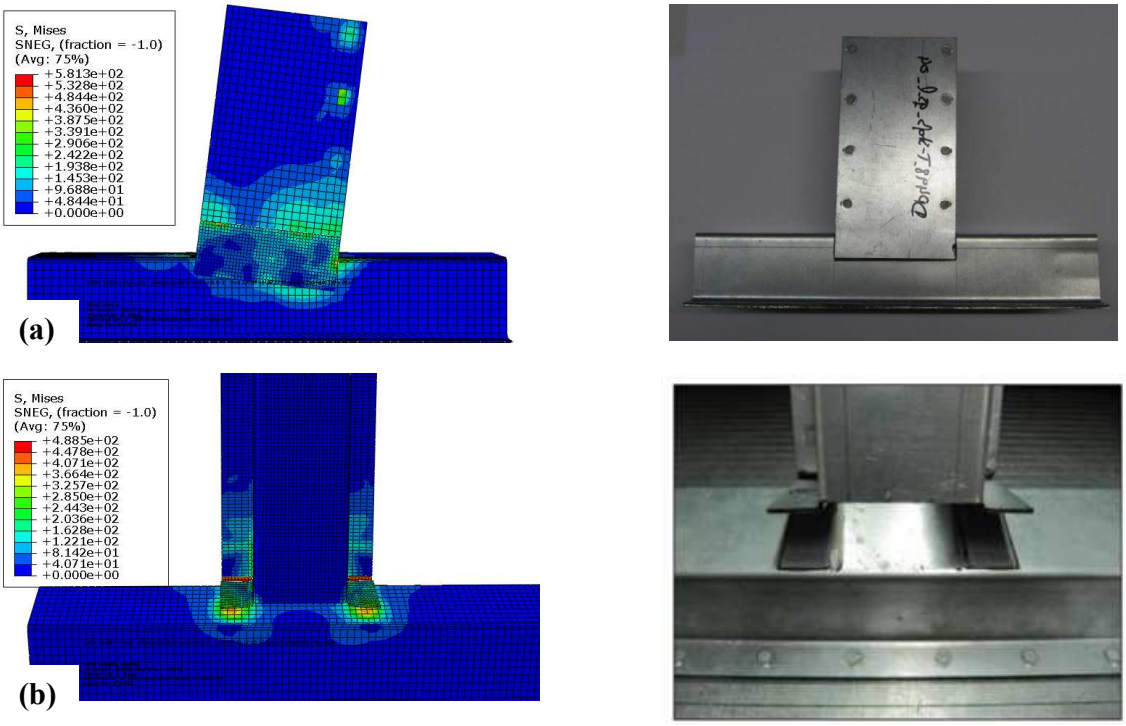

Figure 5-19. *Predicted deformed shape vs. test picture of AB T-joint under (a) longitudinal loading and (b) transverse loading*

3.3. Predictions from WB T-joint model

The models developed for AB and SW T-joint simulation are combined here to predict WB T-joint. BM is discretized with the help of 3D shell element with *5 mm* size, adhesive layers are modeled by cohesive model and fastener with connector element is used to represent spot welds, as depicted in Figure 5-20.

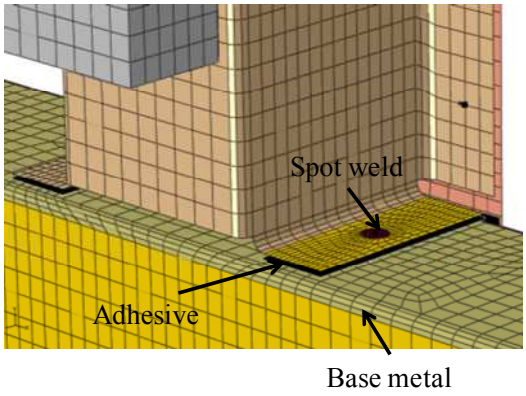

Figure 5-20. *Modelling configuration of WM T-joint*

The connector stiffness along the direction 1, 2 and 3 for simulation are represented by E_1, E_2 and E_3, as summarized in Table 5-1. The rotation stiffness about each axis is denoted by E_4, E_5 and $E6$. All the rotation stiffness is rigid in the analysis.

Table 5-1. *Stiffness of connector for translation and rotation*

E_1 (N/mm)	E_2 (N/mm)	E_3 (N/mm)	E_4 (N·mm/rad)	E_5 (N·mm /rad)	E_6 (N·mm /rad)
3.47e+06	1.33e+06	1.33e+06	Rigid	Rigid	Rigid

As regards WB T-joint, it was observed that spot welds on horizontal surface exhibit pull-out fracture with fracture initiation in HAZ/BM rather than in HAZ/WM as in SW T-joint. The ultimate strength in former is higher than latter as discussed in section 3.3.2 in Chapter 3. Hence, the force for damage initiation in pure tension is scaled by *22.7%* for WB T-joint simulation, as shown in Table 5-2.

Table 5-2. *Parameters of connector for damage initiation and evolution of spot welds in WB joint*

F_n (kN)	F_s (kN)	M_n (N·m)	M_t (N·m)	a_1	a_1	a_1	a_1	r_{inf} (mm)
14.7	20.7	16500	10^6	2	2	2	2	2.9
U_n (mm)	U_s (mm)	U_b (Rad)	U_t (Rad)	b_1	b_2	b_3	b_4	α
5	1	2	10^6	2	2	2	2	3.5

The predictions with original and scaled parameters are compared with measurements under longitudinal and transverse loading, as depicted in Figure 5-21.

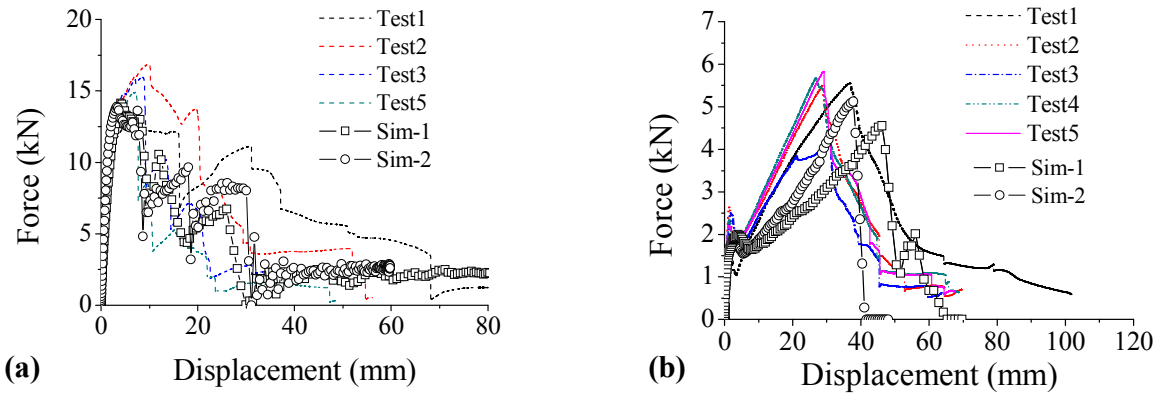

Figure 5-21. *Simulation vs. measurement of WB T-joint: (a) longitudinal load (b) transverse load*

The predictions using the original parameters and scaled parameters are denoted *Sim-1* and *Sim-2* respectively. Obviously, the predictions obtained with the original parameters under predict the results while the predictions obtained with the scaled parameters are in good agreement with the measurements.

Figure 5-22 shows the predicted deformed shape and damaged T-joint image under different loading. It shows that large deformations occur in the vicinity of spot weld N° 3 on vertical faying surface, as shown in Figure 5-22 (a). Under transverse loading, the plastic deformation takes place on the two horizontal faying surfaces, as depicted in Figure 5-22 (b).

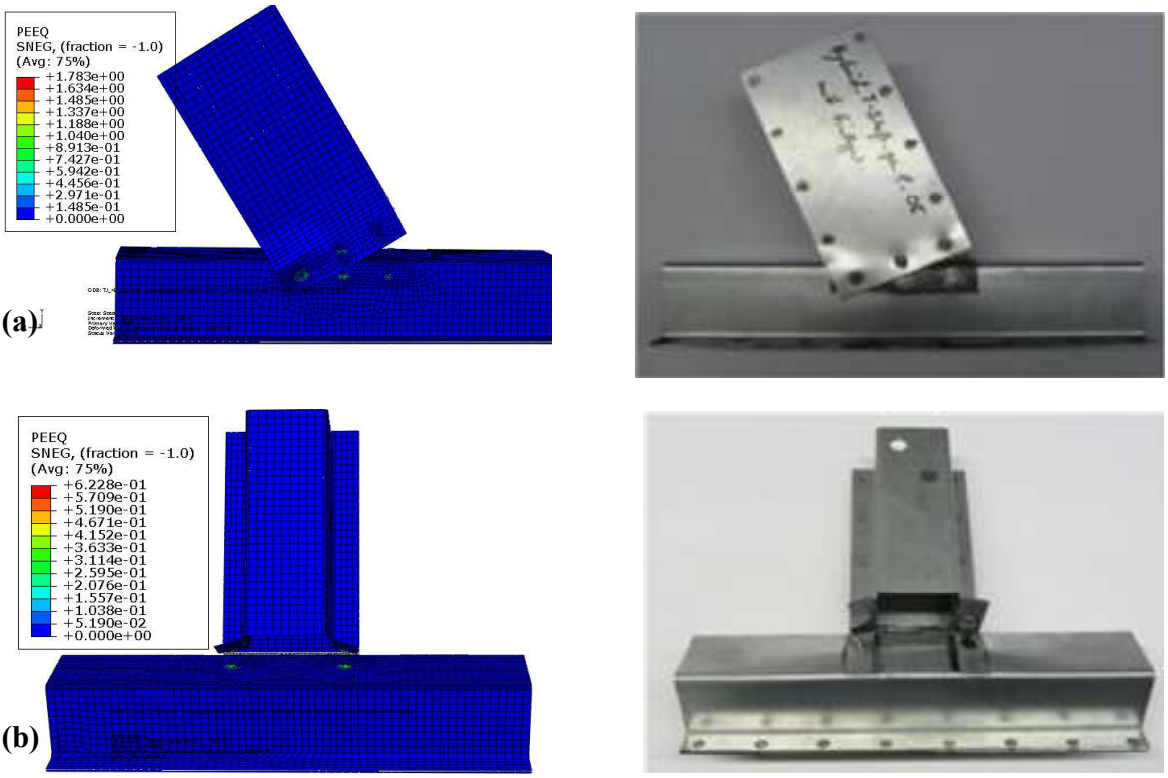

Figure 5-22. *Predicted deformed shape* vs. *test picture of WB T-joint under (a) longitudinal loading and (b) transverse loading*

4. Conclusion

The models developed in Chapter 4 are used to analyze the T-joint test that is representative of the B-pillar. As the hybrid joint performance is assessed by comparison with adhesively bonded joint and spot welded joint, all three types of joints are tested under longitudinal and transverse loading condition.

SW T-joint shows more large deformation than AB T-joint under both loading cases; consequently SW T-joints offer more large energy absorption than AB T-joints. SW T-joint exhibits greater ultimate strength than AB T-joint under transverse loading. However, AB T-joint offers more large ultimate strength as adhesive has good property against shear force under longitudinal loading. WB T-joint exhibits the largest strength and energy absorption in the three joints under both loading condition.

The simplified models can correctly predict the response of T-joints under both longitudinal and transverse loading.

Chapter 6. Conclusion and prospects

Weld bonding is referred to as a complex joining process combining spot welding with adhesive bonding. Compared with adhesive bonding or spot welding, weld bonding has advantages in terms of loading strength and energy absorption, which are favorable to vehicle crash tests. Hence, weld bonding has been employed to improve the stiffness and crashworthiness of car body by joining Advanced High Strength Steel. It is very common that car components or whole car frames are simulated to validate the design prior to the production of prototype. The simulations require reliable models to predict the elastoplastic and damage behaviors. The modelling of weld bonded joint is a new challenge when spot welds are associated with adhesive. On one hand, the nugget of spot weld is heterogeneous. This needs additional material parameters to be calibrated for different zones (BM, HAZ and WM). On another hand, adhesive and spot weld can interact each other. Spot weld heat can diminish the effective surface of adhesive bonding, meanwhile adhesive increase the welding current of spot weld and affect the spot weld dimensions. All these can make the modelling of weld bonded joint a tricky task. Moreover, as regards car crash simulation that uses explicit codes, only the models with adequate stable time step can be acceptable due to the computational cost. Hence, simplified models should also be developed.

The aim of this work is to find adequate constitutive models to predict the failure of weld-bonded joint under complex loading condition. The models intend to be used to simulate large industrial problems.

The adopted methodology consists in combining experiments with numerical models to investigate WB joints in relation to SW and AB joints. As regards the experimental aspects, welding parameters are firstly optimized for spot welding and weld bonding in terms of welding current, squeeze force and squeeze time. Optimal welding current for spot welding is *7.4* while this value is increased to *7.8* for weld bonding. Adhesive layer must have a controlled small thickness in order to obtain optimal mechanical properties. The optimized thickness for SikaPower®-498 is *0.3 mm* in this work. With the help of optimized parameters, SW joints, AB joints and WB joints are successfully produced on KS2 and lap-shear specimens.

The inspection of microstructure on specimens of weld bonded joints was carried out by AFM and OM to investigate the configurations and interactive effect between spot weld and adhesive. Micro-hardness measurement was carried out to verify the microstructure change in spot weld. The complex structure consisting in columnar grains and equiaxial grains are observed in molten zone. The materials are hardened in HAZ due to phase transformation which is evidenced by the hardness tests. As regards WB joint, the hardness distribution of spot weld is not significantly affected by the adhesive. In all the investigated WB joints, an area of burned adhesive of about *2 mm* width is observed in the vicinity of spot weld. The resulting diminution of bonded area is taken into account in FE model of WB joint.

SW, AB and WB joints are tested on KS2 and lap-shear specimens under tension, shear and peeling load.

AB joint exhibits by far the highest strength under shear load among the 3 kinds of joints while it performs the lowest strength under tension load. SW joint exhibits the highest ultimate strength among the three joints under tension load. Generally, SW joint provides excellent energy absorption through the plastic deformation in base metal. WB joint exhibits two stages failure: adhesive failure and spot weld failure except the case of KS2 shear. WB joint can combine high strength with high energy absorption. It offers largest energy absorption under tension and peeling among the three joints. As regards pure shear (KS2 shear), WB particularly exhibits moderate ultimate strength and the lowest energy absorption among the 3 joints. With contrast to pure shear, WB exhibits the highest strength and energy absorption in lap-shear tests. In reality, the damage mode of lap-shear joint is a common case for large component.

For the numerical aspects, both solid and simplified models are developed in this work. The former can predict the response of joint under given configuration for small specimen (KS2 and lap-shear) and build some reference solutions. The latter is used to analyze large components, such as whole car body, to which solid model is inadequate due to the high computational cost.

Firstly, the detailed models of spot weld and adhesive are investigated separately prior to the model of weld bonding. As regards spot weld, sensitivity analysis shows that HAZ and WM property have prominent effect on damage mode and strength of spot weld. Therefore, the heterogeneity of materials in WM and HAZ are taken into account by scaling the flow stress of BM. Inverse identification can be efficiently used to identify scaling factors. CZM with TSLs was associated with Gurson model to predict damage under complex loading (tension, shear and

peeling). Different sets of parameters of Gurson model were calibrated for each zone (BM, HAZ and WM) of spot welds. TSLs are employed to predict the interfacial facture by shear in which Gurson model cannot predict damage adequately. J-integral can be used to assess the damage energy of TSLs. J-integral under tension and shear loading are calculated by simulation of KS2 specimen under tension and shear, respectively. The ultimate strength as well as the displacement at fracture of spot welds (KS2 tension, KS2 shear, peeling and lap-shear) is accurately predicted.

Secondly, as regards adhesive bonding, BM (the adherends) was meshed with 3D solid elements while adhesive was modeled by interfacial element-CZM with TSLs. The parameters of TSLs were calibrated using measurements from DCB and ENF specimen. TSLs have limited capacity to adequately predict the ultimate strength of AB joints with small scale specimens due to the lack of plasticity. The predicted ultimate strength is in good agreement with measurement for each test while the predicted initial stiffness on KS2 shear is higher than that of the tests. The error is supposed to come from measurements as the model can well predict the stiffness of lap-shear tests.

Finally, the models for spot weld and adhesive were combined to predict WB joints under different loading condition. The burned adhesive is taken into account in the model with the help of a *2 mm* gap between the adhesive layer and the spot weld. The model can predict two stages damage (adhesive failure and spot weld failure) of weld bonded joint. The ultimate strength of spot weld stage was accurately predicted by Gurson model and CZM. The strength of adhesive stage is not accurately predicted by TSLs as The TSLs model has limited capacity to estimate the plasticity of SikaPower®-498.

Simplified model was developed for the analysis of large spot welded structure due to its computational efficiency. The connector parameters were calibrated by KS2 specimens under shear, tension and peeling. In simplified model, BM was modeled with shell elements and adhesive with CZM. The spot welds were represented by mesh-independent fastener thereby enabling the use of coarse mesh in BM. Simplified models accurately predicted the ultimate strength as well as displacement for KS2 specimens.

Simplified models for SW, AB and WB are validated by T-joint model which can represent the B-pillar of car frame. The T-joint tests are carried out under longitudinal and transverse loading condition. SW T-joint shows larger deformation than AB T-joint under both loading cases; consequently SW T-joints provide more large energy absorption than AB T-joints. SW T-joint

exhibits larger ultimate strength than AB T-joint under transverse loading. However, AB T-joint offers more large ultimate strength than that of SW T-joint under longitudinal loading because of the high strength of AB under shear load. WB T-joint exhibits the largest strength and energy absorption among the three joints.

The simplified model for T-joint analysis contains shell elements for BM, CZM for adhesive and connector elements for spot weld. Simplified model can efficiently predict the strength and the displacement of T-joints.

Some future works are recommended:

In this work, the primary research reveals that Gurson model cannot predict voids growth for spot weld under shear loading. Alternatively this problem is overcome by introducing CZM. However, the extra CZM model will bring additional parameters to calibrate. Therefore, extended Gurson model with shear damage prediction could be developed to analyse spot weld under pure shear loading.

Adhesive behaviour is temperature-, thickness- and strain rate dependent. The models taking all these effects into account can be implemented to predict the performance of adhesive under more complicated condition.

The CZM model for adhesive has bi-linear shape which can capture the maximum force at damage. However, under shear or lap-shear, the predicted response cannot match with the actual data from experiments. Different CZM models can be found in the literature. It is interesting to implement them to improve the prediction for the adhesive behaviour under shear.

All the models in this work are used for quasi-static loading condition. However, constitutive models with strain rate dependant are required for car crash simulation. As regard simplified models, the model taking strain-rate dependency into consideration is also an interesting issue. Moreover, simplified models with prediction of torsion damage could be developed because some spot welds in T-joint can sustain torsion force under certain loading conditions. It would also be necessary to develop adequate test to calibrate the model parameters for torsion.

Appendix: SikaPower®-498

Automotive

Product Data Sheet
Version 12 / 2008

SikaPower®-498

Crash resistant metal adhesive

Technical Product Data

Chemical base	Epoxy hybrid
Color (CQP[1] 001)	Black
Hazard designation	Xi, N
Non-volatile compounds (CQP 576)	> 99 %
Density before / after curing (CQP 576)	1.3 / 1.3 kg/l approx.
Application temperature	50 - 60°C (nozzle)
Viscosity; 50°C, osc. 5 Hz, P/P 25 mm, 1 mm gap (CQP 584-1, Physica MCR 101)	1300 Pa·s approx.
Curing time / substrate temperature	20 min / 175°C
Lap shear strength[2], at 0.3 mm (CQP 580-1,-6 / EN 1465)	20 MPa approx.
Lap shear strength[2], -30°C / +80°C, at 0.3 mm (CQP 580-1,-6 / EN 1465)	24 / 16 MPa approx.
Lap shear strength[2], 20' 160°C / 40' 200°C, at 0.3 mm (CQP 580-1,-6 / EN 1465)	20 / 19 MPa approx.
Lap shear strength[3], 1.5 mm metal sheet, at 0.3 mm (CQP 580-1,-6 / EN 1465)	30 MPa approx.
Dynamic resistance to cleavage[4] (CQP 580-3,-6 / ISO 11343)	40 N/mm approx.
T-Peel strength[5] (CQP 580-2,-6 / ISO 11339)	10 N/mm approx.
Tensile strength[6] (CQP 580-5,-6 / ISO 527)	30 MPa approx.
Elongation at break[6] (CQP 580-5,-6 / ISO 527)	5% approx.
Glass transition temperature, DMTA (CQP 509 / DIN EN ISO 6721, EN 61006)	100°C approx.
Shelf life, at 23°C (CQP 584-1)	10 months

[1] CQP = Corporate Sika Quality Procedures
[2] DC 04 ZE 75/75 0.8 mm; 2 g/m² Anticorit PL 3802-39 S; adhesive layer: 25 x 10 x 0.3 mm; rate of extension: 10 mm/min.
[3] H320 ZE 50/50 1.5 mm; 2 g/m² Anticorit PL 3802-39 S; adhesive layer: 25 x 10 x 0.3 mm; rate of extension: 10 mm/min.
[4] DC 04 ZE 75/75 0.8 mm; 2 g/m² Anticorit PL 3802-39 S; adhesive layer: 20 x 30 x 0.3 mm; impact speed: 2.0 m/s.
[5] DC 04 ZE 75/75 0.8 mm; 2 g/m² Anticorit PL 3802-39 S; adhesive layer 25 x 100 x 0.3 mm; rate of extension: 100 mm/min.
[6] Rate of extension: 2 mm/min.

Description

SikaPower®-498 is a one-part, warm-applied, heat-curing high-structural, impact modified adhesive based on epoxy.
SikaPower®-498 is designed for sheet metal assembly work in the body shop and is cured with heat, e.g. in the paint oven, to form a high-performance thermoset.
SikaPower®-498 is manufactured in accordance with ISO 9001/14001 quality assurance system and with the Responsible Care program.

Product Benefits

- One-part
- High strength
- Adheres well to oily substrates
- Very high resistance to washing out
- Suitable for joining different metals
- Spot-weldable
- Distortion-free joining
- Provides protection against corrosion
- No damage to substrates
- Contains no solvents, PVC or isocyanate

Areas of Application

SikaPower®-498 is suitable for high structural bonding of different types of metal. As an adhesive product it is designed for use in combination with spot-welding, riveting, clinching and other mechanical fastening techniques, and in some cases as a partial replacement for them. Through a high crack resistance a high integrity, also at extreme deformations (crash), can be reached. The bonding of oily substrates (standard anti-corrosion treatment and deep drawing oils, approx. 2 g/m²) is possible because of the oil uptake during the heat curing that is an essential part of the process.

Cure Mechanism

SikaPower®-498 is cured by heat. The cure-rate depends both on temperature and elapsed time. The most suitable heat sources are convection ovens. The maximum temperature must not exceed 220°C.

Method of Application

SikaPower®-498 is applied in bead form with a recommended diameter of 1 to 3 mm. SikaPower®-498 is filtered with a mesh size of 300 µm before packaging.

Because the viscosity is temperature-dependent (see Fig. 1) all parts of the application system that are in contact with the adhesive must be heated. We recommend phased temperature increase from 40°C at the follower plate to 55°C at the application unit (nozzle). To prolong the life of the packings and facilitate removal of the cut foil disk we strongly recommend a preheating of the new drum for 15 minutes. This will make it easier to remove the foil. During longer breaks (e.g. over night or at the weekend) the equipment must be cooled down to ambient temperature and switched-off and the system (pump and dosage unit) depressurized.

The time between application and curing must be as short as possible, since any uptake of moisture in the interim (climate-dependent) can cause formation of blisters during heat curing. As a guide to process planning, blister formation was not detected after conditioning of uncured parts at 23°C and 80% relative humidity in joined state for two weeks, a drop in dynamic resistance to cleavage was not detected even after four weeks. However, if suitable conditions cannot be guaranteed, pre-curing for 15 minutes at 160°C (substrate temperature) is necessary.

For advice on project-specific application techniques please contact the Corporate System Engineering department (Sika Services AG). For advice on suitable applications (Technical Service) please contact Sika Automotive GmbH.

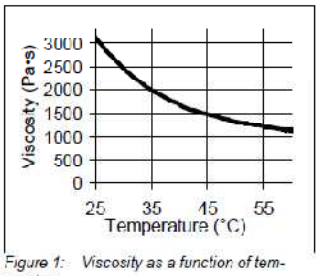

Figure 1: Viscosity as a function of temperature

Further Information

Copies of the following publications are available on request.

- Material Safety Data Sheet
- Pump specification

Packaging Information

Cartridges	310 ml
Hobbock[1]	23 l
Hobbock	50 l
Drum	195 l

[1] 280 mm diameter

Value Base

All technical data stated in this Product Data Sheet are based on laboratory tests. Actual measured data may vary due to circumstances beyond our control.

Local Restrictions

Please note that as a result of specific local regulations the performance of this product may vary from country to country. Please consult the local Product Data Sheet for the exact description of the application fields.

Health and Safety Information

For information and advice on the safe handling, storage and disposal of the chemical products, users shall refer to the most recent Material Safety Data Sheet containing physical, ecological, toxicological and other safety-related data.

Legal Notes

Further information available at:
www.sika.ch
www.sika.com

Sika Automotive GmbH
Reichsbahnstr. 99
D-22525 Hamburg
Germany
Tel. +49 40 540 02 0
Fax +49 40 540 02 241

Reference:

1. Plunkett Research Ltd., Automobiles and Truck Trends. Available from: http://www.plunkettresearch.com/automobiles-trucks-market-research/industry-trends.
2. Rajput R.K., A text book of automobile engineering. New Delhi: Laxmi Publication Ltd., 2007.
3. Kuziak R., Kawalla R., Waengler S., Advanced high strength steels for automotive industry. Archives of civil and mechanical engineering. 2008;8:103-117.
4. García O.L., Micromechanisms of failure under static loading in sheet metals for automotive applications. Ph.D. Dissertation. The Netherlands: Delft University of Technology; 2013 Materials Science and Engineering.
5. Weber G., Thommes H., Gaul H., Hahn O., Rethmeier M., Resistance spot welding and weldbonding of advanced high strength steel. Mat.-wiss. u.Werkstofftech. 2010;41:931-939.
6. Jousset P., Constitutive modeling of structural adhesives experimental and numerical aspects. Ph.D. Thesis. Université de Technologie de Compiègne; Juin 2010.
7. Ghassemi-Armaki H, Maaß R., Bhat S.P., Sriram S., Greer J.R., Kumar K.S., Deformation response of ferrite and martensite in a dual-phase steel. Acta Materialia. 2014;62:197-211.
8. Speich G.R., Properties and Selection: Irons, Steels, and High-Performance Alloys. Volume 1. 1990.
9. Wan X.D., Wang Y.X., Zhang P., Modelling the effect of welding current on resistance spot welding of DP600 steel. Journal of Materials Processing Technology. 2014;241:2723-2729.
10. Ramazani A., Bruehl S., Gerber T., Bleck W., Prahl U., Quantification of bake hardening effect in DP600 and TRIP700 steels. Materials and Design. 2014;57:479-486.
11. Asadi M., De Cooman C.B., Palkowski H., Influence of martensite volume fraction and cooling rate on the properties of thermomechanically processed dual phase steel. Materials Science and Engineering A. 2012;538:42-52.
12. Sun S., Pugh M., Properties of thermomechanically processed dual-phase steels containing fibrous martensite. Materials Science and Engineering A. 2002;335:298-308.
13. Wang W., Wei X.C., The effect of martensite volume and distribution on shear fracture propagation of 600–1000MPa dual phase sheet steels in the process of deep drawing. International Journal of Mechanical Sciences. 2013;67:100-107.
14. Saha D.C., Cho Y., Park Y.D., Metallographic and fracture characteristics of resistance spot welded TWIP steels. Science and Technology of Welding and Joining. 2013;18:711-720.
15. Zhang H., Senkara J., Resistance Welding-Fundamentals and Applications. Boca Raton: CRC Press Taylor & Francis Group; 2006.

16. Movahed P., Kolahgar S., Marashi S.P.H., Pouranvari M., Parvin N., The effect of intercritical heat treatment temperature on the tensile properties and work hardening behavior of ferrite–martensite dual phase steel sheets. Materials Science and Engineering A. 2009;518:1-6.

17. Bleck W., Phiu-On K., Microalloying of Cold-Formable Multi Phase Steel Grades. Materials Science Forum. 2005;500-501:97-112.

18. Brauser S., Pepke L.A., Weber G., Rethmeier M., Deformation behaviour of spot-welded high strength steels for automotive applications. Materials Science and Engineering A. 2010;527:7099-7108.

19. Hou Z.G., Kim I.S., Wang Y.X., Li C.Z., Chen C.Y., Finite element analysis for the mechanical features of resistance spot welding process. Journal of Materials Processing Technology. 2004;184:160-165.

20. Lin S.H., Pan J., Wu S-R., Tyan T., Wung P., Failure loads of spot welds under combined opening and shear static loading condition. International Journal of Solids and Structures. 2002;39:19-39.

21. Jeffus L.F., Welding: Principles and Applications, Fifth Edition. New York: Delmar Learning; 2004.

22. Gupta H.N., Gupta R.C., Mittal A., Manufacturing Processes, 2ED. New Delhi: New Age International Publication Limited, Publishers; 2009.

23. MARYA M., GAYDEN X. Q., Development of requirements for resistance spot welding dual-Phase (DP600) steels part 1-The causes of interfacial fracture. Welding Research. 2005;November:172S-182s.

24. Sommer S., Modeling of the fracture behavior of spot welds using advanced micro-mechanical damage. IOP Conf. Series: Materials Science and Engineering. 2010;10:1-10.

25. Sun X., Stephens E.V., Khaleel M.A., Effects of fusion zone size and failure mode on peak load and energy absorption of advanced high strength steel spot welds under lap shear loading conditions. Engineering Failure Analysis. 2008;15:356-367.

26. Pereira A.M., Ferreira J.M., Loureirob A., Costab J.D.M., Bártoloa P.J., Effect of process parameters on the strength of resistance spot welds in 6082-T6. Materials and Design. 2010; 31:2454-2463.

27. Tong W., Tao H., Jiang X.Q., Zhang N., Marya M. P., Hector L.G., Xiaohong Jr., Gayden Q., Deformation and fracture of miniature tensile bars with resistance-spot-weld microstructures. Metallurgical and Materials Transaction A. 2005;36A:2651-2669.

28. Gould J.E., Khurana S.P., LI T., Predictions of microstructures when welding automotive advanced high-strength steels. Welding Journal. 2006;May:111-116.

29. Raoelison R.N., Étude et modélisation des conditions interfaciales dans le procédé de soudage par résistance par point de tôles d'acier revêtues. Ph.D. Thesis. Université de Bretagne Sud; 2010.

30. Zuniga S., Resistance spot weld failure loads and modes in overload condition. Fatigue and Fracture Mechanics: ASTM SYP 1296, American Society for Testing and Materials. 1997;27:469-489.

31. Lin S.H., Pan J., Wung P., Chiang J., A fatigue crack growth model for spot welds under cyclic loading conditions. International Journal of Fatigue. 2006;28:792-803.

32. Chao Y.J., Ultimate strength and failure mechanism of resistance spot weld subjected to tensile, shear, or combined tensile/shear loads. Journal of Engineering Materials and Technology. 2003;125:125-132.

33. Lin S.H., Pan J., A general failure criterion for spot welds under combinated loading conditions. International Journal of Solids and Structures. 2003;40:5539-5564.

34. Radaj D., Zhang S., Geometrically nonlinear behaviour of spot welded joints in tension and compressive in shear. Engineering Fracture Mechanics. 1994;51:281-294.

35. Falko S., Guillaume M., Matthieu B., Investigation of Spot Weld Behavior Using Detailed Modeling Technique. LS-DYNA Anwenderforum. Bamberg 2008.

36. Sommer S., Modellierung des Verformungs und Versagensverhaltens von Punktschweißverbindungen unter monoton ansteigender Belastung. Ph.D.Thesis. Universität Karlsruhe; August 2009.

37. Dancette S., Fabregue D., Estevez R., Massardier V., Dupuy T., Bouzekri M., A finite element model for the prediction of advanced High Strength Steel spot welds fracture. Engineering Fracture Mechanics. 2012;87:48-61.

38. Donders S., Brughmans M., Hermans L., Liefooghe C., Van der Auweraer H., Desmet W., The robustness of dynamic vehicle performance to spot weld failures. Finite Elements in Analysis and Design. 2006;42:670 - 682.

39. Nielsen K.L., 3D modelling of plug failure in resistance spot welded shear-lab specimens (DP600-steel). International Journal of Fracture. 2008;153:125-139.

40. Darwish S.M.H, Ghanya A., Critical assessment of weld-bonded technologies. Journal of Materials Processing Technology. 2000;105:221-229.

41. Darwish S.M.H., Characteristics of weld-bonded commercial aluminum sheets. International Journal of Adhesion & Adhesives. 2003;23:169-176.

42. Tripathy B., Suryanarayan S., Analytical studies for buckling and vibration of weld-bonded beam shells of rectangular cross-section. International Journal of Mechanical Sciences. 2009;51:77-88.

43. Silva L.F.M., Campilho R.D.S.G., Advances in numerical modelling of adhesive joints. Springer Briefs in Computational Mechanics. 2012; 1-94.

44. Audi A.G., Audi Collision Frame Technology Guide. Audi of America,Inc. 2011.

45. Xia Y., Zhou Q., Wang P.C., Johnson N.L., Gayden X.Q., Fickes J.D., Development of high-efficiency modeling technique for weld-bonded steel joints in vehicle structures-PartI:Static experiments and simulations. International Journal of Adhesion & Adhesives. 2009;29:414-426.

46. Hayat F., Comparing properties of adhesive bonding resistance spot welding and adhesive weld bonding of coated and uncoated DP 600 steel. Journal of Iron and Steel Research International. 2011;18: 70-78.

47. Santos I.O., Zhang W., Goncalves V.W., Bay N., Martins P.A.F., Weld bonding of stainless steel. International Journal of Machine Tools & Manufacture. 2004;44:1431-1439.

48. Mazda. Skyactiv-body. Available from: http://www.mazda.com/technology/skyactiv/platform/skyactiv-body.html

49. Ford Motor Company. Ford Motor Company provide weld bonding procedure. I-Car advantage-Tecnical information for the collision industry. 2005.

50. Chang B., Shi Y., Dong S., Studies on a computational model and the stress field characteristics of weld-bonded joints for a car body steel sheet. Journal of Materials Processing Technology. 2000;100 :171-178.

51. Hahn O., Kurzok J.R., Oeter M., Test specification for KS-2 specimen. Laboratory of Materials and Joint Technology: University of Paderborn; 2000.

52. Seeger F., Feucht M., Frank T., Keding B., Haufe A., An investigation on spot weld modelling for crash simulation with LS_DYNA. Vol Crash-1-Spotweld/Bonding. Bamberg: DYNAmore GmbH; 2005.

53. Pouranvari M., Marashi S.P.H., Failure mode transition in AHSS resistance spot welds. Part I. Controlling factors. Materials Science and Engineering A. 2011;528:8337-8343.

54. ISO4063:212. INTERNATIONAL STANDARD; 1998.

55. Zuniga S., Determining the constitutive properties of the heat influence zone in a resistance spot weld. Modelling and Simulation in Materials Science and Engineering. 1995;3:391-416.

56. Mayer M., Gayden X.Q., Development of requirements for resistance spot welding dual-phase (DP600) steels Part 1- The causes of interfacial fracture. Welding Research. 2005; November:172s-182s

57. Xin S., Khaleel M.A., Dynamic strength evaluations for self-piercing rivets and resistance spot welds joining similar and dissimilar metals, International Journal of Impact Engineering 2007;34:1668-1682

58. Marya M., Wang K., Xiaohong Jr., Tensile shear forces and fracture modes in single and multiple weld specimens in dual-phase steel. Journal of Manufacturing Science and Engineering. 2006;128: 287-298

59. Ghosh P.K., Gupta P.C., Ramavtar, JHA B.K., Weldability of intercritical annealed dual-phase steel with the resistance spot welding process. Welding Reseach Supplement. 1991;January: 7s-14s

60. Lee L.Y., Wehner J.T., Lu W.M, Ultimate strength of resistance spot weld subjected to combined tensile and shear. Journal of Testing and Evaluation. 1998;26:219-313.

61. Dancette S., Fabrègue D., Massardier V., Merlin J., Dupuy T., Bouzekri M., Experimental and modeling investigation of the failure resistance of Advanced High Strength Steels spot welds. Engineering Fracture Mechanics. 2011;78:2259-2272.

62. Jousset P., Simplified parameters identification and modelling. Adhesives and Sealants. 2012 Apr.

63. Fung Y.C., Foundation of solid mechanics. Englewood Cliffs, New Jersey: Prentice-Hall, Inc.; 1965.

64. Wikipedia. Available from: http://en.wikipedia.org/wiki/Hooke's_law.

65. Dunne F., Petrinic N., Introduction to computational plasticity. New York: Oxford university press Inc.; 2005.

66. Wikipedia. Available from: http://en.wikipedia.org/wiki/Von_Mises_yield_criterion.

67. Chakrabarty J., Theory of plasticity, Butterworth-Heinemann, 2006.

68. Zhang Z.L., A complete Gurson Model. Nonlinear Fracture and Damage Mechanics; 2001: 223-248.

69. Gurson A.L., Continuum theory of ductile rupture by void nucleation and growth: Part 1-Yield criteria and flow rules for porous ductile media. Journal of Engineering Materials and Technology. 1977;99:2-15.

70. Tvergaard V., Needleman A., Analysis of the cup-cone fracture in a round tensile bar. Acta Matallurgica. 1984;32:157-169.

71. Tvergaard V., Influence of voids on shear band instabilities under plane strain conditions. International Journal of Fracture. 1981;17:389-407.

72. Sun D.Z., Kienzler R., Voss B., Schmitt W., Application of micro-mechanical models to the prediction of ductile fracture. Fracture Mechanics, 22nd Symposium; 1992; Philadelphia. p. 368-378.

73. Chu C.C., Needleman A., Voids nucleation effects in biaxially stretched sheets. Journal of Engineering Material and Technology. 1980;102:249-256.

74. Pardoen T., Hutchinson J.W., An extended model for void growth and coalescence. Journal of the Mechanics and Physics of Solids. 2000;48:2467mar-2512.

75. Nahshon K., Hutchinson J.W., Modification of the Gurson Model for shear failure. European Journal of Mechanics A/Solids. 2008;27:1-17.

76. Cavalli M.N., Thouless M.D., Yang Q.D., Cohesive-Zone modeling of the deformation and fracture of weld-bonded joint. Welding Journal. 2004;83:133S-139S.

77. Dancette S., Fabrègue D., Massardier V., Merlin J., Dupuy T., Bouzekri M., Investigation of the tensile shear fracture of advanced high strength. Engineering Failure Analysis. 2012;25:112-122.

78. Kregting R., Cohesive zone models towards a robust implementation of irreversible behaviour. Master Thesis. University of Technology of Eindhoven; 23 February, 2005.

79. Ortiz M., Pandolfi A., Finite-Deformation irreversible cohesive element for three-dimensional crack propagation analysis. International Journal for Numerical Method in Engineering. 1999;44:1267-1272

80. Chandra N., Li H., Shet C., Ghonem H., Some issues in the application of cohesive zone models for metal–ceramic interfaces. International Journal of Solids and Structures. 2002;39:2827-2855.

81. Benzeggagh M.L., Kenane M., Measurement of mixed-mode delamination fracture toughness of unidirectional glass/epoxy composites with mixed-mode bending apparatus. Composites Science and Technology. 1996;56:439-449.

82. Nielsen K.L., Tvergaard V., Ductile shear failure or plug failure of spot welds modelled by modified Gurson model. Engineering Fracture Mechanics. 2010;77:1031-1047.

83. Palmonella M., Friswell M.I., Mottershead J.E., Lees A.W., Finite element models of spot welds in structural dynamics: review and updating. Computers and Structures. 2005;83:648-661.

84. Sommer S., Fracture modeling of spot welds and rivets for crash simulation. In: NAFEMS Seminar; 2010; Wiesbaden, Germany. p. 1-12.

85. Heiserer D., Charging M., Sielaft J., High performance, process oriented, weld spot approach. 1st MSC worldwide automotive user conf. Munich, Germany September 1999.

86. Pal D., Cronin D., Static and dynamic characteristics of spot welded sheet metal beams. Journal of Engineering Industry-Transition ASME. 1995;117:316-22.

87. Hibbitt, Karlsson, Sorensen. Abaqus user manual. Ver.6.9. 2007.

88. Dancette S., Fabrègue D., Massardier V., Merlin J., Dupuy T., HAZ microsructure and local mechanical properties of high strength steel resistance spot welds. Engineering Failure Analysis. 2011;78:2259-72.

89. Nielsen K.L., Tvergaard V., Effect of a shear modified Gurson model on damage development in a FSW tensile specimen. International Journal of Solids and Structures 2009;46:587-601

90. Cavalli M.N., Thouless M.D., Yang Q.D., Cohesive-zone modelling of the deformation and fracture of spot-welded joints. Fatigue Fracture Engineering Materials and Structure. 2005;28:861-874.

91. Zhou B., Thouless M.D., Ward S.M., Predicting the failure of ultrasonic spot welds by pull-out from sheet metal. International Journal of Solids and Structures. 2006;43:7482-7500.

92. Rice J.R., A path independent integral and the approximate analysis of strain concentration by notches and cracks. Journal of Applied Mechanics. 1968;35:379-386.

93. Wang D.A., Lin S.H., Pan J., Stress intensity factors for spot welds and associated kinked cracks in cup specimens. International Journal of Fatigue. 2005;27:581-598.

94. Biel A., Stigh U., Effects of constitutive parameters on the accuracy of measured fracture energy using the DCB-specimen. Engineering Fracture Mechanics. 2008;75:2968-2983.

95. Biel A., Mechanical Behaviour of Adhesive Layers. Ph.D. Thesis. Göteborg, Sweden: CHALMERS UNIVERSITY OF TECHNOLOGY. 2008.

96. Sørensen B.F., Jacobsen T.K., Determination of cohesive laws by the J integral approach. Engineering Fracture Mechanics. 2003;70:1841-1858.

97. Al-Samhan A., Darwish S.M.H., Strength prediction of weld-bonded joints. International Journal of Adhesion & Adhesives. 2003;23:23-28.

98. Al-Samhan A., Darwish S.M.H., Finite element modeling of weld-bonded joints. Journal of Materials Processing Technology. 2003 ;142:587-598.

99. Tumiluru M.D., Resistance spot weld of coated high-strength in dual-phase steels. Welding Journal. 2006; June:31-37.

100. Schneider F., Jones N., Infuence of spot-weld failure on crushing of thin-walled structural sections. International Journal of Mechanical Sciences. 2003;45:2061-2081.

101. Yang X., Xia Y., Zhou Q., A simplified FE model for pull-out failure of spot welds. Engineering Fracture Mechanics. 2010;77:1224-1239.

102. Khandoker N., Takla M., Tensile strength and failure simulation of simplified spot weld models. Materials and Design. 2014;54:323-330.

103. Pickett A.K., Pyttel T., Payen F., Lauro F., Petrinic N., Werner H., Christlein J., Failure prediction for advanced crashworthiness of transportation vehicles. International Journal of Impact Engineering. 2004; 30:853-872.

104. Feucht M., Haufe A., Pietsch G., Modeling of adhesive bonding in crash simulation. In: 6th LS-DYNA Anwenderforum; 2007; Frankenthal.
105. Scharff R., Mullen K., Corinchock J.A., Complete automotive estimating. New York: Delmar Publishers; 1990.
106. Weissler P., SAE International. 2010. Available from: http://articles.sae.org/7695/.